# Characterization of the Physical Properties of Atmospheric Aerosols Through Airborne Sampling

Thesis by

Donald R. Collins

In Partial Fulfillment of the Requirements

for the Degree of

Doctor of Philosophy

California Institute of Technology

Pasadena, California

2000

(Submitted April 4, 2000)

# Acknowledgements

As graduate students, it is all too easy to believe that we are entirely responsible for our successes (and, of course, none of our failures). In reality, I owe thanks to so many for making this possible.

I was fortunate enough to have two advisors that complemented one another extremely well. Rick has a unique ability to look beyond traditional approaches to research within our discipline. He always inspired me to push the envelope in my own work, something I hope to instill in my own students someday. His almost child-like excitement about new discoveries in the lab is something that many of us never have to start, and many more lose with time.

In my opinion, John's depth of understanding of this field is unparalleled. This is echoed in the diversity of his research. As a graduate student, this diversity allowed me to choose a project that I was deeply interested in. I believe John's success as an advisor stems directly from the trust he has in his students. This trust inevitably allows the new student to stumble once or twice, not being accustomed to attacking open-ended problems independently. But in the end it leads to independent and self-motivated researchers. These are the attributes that will ultimately lead to success after graduation. I sincerely hope that I will have the patience and faith necessary to take the same approach with my students.

Given my initial ignorance of just about everything in lab, I never could have accomplished what I did without all the support I received from those within and outside my group. In the lab, I would often refrain from asking Jim, Paul, or Greg questions, not because they wouldn't help, but because they wouldn't stop helping, even if it kept them from doing their own work. Without Sherwood's guidance, and his careful design and construction of the ACAD, I would probably be a Caltech for quite a while longer. Lynn was kind enough to take me under her wing during ACE-1, allowing me to get field experience early on. I am grateful to Jian, Tim, and David

both for helping me in lab, and for offering their time and often their equipment to satisfy my curiosity about some scientific subtlety that would likely have no impact on their own work. Thanos saved me at least a month of work by adapting his code to my research, although I think I lost about that same amount of time with all the long discussions we had in the past year. I would also like to thank Matt, Mike, and Jamie for all their help both in the lab and out.

Of all of my co-workers at Caltech, I had the most interaction with Pat. Having to work side-by-side in the field and in the lab for several years could have been a particularly unpleasant situation were it someone else. Instead, we somehow managed to work so closely for so long, and still remained good friends. Since Pat had a little jump on me in time, and a big jump on me in experience, the flow of information between us was typically in one direction. I hope that in the years to come I can repay that information debt and be as much help to him as he was to me.

Jay was one of my biggest influences, and one of my closest friends. Jay and I became friends while we were stumbling through our first year of classes, but it was during my first summer that we really became close, the kind of closeness only 12 hours a day on the 120 °F roof can bring. Whereas most of us get a bit of tunnel vision, focusing only on our immediate research project, Jay fought that tendency, and instead enjoyed learning about just about anything related to our field. He had the talent and personality that would have enabled him to excel in any career he chose. I only wish that he had given himself an opportunity to do so.

Since much of my research involved aircraft sampling, I am indebted to those at CIRPAS that helped make the field projects both enjoyable and productive. Paul, Randy, and Mark worked long and hard to ensure the flights went smoothly and required the least amount of effort from the rest of us. Haf was able to keep the atmosphere light, while at the same time maintaining and utilizing a staggering number of instruments. I am also thankful for the close interactions I had with other groups during these campaigns. Phil Durkee, Phil Russell, Kurt, Beat, Dean, Santiago, Kevin, and Susanne were among those that made these projects so rewarding.

Being an Environmental Engineering Science student with advisors in Chemical

Engineering had some definite perks, one of which was doubling the office staff I could go to. I had just enough interaction with people outside of Caltech to realize just how nice and competent our office staff is. I appreciate all they did during my stay at Caltech, and hope they will remember the few times I did something right rather than the many times they had to fix something I did wrong.

Of course, my friends helped keep me sane over the past five years. The fact that most of my friends were my co-workers and vice-versa is testament to the supportive atmosphere within the department. An all-inclusive list might make these acknowledgments seem like an Oscars acceptance speech, so I'll name only a few. Matt was my tour guide as a prospective student, and with his unsurpassed knowledge of facts and maps, continued in that role over the next few years as well. Somehow I was able to remain friends with Mike Kleeman even after all the pain he put me through while I was his gym partner. Mike Hannigan taught me the ladder of importance - beer, then everything else. My brother Mark remains one of my best friends even after the torment I put him through when we were kids.

Even though both of my parents received doctoral degrees, they never pushed me to do the same, but it was their support that made this possible. Since kindergarten they always made sacrifices to give me the best education possible. In high school, I fought hard to thwart their efforts, but in the end I guess they won. I've managed to get a little of my dad's dedicated but care-free work ethic as well as a little of my mom's dedicated with-a-stress-level-to-prove-it work ethic. Hopefully the mix will work well for me.

Above all others, it was my wife Courtney that gave me the love and support I needed to get through the last five years. Throughout our stay in California, Courtney always seemed to be the one making the sacrifices, whether it was commuting to Long Beach or South L.A. everyday, or leaving her beloved horse behind in Virginia. Between going on several long field projects and often working seven days a week while in California, I was not around as much as either of us would have liked. Still, Courtney found it in her heart to support me during this time, and I'll always be grateful for that.

# Abstract

Atmospheric aerosols are highly variable both in their characteristics and their concentration. Aircraft-based sampling provides a means of characterizing such a complex and variable constituent. To maximize the potential of aircraft sampling, improvements in existing aerosol instrumentation and development of new instruments is necessary.

A new approach to inversion of differential mobility analyzer (DMA) data has been developed that improves the accuracy with which accelerated size distribution measurements can be made. Extensive testing of this inversion has demonstrated that it accurately recovers initial distributions of actual aerosols sampled directly by a commonly used detector, actual aerosols analyzed with a scanning DMA, and test-case aerosols.

To expand upon the measurable size range of the DMA, a new technique has been employed in which the associated flow rates are varied in conjunction with the applied voltage. The performance of the instrument was evaluated theoretically through detailed flow and trajectory modeling, and experimentally through comparison with a constant flow instrument. By varying the flow rates by an order of magnitude, it was shown that measurable size range could be increased by a factor of four.

During the Second Aerosol Characterization Experiment (ACE-2), aerosol size distributions were measured using a DMA and two optical particle counters (OPCs) during 21 missions flown on the CIRPAS *Pelican*. These data were combined with chemical composition measurements to derive a range of associated optical properties, which were compared with simultaneous direct measurements by a sunphotometer and three nephelometers. Agreement between derived and measured quantities varied, but was generally within calculated uncertainties.

A similar payload to that used during ACE-2 was employed for the Southern California Ozone Study (SCOS). Physical and chemical aerosol properties were analyzed

to provide a three-dimensional description of the Los Angeles aerosol. Pronounced aerosol layers aloft were found to exist over the majority of the study area, and over a range of altitudes. In addition to the complex vertical structure of the aerosol observed, horizontal gradients were found to be sufficient to cause more than 50% variability in aerosol concentration over 5 km. The sampled aerosol was estimated to enhance photolysis rates of important gas-phase species by up to 5%.

# Contents

# List of Figures

# List of Tables

# Chapter 1 Introduction

Aerosols are an exceedingly important, but only partially understood, component of the atmosphere. On an urban scale, aerosols have detrimental effects on human health. Recent studies suggest that long-term health risks associated with air pollution are more closely correlated with aerosols than with the gas-phase pollutants that have been the impetus for most of the emissions controls instated in the last several decades. On a regional scale, aerosols are the primary cause of visibility reduction. Combatting the regional influence of aerosols on visibility within America's National Parks has necessitated detailed studies of the mechanisms by which aerosols are transported over thousands of kilometers across state and even country borders. An appreciation of the global importance of aerosols has intensified in recent years. By acting as surfaces for heterogeneous reactions, aerosols alter the gas-phase composition of the global atmosphere. Scattering of solar radiation back into space by atmospheric aerosols can lead to a net reduction in the Earth's energy budget, and subsequently to regional to global scale cooling of the Earth / atmosphere system. Alternatively, absorbing aerosols such as soot and mineral dust can warm the atmosphere by trapping solar radiation that might otherwise reflect off clouds or the Earth's surface and back into space. The relative importance of these two radiative impacts is still uncertain. Even more uncertainty surrounds the indirect impact aerosols have on radiation through alteration of cloud properties.

Understanding, predicting, and potentially mitigating the effects of aerosols is complicated by their non-uniform distribution in the atmosphere, as well as their highly variable properties. Unlike long-lived gas-phase species such as carbon dioxide and methane, aerosols have tropospheric lifetimes on the order of a week. The result is a highly variable aerosol distribution on both a temporal and spatial scale, which can only be fully characterized through long-term and widespread measurements. Also, unlike gas-phase species, which can be uniquely described by their concentration, complete description of an aerosol population requires details of the size, shape, physical state (liquid or solid), composition, mixing state, and concentration of the particles. Of these, particle size and concentration are of particular use in understanding the properties and impacts of an aerosol population. A variety of

techniques are available for estimating the size of a particle through its interaction with its surroundings. These techniques allow analysis of aerosol size distributions at higher time resolution than is generally feasible for measurement of many of the other aerosol descriptors listed above. Commonly, multiple techniques are employed to size particles ranging from a few nanometers to several tens of micrometers.

In recent years, aircraft have increasingly been employed to study aerosols as well as atmospheric gas-phase species. The benefits of such an approach are obvious: spatially-resolved characterization of the aerosol present over a wide area, in regions that are often inaccessible by alternative means. Additionally, for analyses that require knowledge of the columnar properties of an aerosol, such as evaluation of the radiative forcing linked with aerosols, aircraft-based measurements can replace the simple extrapolations from ground-based measurements that would otherwise be necessary. On the other hand, aircraft use in an urban area can capture the three-dimensional distribution of the aerosol present, and allows sampling that is largely unaffected by highly localized sources that can complicate analysis of ground-based measurements. However, aircraft-based sampling also has challenges. Instruments operated on board aircraft must be compact in order to most efficiently use the limited space, weight, and power available to afford the most comprehensive instrumentation payload possible. Additionally, measurement time must be minimized, since at common flight speeds and ascent or descent rates, even a one minute measurement provides an integrated measurement of the aerosol present over about 3 km horizontally, and 150 m vertically.

Size characterization of particles smaller than approximately 0.5 $\mu$m diameter is most accurately accomplished using a differential mobility analyzer (DMA), which separates charged particles with respect to their electrical mobility, from which size is inferred. Significant progress has been made in the development of DMA systems capable of aircraft operation. Still, there is potential to improve upon the performance of the present generation of instruments, aircraft-based or otherwise. Chapter 2 describes a new approach to analysis of DMA data, in which mixing within commonly used detectors is accounted for, thereby enabling accelerated size distribution

measurements. For aircraft studies, this improvement translates into higher spatial resolution. Chapter 3 presents a novel method of DMA operation in which each of the four flow rates of the instrument are varied with time. This vastly increases the measurable size range of the DMA, and is also demonstrated to lead to additional improvements in performance. Implementation of this technique could reduce the number of additional instruments necessary to characterize a complete size distribution.

Two approaches can be taken to study the impact aerosols have on the Earth's radiation budget: Direct measurements of the scattering, absorption, and extinction associated with aerosols, or measurement of the physicochemical properties of the aerosol that can then be linked to optical properties of interest. Ideally, the two approaches will have the same result. In practice, incomplete aerosol descriptions and instrumental error inevitably result in discrepancies. The Second Aerosol Characterization Experiment (ACE-2) provided an opportunity to evaluate the accuracy with which an aerosol physicochemical description derived from measured size distributions can be used to predict a variety of aerosol optical properties. Radiative closure comparisons with a sunphotometer and three nephelometers operated during this campaign are discussed in Chapter 4.

Similar to ACE-2, the Southern California Ozone Study (SCOS) was an intensive study aimed at simultaneous analysis of a wide range of meteorological and air quality parameters. Complex terrain and meteorology associated with areas such as Los Angeles complicate modeling efforts and make the representativeness of point measurements questionable. Use of an aircraft during this study provided a unique three-dimensional description of the local aerosol, which is presented in Chapter 5. These data have been used to evaluate the impact the columnar aerosol loading has on photolysis rates of important gas-phase species, and will ultimately be used to improve upon modeling capabilities within Southern California and elsewhere.

# Chapter 2 Improved Inversion of Scanning DMA Data

*Aerosol Science and Technology*, in press

**Abstract**

Recovery of aerosol size distributions from either stepping or scanning mode differential mobility analyzer (DMA) measurements requires an accurate description of the characteristics of the DMA itself, as well as certain properties of the aerosol. Inversion of scanning DMA data is further complicated by the non-unique relationship between the time a particle exits the DMA and the time it is ultimately detected. Without an accurate description of this relationship, and an appropriate method of accounting for it, inverted distributions will be broadened and skewed relative to the true distribution. A simplified approach to inversion of scanning DMA data is described here in which adjustment of the raw data to account for the delay time distribution associated with the instrument is accomplished prior to final inversion. This provides the flexibility to utilize more accurate descriptions of the delay time distribution and the DMA transfer function than is feasible if the inversion is to be accomplished in one step as described by Russell et al. (1995). The accuracy of this procedure has been demonstrated through analysis of actual as well as test-case data.

## 2.1 Introduction

Since the development of the first of the modern instruments by Knutson and Whitby (1975), the differential mobility analyzer (DMA) has been recognized as an accurate method of measuring submicron aerosol size distributions. Subsequent development of the continuous flow condensation nucleus counter (CNC; Agarwal and Sem, 1978) facilitated computer control of DMA operations (Fissan et al., 1983; Ten Brink et al., 1983) and made the DMA a practical measurement instrument. In the original method of size distribution measurement, the DMA classification voltage is set and, after a delay to ensure steady state conditions, the particle concentration is measured with the CNC or other detector. The classifier voltage is then changed and the process repeated. The computerized measurement system, known as the differential mobility particle sizer (DMPS), has been extensively used to make high resolution particle size distribution measurements. The measurements are, however, slow, often requiring 10 minutes or more depending on the number of voltages employed. Attempts to accelerate the voltage stepping by reducing the settling time leads to distorted measurements.

Wang and Flagan (1989) demonstrated an alternate operating mode for the measurement system in which the classifier voltage was continuously ramped and particle counts were accumulated into a sequence of time bins. By eliminating the settling time between successive measurements, this reduced the time required to measure a complete particle size distribution to as little as 30 s. This instrumental system, which is most commonly known as the scanning mobility particle sizer (SMPS), made the DMA suitable for measurements of rapidly changing aerosols. To interpret the mobility distribution obtained in this scanning-mode operation of the DMA, the time bins into which particle counts are accumulated must be related to particle mobility. Wang and Flagan (1989) interpreted their data by assuming that particles experienced a fixed time delay between exiting the DMA and reaching the detection point within the CNC.

Subsequent studies revealed that this analysis was oversimplified. Russell et al.

(1995) observed tails on the low mobility (large particle) side of distributions measured during increasing voltage scans, and on the high mobility (small particle) side when the scans were performed with decreasing voltages. These tails were attributed to a distribution of delay times caused by mixing within the flow passages of the CNC. To account for this, the flow between the DMA outlet and the detector was modeled as a plug flow region (fixed time delay) in series with a perfectly mixed volume (called a continuously stirred tank reactor or CSTR) that produces an exponentially decaying distribution of delays. The transfer function of the scanning DMA was then modeled as a convolution of the DMA transfer function and the distortion of time bin assignments caused by the delay time distribution. Scanning DMA measurements were inverted using the resulting system transfer function. The analysis required to achieve this result was complex. Moreover, the true distribution could only be found after extensive post-processing of the data.

The inversion of DMA data, whether obtained in scanning or stepping mode, is further complicated by diffusional broadening of the DMA transfer function (Kousaka et al., 1985, 1986; Stolzenburg, 1988). Stolzenburg (1988) derived a semi-analytical expression for the distorted transfer function over a decade ago, but only recently has use of this, or other similar representations, become routine (Zhang and Flagan, 1996; Fissan et al., 1996; Rossell-Llompart et al., 1996). Convolution of a diffusionally broadened transfer function with the delay time distribution, while feasible, would be mathematically complex and computationally intensive. This paper presents a two-step approach to analysis of scanning DMA data in which the raw data are first deconvoluted to remove the effect of mixing within the detector and then inverted, considering only the response function of the DMA itself. The analysis has been applied to a number of different types of DMAs employed under varying ambient and operational conditions.

## 2.2 Inversion Method

Several references are available that describe in detail the governing equations and methods of inversion related to DMA measurements (see, for example, Hagen and Alofs, 1983). Only a brief synopsis will be presented here, with additional detail available in the references given.

The recovery of size distributions, which is referred to as data inversion, requires the solution of the set of Fredholm integral equations,

$$R_i = \int_{-\infty}^{\infty} n(\log D)\Psi(i, D)d\log D \qquad i = 1, 2, 3, ..., I \tag{2.1}$$

where $R_i$ is the $i^{th}$ datum, $I$ is the total number of measurements made, $\Psi(i, D)$ is the response of the $i^{th}$ measurement channel to a particle of diameter $D$, and $n(\log D)$ is the (unknown) number concentration of particles with logarithms of diameter between $\log D$ and $\log D + d\log D$. The particle size distribution is expressed in terms of the logarithm of diameter to facilitate the recovery of distributions that span several decades in particle size.

Regardless of whether the DMA voltage is stepped or scanned, the raw data set comprises a finite number of measurements. Therefore, in practice, the integral in Equation (2.1) is approximated using the trapezoidal rule as

$$R_i \cong \sum_{j=0}^{J} \beta_j n(\log D_j)\Psi(i, D_j) \log\left(\frac{D_{j+\frac{1}{2}}}{D_{j-\frac{1}{2}}}\right) \tag{2.2}$$

where $J$ is the number of size intervals, $D_j$ is the particle diameter corresponding to the $jth$ bin, $D_{j\pm\frac{1}{2}} = \sqrt{D_j D_{j\pm1}}$, and $\beta_j = 1/2$ at the endpoints of the summation and 1 elsewhere.

Equation (2.2) can also be written in matrix form as

$$\vec{\mathbf{R}} = \mathbf{\Gamma}\vec{\mathbf{N}} \tag{2.3}$$

where $\vec{\mathbf{R}}$ is the array of raw data points, $R_i$ $(i = 1, 2, ..., I)$, $\vec{\mathbf{N}}$ represents the array

of solution elements, $n(\log D_j) = N_j (j = 1, 2, ..., J)$, and the elements of the response matrix, $\mathbf{\Gamma}$, are given by $\Gamma_{ij} = \Psi(i, D_j) \log\left(\frac{D_{j+\frac{1}{2}}}{D_{j-\frac{1}{2}}}\right)$, and have the form

$$\Gamma_{ij} = Q_a t_c \log\left(\frac{D_{j+\frac{1}{2}}}{D_{j-\frac{1}{2}}}\right) \bar{\eta}(D_j) \sum_{\phi=0}^{\phi_{\max}} \bar{f}(D_j, \phi) \bar{\Omega}(Z(D_j, \phi), Z_i, \mathrm{Pe}(D_j)) \tag{2.4}$$

where $Q_a$ is the aerosol flow rate, $t_c$ the counting time, and $\bar{\eta}(D_j)$, $\bar{f}(D_j, \phi)$, and $\bar{\Omega}(Z(D_j, \phi), Z_i, \mathrm{Pe}(D_j))$ are the bin averages of the efficiency, charging probability, and DMA system transfer function, respectively. Each of these factors is described below.

The efficiency, $\eta(D_j)$, is the product of the penetration efficiency through the tubing, $\eta_{tube}(D_j)$, the penetration efficiency through entrance and exit regions of the DMA, $\eta_{DMA}(D_j)$, and the counting efficiency of the detector, $\eta_{\mathrm{det}}(D_j)$. Expressions relating tubing and detector efficiencies to particle diameter are available in Friedlander (1977) and Mertes et al. (1995), respectively. DMA penetration efficiency is described by Reineking and Porstendörfer (1986), and Zhang and Flagan (1996). The probability that a particle of diameter $D_j$ has $\phi$ elementary charges of the appropriate sign, $f(D_j, \phi)$, is described by Fuch's theory (1963) as modified by Hoppel and Frick (1986). The choice of appropriate ion properties may depend on the application, with those given by Reischl et al. (1996) applicable for typical ambient conditions. To accelerate the calculations, the Wiedensohler (1988) approximation can also be used. The maximum number of charges considered, $\phi_{\max}$, can be specified for the inversion calculation. It typically ranges between 5 and 10 depending on the particle size range in question.

The transfer function of the DMA column (classifier region), $\bar{\Omega}(Z(D_j, \phi), Z_i, \mathrm{Pe}(D_j))$, represents the fractional transmission of particles of electrical mobility,

$$Z(D, \phi) = \frac{\phi e C_c(D)}{3\pi\mu D}, \tag{2.5}$$

and associated Peclet number,

$$\mathrm{Pe} = \frac{ZV}{\mathfrak{D}}, \tag{2.6}$$

to the detector in channel $i$. The centroid mobility of the particles classified in mobility range channel $i$ is $Z_i$, $C_c(D)$ is the slip correction factor which accounts for non-continuum effects between the particle and the surrounding gas, $e$ is the elementary unit of charge, $V$ is the applied voltage, and $\mathfrak{D}$ is the particle diffusivity. The mathematical form of the DMA transfer function is available in Stolzenburg (1988). His analysis showed that the classical triangular transfer function is distorted into a broadened, continuous function by particle diffusion. Other investigators have also recognized the importance of diffusional broadening of the DMA transfer function, and applied inversions with broadened triangular distributions (Fissan et al., 1996), with the Stolzenburg transfer function (Zhang and Flagan, 1996), or with alternative derivations of the diffusion-broadened transfer function (Rossell-Llompart et al., 1996). Figure 2.1 presents some representative transfer functions for both radial (Zhang and Flagan, 1996) and cylindrical (Stolzenburg, 1988) DMAs.

For bins near the limits of the DMA's range, the transfer function may have finite values for mobilities significantly beyond the minimum or maximum calculated centroid mobility. Particles outside the targeted mobility range are thus transmitted, contributing particle counts to bins near the extremes of the measurement range through the tails of the transfer function. Unless this effect is taken into account, data inversion will overestimate the concentration of particles within these bins. This effect is most pronounced near the high mobility limit of the distribution since these particles undergo substantial diffusion and, therefore, have significantly broadened transfer functions. The resulting error may be minimized by extrapolating both the raw counts data and the response matrix, and then discarding these extrapolated bins after the combined data set is inverted.

In general, multiply charged particles will be sampled by the DMA that would have an electrical mobility less than the minimum mobility of singly charged particles that are classified by the DMA. Unless the number of such multiply charged, large

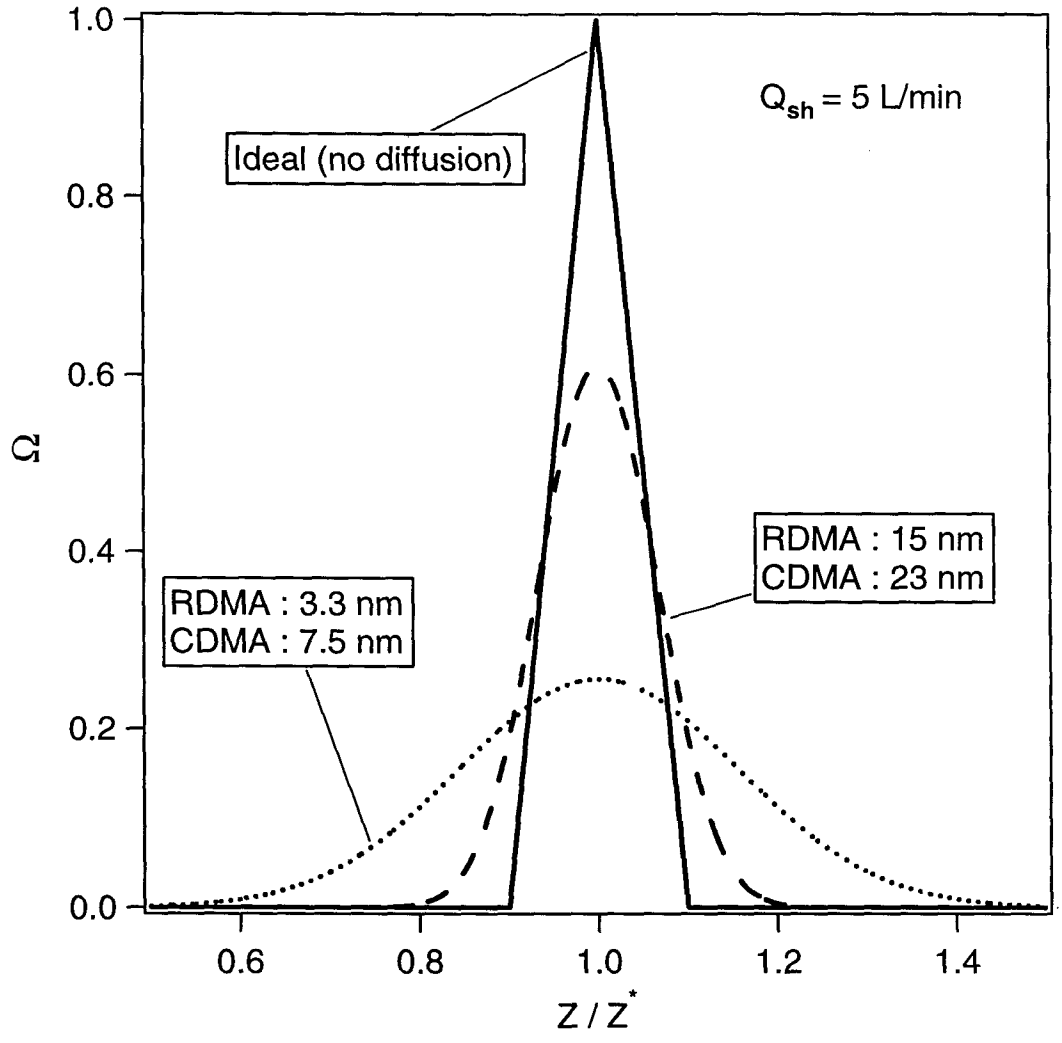


Figure 2.1: DMA transfer functions calculated using the expressions derived by Stolzenburg (1988).

particles is very small, their size distribution must be known from other measurements such as optical particle counters before one can estimate this contribution to the raw DMA data array, $\vec{\mathbf{R}}$. Regardless of the type of measurement used to provide this information, the adjustment can be expressed as

$$\Delta R(D')_{DMA} = -n(\log D)\Gamma(D)\frac{f(D,\phi)}{f(D,1)} \tag{2.7}$$

where $\Delta R(D')_{DMA}$ is the adjustment to the DMA counts corresponding to diameter $D'$, resulting from $n(\log D)$ particles of size $D$, each possessing $\phi$ ($\geq 2$) elementary units of charge. The relationship between $D$ and $D'$ is simply

$$\left(\frac{D'}{C_c(D')}\right)_{DMA} = \frac{1}{\phi}\left(\frac{D}{C_c(D)}\right) \tag{2.8}$$

where $D$ is the particle diameter as it would be measured by the DMA. Since it is unlikely that $D'$ corresponds exactly to any of the actual DMA bins, interpolation is necessary. This bias is often mitigated by using an impactor at the DMA inlet to exclude particles that are too large to be classified in their singly-charged state.

## 2.3 Accounting for CNC Smearing

After exiting the DMA, a classified particle must travel some distance before its ultimate detection. The time associated with this travel is referred to as the plumbing delay time. For a scanning DMA, this time must be known in order to state when the particle was in the DMA, and what voltage ramp the particle experienced. Initial inversions of scanning DMA data were based on the assumption that all classified particles suffer the same plumbing delays (Wang and Flagan, 1989). Given this assumption, the analysis requires only a linear shift of the raw data sufficient to force the distributions corresponding to the up and down scans to overlap. However, particles experience a range of delay times due to mixing and deviations from plug-flow within the tubing and, more importantly, within the condensation nucleus counters that are commonly used to detect the transmitted particles. These non-idealities

smear the particle counts over a range of time bins. Unless this response smearing is taken into account, the recovered size distributions are broadened and distorted. This effect becomes more pronounced as the voltage scan rate is increased or as the features in the measured size distribution sharpen. Only by accounting for the distribution of delay times can the data be accurately analyzed.

Fundamental to the removal of this smearing effect is an accurate description of the relative frequency of particle delay times, or the delay time distribution (DTD) (Russell et al., 1995). Condensation nucleus counters, and in particular the TSI 3010, are the most commonly used detectors for scanning DMA systems and will, therefore, be considered in detail here, although the analysis is readily extended to response delays of electrometers and other detectors. To probe the DTD, Quant et al. (1992) introduced a step-change in particle concentration into a number of different commercially available CNCs. The CNC output at 0.1 s intervals was then recorded to infer the deviation from the constant delay that would result from plug flow within the CNC. The fitted results for both a concentration step-up and step-down for the TSI 3010 are shown in Figure 2.2a. The data indicate that the CNC response approaches that of an exponential decay with a time constant of approximately 0.9 s as is shown in Figure 2.2b. If care is taken to minimize the length of tubing and the number of plumbing connections between the DMA outlet and detector inlet, the additional mixing introduced by external plumbing is typically small relative to that within the detector.

Russell et al. (1995) first addressed this problem by deriving an effective DMA system transfer function that accounted for the smearing effect. This effective transfer function was then used along with the original raw counts data in the final inversion. An advantage of this approach is that the data are inverted in a single step, thereby reducing the errors involved with constraints that must otherwise be placed upon the data at intermediate steps. However, the resulting equations describing the transfer function are very complex. Moreover, diffusional broadening of the DMA transfer function was not incorporated into the derivation. Their analysis was based on the assumption that the response of the CNC decayed exponentially with time.

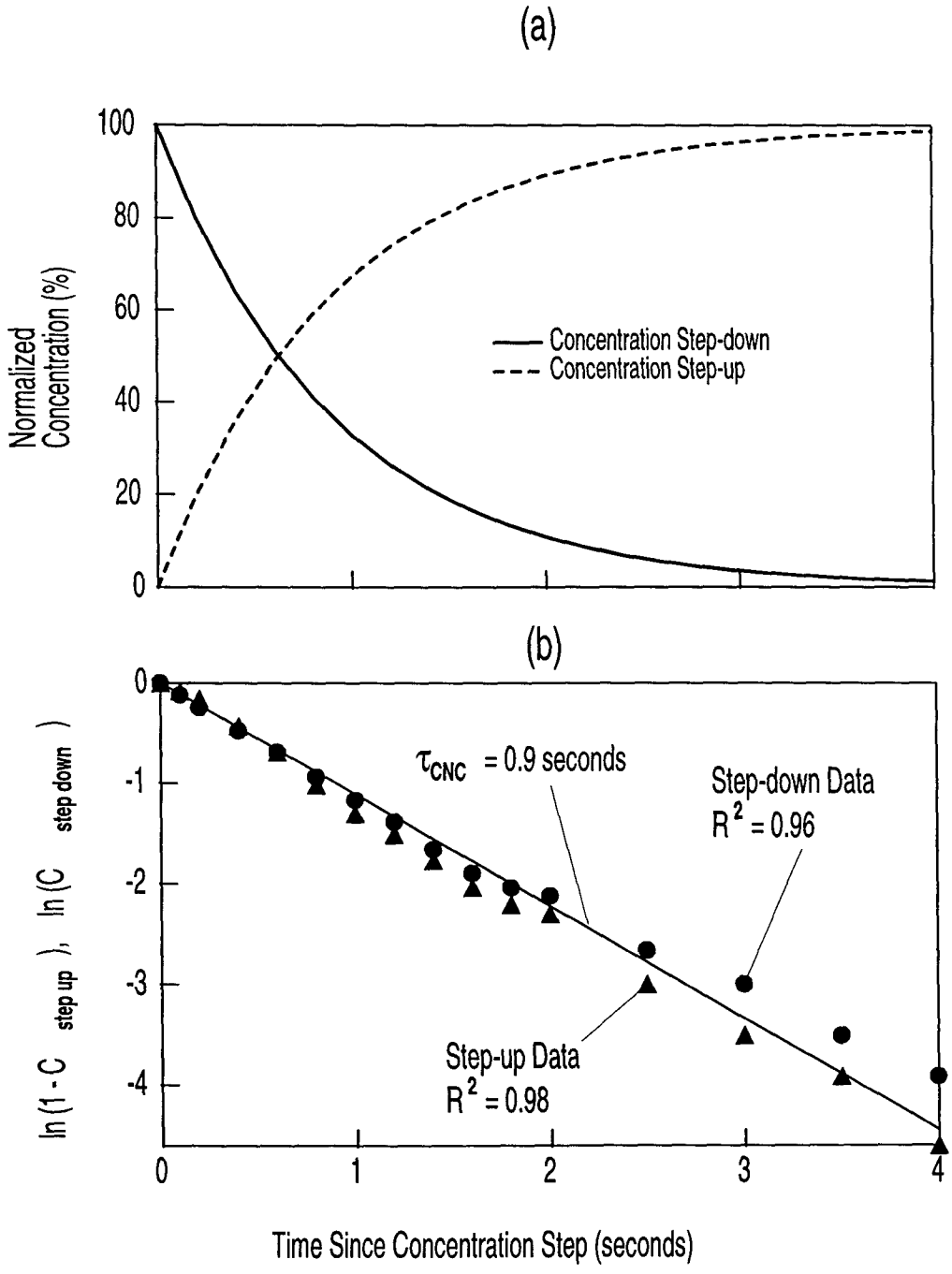


Figure 2.2: (a) Data of Quant et al. (1992) showing the response of the TSI 3010 CPC to concentration step-changes, and (b) the extent to which these data approach an exponential decay function.

We seek to account for both diffusional broadening of the DMA transfer function and the delay time distribution. Rather than attempting to invert the data by taking both effects into account in a single step, we present an approach for deconvoluting the time sequence of raw counts prior to further processing. These adjusted counts data can then be inverted using the conventional scanning DMA transfer function during the inversion process. Not only is the method described below very simple, it is performed separately from evaluation of the response matrices as described above. Hence, changes in the smearing parameters do not require recalculation of the set of matrices. The basic premise behind this analysis is that the number of particles counted during a given time interval is a function of the number of particles exiting the DMA at all previous times as described by

$$C(t) = \frac{1}{t}\int_0^t R(t')\Theta(t-t')dt' \tag{2.9}$$

where $C(t)$ represents the actual detector response (counts), $R(t')$, the number of particles exiting the DMA at time $t'$, is the desired raw counts data, $\Theta(t-t')$ represents the fraction of particles that exited the DMA at time $t'$ that are detected at later time $t$, and $t = 0$ denotes the time at which the entire sequence of measurements was started. As discussed above, DMA data are recorded as the number of counts obtained during discrete averaging times. As with equation (2.1), the counts can be approximated by a summation of the form

$$C_m = \sum_{n=0}^{n=m} R_n \Theta_{(m-n).} \tag{2.10}$$

Equation (2.10) can also be expressed in matrix form as

$$\vec{\mathbf{C}} = \boldsymbol{\Theta}\vec{\mathbf{R}} \tag{2.11}$$

where $\boldsymbol{\Theta}$ is a lower triangular matrix with coefficients,

$$\Theta_{mn} = \begin{cases} \dfrac{\int_{(m-n+1)t_c}^{(m-n)t_c} E(t')dt'}{\int_{t_c\Delta b}^{0} E(t')dt'} & m \geq n,\ \Delta b \geq (m-n),\ n \geq \Delta b \\ \dfrac{\int_{(m-n+1)t_c}^{(m-n)t_c} E(t')dt'}{\int_{nt_c}^{0} E(t')dt'} & m \geq n,\ \Delta b > n \\ 0 & m < n,\ \text{or}\ \ (m-n) > \Delta b \end{cases} \tag{2.12}$$

The number of earlier time bins considered, $\Delta b$, is generally determined from the bin at which the value of $\Theta$ falls below a limiting value. $E(t)$ is the response of the detector at time $t$ to particles that exited the DMA at time $t = 0$. A range of functional forms of $E(t)$, as well as methods of solving equation (2.11), are possible. Use of an exponential decay function, $E(t) = E_0 e^{-\frac{t}{\tau}}$, and direct solution of equation (2.11), represents the simplest approach. Each of the elements of the matrix is then simply an exponential function of time. Direct solution of the triangular matrix can then easily be accomplished by the backsubstitution method,

$$R_1 = \frac{C_1}{\Theta'_0},\quad R_2 = \frac{C_2 - R_1\Theta'_1}{\Theta'_0},\quad R_3 = \frac{C_3 - R_2\Theta'_1 - R_1\Theta'_2}{\Theta'_0} \tag{2.13}$$

$$\text{where}\quad \Theta'_k = \frac{e^{-kt_c/\tau}}{\sum_{p=0}^{\Delta b} e^{-pt_c/\tau}}, \tag{2.14}$$

and $R_i = R(t_i)$ is the number of particles exiting the DMA in the time interval $t_i \leq t \leq t_i + t_c$. To ensure that significant contributions from all previous bins are considered, it may be necessary to include data from previous scans in the raw counts array when the delay between scans is too short. As the ratio $t_c/\tau$ is decreased, the number of earlier bins that need to be considered increases. The number of bins that must be tracked can be reduced by replacing Equation (2.13) with

$$R_n = \frac{C_n - F_n}{1 - \frac{u-1}{u \ln u}} \tag{2.15}$$

where $u = e^{t_c}$, and $F_n = R_{n-1}\frac{(u-1)^2}{u \ln u} + F_{n-1}$, and $F_{n-1}$, which will have been calculated for the previous bin, is given by

$$F_{n-1} = \sum_{k=-\infty}^{n-2} R_k \frac{(u-1)^2}{u \ln u} \frac{1}{u^{n-k}} \tag{2.16}$$

For a continuous stream of data, Equation (2.15) can be used directly after a brief start-up transient.

A more elaborate solution to this problem can also be performed in which a higher order, best fit curve is found for the system transient response data such as that generated by Quant et al. (1992). We have fitted that data set to the functional form

$$E(t) = a \exp(b + ct + dt^2 + ...) \tag{2.17}$$

and used the non negative least squares routine (NNLS) originally written by Lawson and Hansen (1974) to solve the resulting matrix equation. NNLS is an iterative routine that, for a given matrix equation, $\vec{\mathbf{A}}\mathbf{X} = \vec{\mathbf{B}}$, seeks to minimize $\left\|\vec{\mathbf{A}}\mathbf{X} - \vec{\mathbf{B}}\right\|$ with the constraint that all elements, $\{A_i\} \geq 0$. This method is appropriate here since the elements of the solution vector represent particle concentrations that can not physically be negative. The two approaches to deconvoluting the transient response data from the step-change measurements of Quant et al. (1992) are compared in Figure 2.3. Ideally, the adjusted data will recover the form of the step-change that was originally introduced into the CNC. The fitted curve / NNLS solution more closely approaches the expected step change, but even the simpler, direct solution method results in a substantial improvement over the non-adjusted data. The direct solution method may be sufficient for many applications. Moreover, its computational simplicity and efficiency makes it ideal for on-line desmearing and real-time display of scanning DMA data.

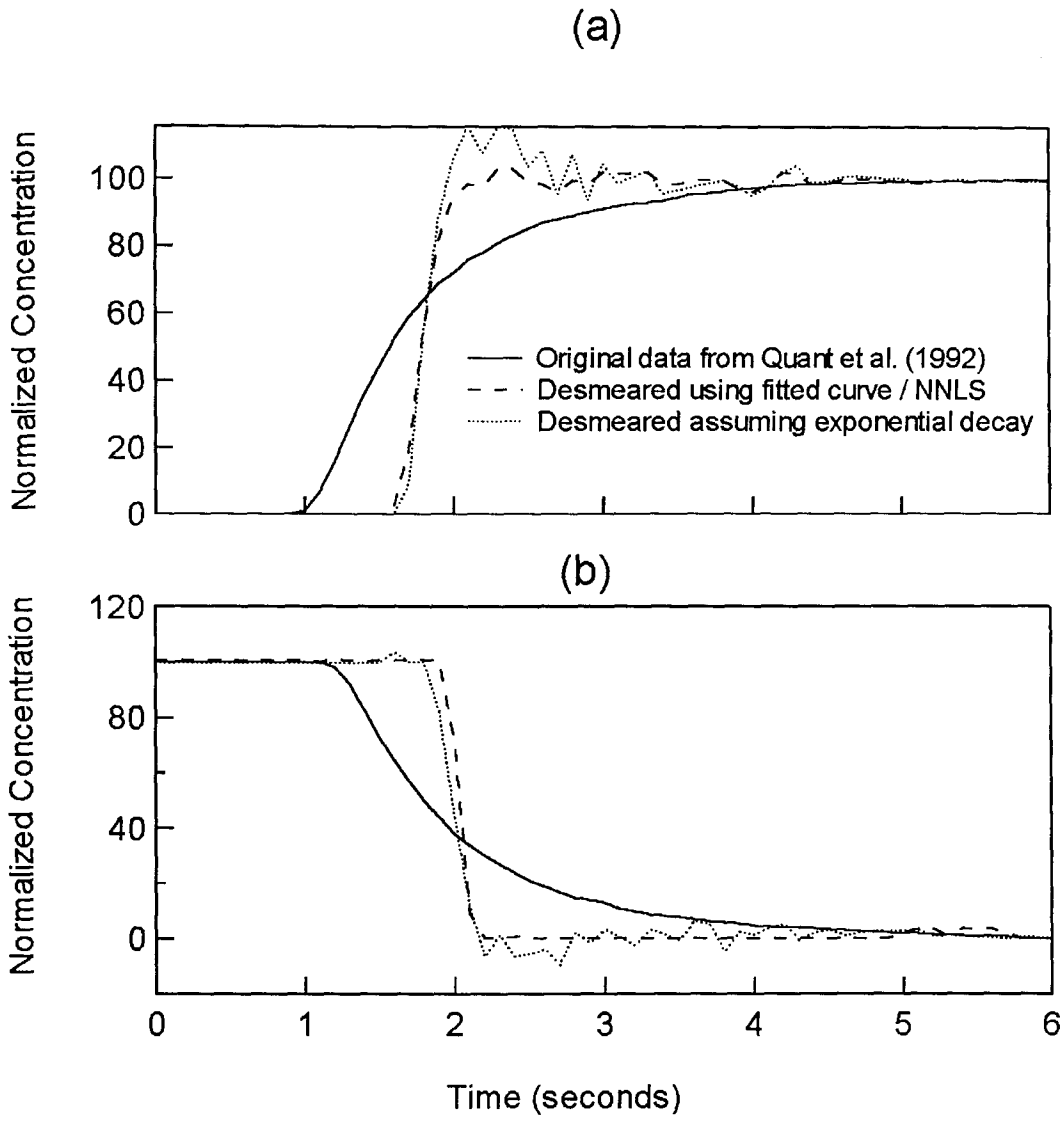


Figure 2.3: Comparison of two techniques used to remove the smearing effect from the concentration step-change data shown in Figure 2.2 for both (a) an increased concentration, and (b) a decreased concentration.

To more clearly demonstrate the impact this mixing has on actual scanning measurements, data were obtained using a DMA that was ramped between 10 and 10000 V over scan times ranging from 30 to 300 s. Consistent with the previous discussion, a TSI 3010 CNC was used as a detector for this analysis. Test aerosols consisted of ammonium sulfate particles of about 100 nm diameter that were generated by atomization and then classified with a DMA operated at a fixed voltage. The sheath-to-aerosol flow rate ratio for both of the DMAs was 10:1. To avoid the additional complications that arise as the residence time of the gas flow within the DMA approaches the voltage scan time, the flow rates were chosen to result in a residence time of less than 2 s. Results obtained using exponentially increasing (up-scan) and decreasing (down-scan) voltage ramps are shown in Figures 2.4a and 2.4b, respectively. Although even the distribution recovered from the 300 s scan is slightly broadened somewhat due to the mixing downstream of the DMA, the deviation from the true distribution is expected to be minimal. Hence, this scan serves as a basis for comparison with the faster ramps. For both increasing and decreasing voltage ramps, the measured distributions are significantly broadened as the ramp time is decreased (Figure 2.4a). For the fastest ramp (30 s), the peak concentration is only $\sim$33% of that measured during the 300 s scan. Figures 2.4c and 2.4d show the results of adjusting these data by assuming that the delay time distribution is represented by an exponential decay with a time constant of 1.5 s. The mixing time constant is larger than the measured CNC smearing time because of the long lengths of tubing that were needed to adapt an existing experimental system to these measurements. Clearly, this simple correction does not produce distributions identical to the 300 s scan, but it does dramatically increase the resolution obtainable with accelerated ramps.

## 2.4 Solving the Matrix Equation

Having calculated the response matrix, $\Gamma$, and the raw counts vector, $\vec{R}$, the solution vector, $\vec{N}$, is found by solving equation (2.3), $\vec{R} = \Gamma\vec{N}$. If there were no errors

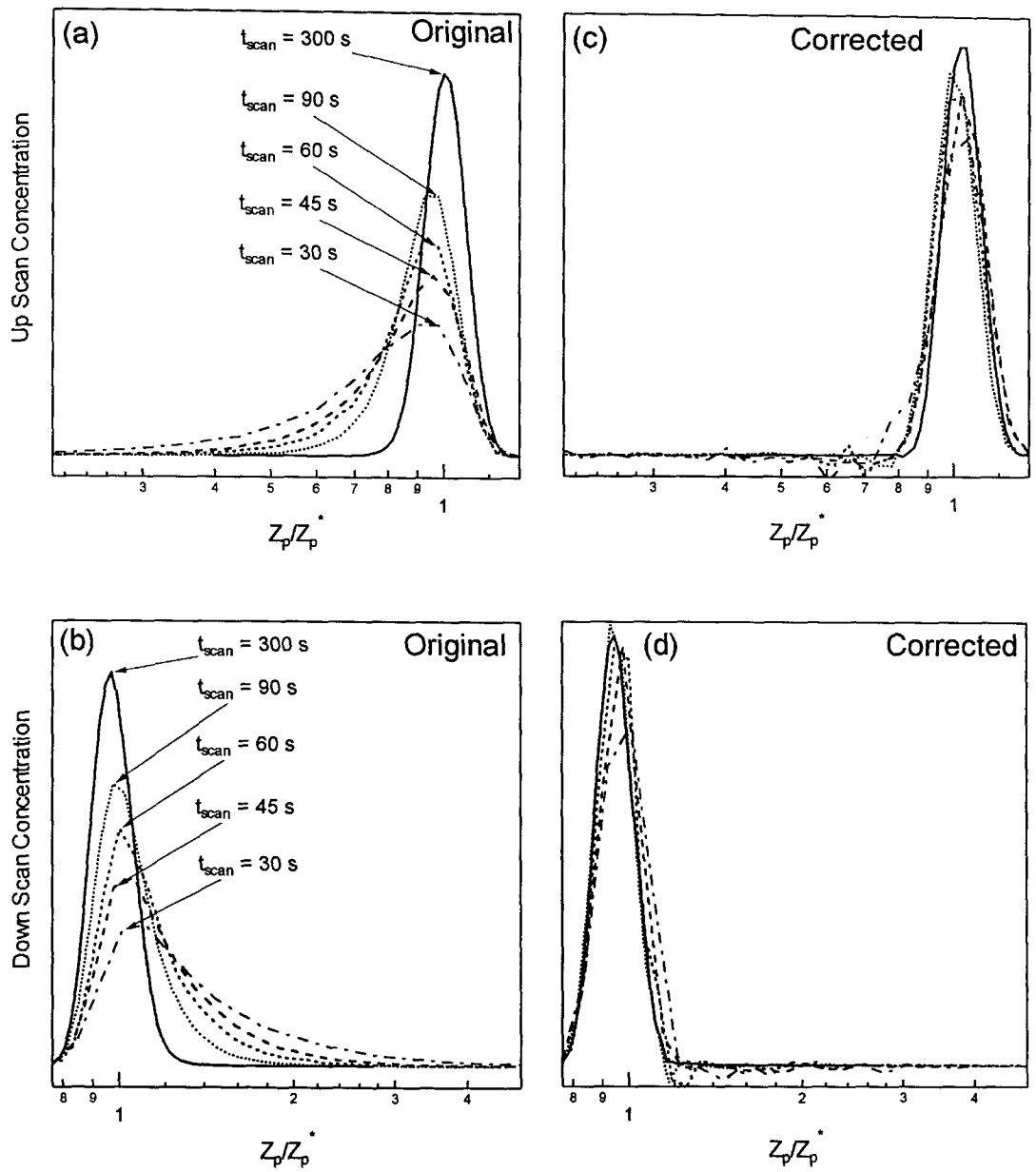


Figure 2.4: Distortion of recovered size distributions for a 3 decade voltage (a) up scan, and (b) down scan. The aerosol analyzed was generated with an atomizer and classified with a DMA at fixed voltage. (c, d) Adjusted size distributions obtained by assuming that the mixing downstream of the DMA resulted in delay times consistent with a simple exponential decay with a time constant of 1.5 s.

or statistical limitations associated with this problem, $\vec{\mathbf{N}}$ could be found directly by multiplying the raw counts vector by the inverse of the response matrix, $\vec{\mathbf{N}} = \mathbf{\Gamma}^{-1}\vec{\mathbf{R}}$. Unfortunately, this often leads to unrealistic oscillations and negative values of $N_i$. A number of approaches to data inversion have been developed to overcome this (Twomey, 1975; Cooper and Spielman, 1976; Alofs and Balacumar, 1982; Crump and Seinfeld, 1982; Hagen and Alofs, 1983; Maher and Laird, 1985; Markowski, 1987; Wolfenbarger and Seinfeld, 1990; Lloyd et al., 1997). These data inversion routines attempt to find a solution vector that approaches a solution of equation (2.3) while requiring that each of the $N_i \geq 0$. Due to its simplicity and widespread use, the Twomey algorithm has been employed here. Similar analyses were conducted using NNLS, but it was found that the recovered distributions contained significant errors when multiply charged particles comprised a significant fraction of the classified particles.

The specifics of the Twomey algorithm have been discussed elsewhere (Twomey, 1975) and will not be described in detail here. A positively-constrained initial guess is necessary as an input for this algorithm. For this, a first order inversion is used in which adjacent bins have been averaged until any negative data points originating from the desmearing step have been eliminated. The loss in resolution resulting from the averaging step is usually insignificant since it is typically necessary only in those intervals within the distribution for which counting statistics would otherwise result in considerable error. Beginning with that initial guess, each of the elements of the solution vector is iteratively multiplied by a factor that improves the agreement between the actual measurement and the response to the trial solution. The number of iterations can be varied but typically ranges between 30 and 50.

To remove the smearing effect from scanning DMA data, one can utilize either the two-step approach described here by first adjusting the raw counts and then inverting the data using a DMA-only transfer function, or invert the raw counts directly by using the effective transfer function derived by Russell et al. (1995). To compare the accuracy of the two approaches, test-case aerosol size distributions were used as inputs

into Twomey-based inversions by each of the two methods[1]. The bimodal test-case aerosol used in Russell et al. (1995) has been replicated for this analysis, and is shown in Figure 2.5. For each of the cases, raw data corresponding to this distribution were calculated using the appropriate instrument response functions, and the assumption that mixing downstream of the DMA was consistent with an exponential decay with a time constant of 1.5 s. The fitted CNC response curve, described in the previous section, is inappropriate here because of the additional contributions of the plumbing connections to the DMA / CNC system response. Data inverted using the Russell et al. transfer function are shown in the top sequence of plots, while those generated using the two-step approach are shown below. Figure 2.5a presents the recovered distributions expected if no adjustment for the mixing is considered, while the results obtained when the mixing is taken into account are shown in Figure 2.5b. As expected for this simple case, each of the two methods accurately recover the initial test-case distribution. To test the robustness of the methods, each inversion was performed 100 times with a $\pm 20\%$ random error in concentration added to the test-case size distribution at each diameter before inversion. The vertical lines shown in Figure 2.5c represent the range of the recovered distributions at each diameter considered. No significant differences are apparent between the two techniques; both result in deviations from the initial test-case distribution that are comparable to the random error introduced.

## 2.5 Summary

Inversion of DMA data, whether obtained by stepping or scanning the applied voltage, poses a unique problem in the study of submicron aerosols. The lack of a unique solution necessitates the use of optimization techniques to find realistic distributions

[1]It should be noted that during this analysis, the following typographical errors were found in Russell et al. (1995):

(1) In Eq. (17), $\beta \equiv 0$ (not 1) when $\gamma \leq 1$

(2) In Eq. (34, v) there should be a + (not -) in front of $\frac{(\zeta_a \pm 1)^{\frac{\Theta_g \pm 1}{\Theta_g}}}{\zeta^{\pm \frac{1}{\Theta_g}}}$

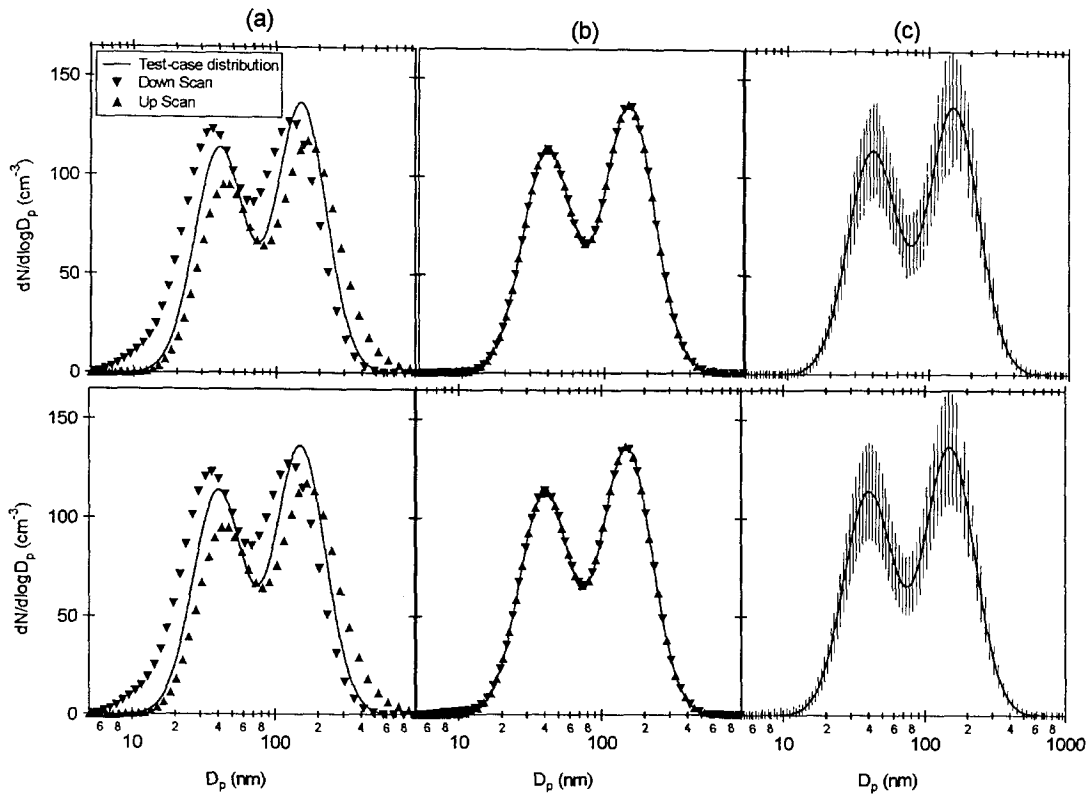


Figure 2.5: Comparison of the size distributions recovered using the bimodal test-case aerosol presented in Russell et al. (1995). The distribution is composed of two log-normals with standard deviations of 1.5, and with concentrations of 50 and 60 $cm^{-3}$ and mean diameters of 40 and 150 nm, respectively. Consistent with the analysis by Russell et al., a ramp time constant of 5.0 s, counting time of 1.0 s, aerosol flow rate of 0.3 L/min, and sheath flow rate of 3.0 L/min were used. The mixing time constant of 1.5 s used for the analysis associated with Figure 2.4 was also used for these analyses. The top sequence of plots represent the results obtained using the transfer function presented in Russell et al., while those below were calculated by first removing the mixing effect from the raw data, and then inverting using a DMA-only transfer function. Shown are (a) the distributions recovered when no adjustment for the mixing effect is considered, (b) distributions recovered for the simple case in which the raw data were calculated using the same time constant as was utilized to invert the data, and (c) the response of the two inversion methods to $\pm 20\%$ random error at each diameter considered. The vertical lines in (c) represent the range of distributions recovered for 100 cases for which random error was added.

consistent with the governing equations and raw data. Inversion of scanning DMA data has many similarities with inversion of stepping data, but with the added complication that the distribution of delay times in detector response must be taken into account. Without this correction, recovered distributions are somewhat broadened. Peaks in the inverted distributions can be as little as 33% of the true peak amplitude. Adjusting the raw DMA data by assuming the delay time distribution can be expressed as a simple exponential decay significantly improves estimation of actual concentrations as compared to raw signals obtained when commercial detectors are subjected to a step change in the aerosol concentration, and of the size distribution of a monodisperse aerosol measured with a scanning DMA. More elaborate corrections using optimization techniques along with fitted curves using detector response data improve the accuracy, although the added complexity of the calculations may not justify the minor gains achieved. Although this paper has focused on the delay time distribution associated with mixing within condensation nucleus detectors, RC time constants in sensitive electrometers will cause similar smearing, and can be addressed by the methods outlined here. Removing the effect of mixing from the raw data counts prior to inversion with a DMA-only transfer function was found to be as accurate for recovery of a test-case size distribution as inclusion of a mixing adjustment directly into the transfer function itself.

# Chapter 3 The Scanning Flow DMA

*Journal of Aerosol Science*, in press

**Abstract**

A new method of DMA operation has been implemented in which the flow rates are continuously changed in conjunction with the applied voltage. By optimizing the flow and voltage ramps, improvements can be made in the DMA's measurable size range, counting statistics, resolution, or a partial combination of each of these. Detailed modeling of this technique suggests that errors on the order of 2 to 5% result from incorrect assumptions concerning the flow profile within the DMA. The experimental system enabled accurate control of flows that were varied by an order of magnitude in as little as 30 s. Excellent agreement was obtained between mobility distributions recovered from a voltage ramp, a flow ramp, and a combined voltage and flow ramp. Slight deviations were apparent in the recovered data as the flow scan time was reduced from 60 to 30 s.

## 3.1 Introduction

The differential mobility analyzer (DMA) consists of a pair of parallel electrodes between which a potential is applied and a gas flows. An aerosol flow, $Q_a$, containing charged particles is introduced adjacent to one of the electrodes. A particle-free sheath flow, $Q_{sh}$, initially separates the aerosol flow from the opposite electrode. A voltage applied to one of the electrodes (typically the center rod of a coaxial cylinder classifier) produces an electric field that causes charged particles to migrate toward the opposite electrode as they are carried through the classifier by the gas flow. Particles that migrate across the gap between the two electrodes in the time they are carried from the upstream aerosol inlet to a downstream exit port are discharged in a small classified sample flow, $Q_s$. Other particles either deposit on the electrode surfaces, or exit the classifier in the excess flow, $Q_e$. The particles contained in the outlet sample flow are classified in terms of electrical mobility, $Z_p$, which is defined as the migration velocity per unit field strength. The relationship between particle transmission efficiency and particle mobility is referred to as the transfer function, $\Omega(Z_p)$. The transmitted particles have mobilities distributed in a narrow region about $Z_p^*$, commonly labeled the centroid mobility because of the symmetry of that distribution for large particles. For a DMA operated with constant flow rates and voltage, the centroid mobility can be expressed as (Knutson and Whitby, 1975; Zhang and Flagan, 1995)

$$Z_p^* = \alpha \frac{2Q_{sh} + Q_a - Q_s}{V} \tag{3.1}$$

where $\alpha$ is a function only of the geometry of the DMA, and $V$ is the applied voltage. This expression applies to both cylindrical and radial DMAs. The classified particle diameter, $D_p$, can then be inferred from the electrical mobility through

$$\frac{D_p}{C_c(D_p)} = \frac{ie}{3\pi\mu Z_p} \tag{3.2}$$

where $i$ is the number of elementary charges on the particle, $e$ is the elementary unit of charge, and $C_c(D_p)$ is the slip correction factor for a particle of diameter $D_p$.

By monitoring the classified sample flow with a continuous-flow particle detector and making a series of measurements at different applied field strengths, the particle size distribution of the aerosol being sampled can be inferred. Utilization of a computer to step the applied voltage and simultaneously record particle counts made the DMA a practical instrument for measuring size distributions (Fissan et al., 1983; Ten Brink, 1983). Continuous scanning of the applied voltage reduced the size distribution measurement time from the many minutes required for stepping-mode measurements to under one minute (Wang and Flagan, 1989). Further enhancement by continuously monitoring the volumetric flow rates of all four streams entering and leaving the DMA, combined with active flow control to maintain the desired flows in spite of pressure variations, has made the DMA a robust system suitable for airborne measurements (Russell et al., 1996).

The computer-controlled DMA fills a very important niche in aerosol particle characterization, allowing high resolution size distribution measurements of particles below the range of optical particle counters and aerodynamic particle sizers, spanning the range from 1 $\mu$m to 3 nm or less. While DMA measurements can be made over a broad range of particle sizes, the size range that can be covered in a given measurement scenario is constrained by practical limits on the range of voltages that can be scanned. The highest classification voltages must be below the threshold for electrostatic breakdown, or spurious counts will be recorded, and the instrument may be damaged. This threshold decreases with decreasing gas density according to Paschen's Law (Meek and Craggs, 1978), complicating aircraft and other low pressure applications. At the opposite extreme, particle diffusion results in deterioration of the instrumental resolution as the voltage is decreased below a threshold value (Stolzenburg, 1988; Flagan, 1999). Figure 3.1 presents the relationship between limiting resolution and applied voltage for the TSI 3071 cylindrical DMA operated with an aerosol to sheath flow ratio, $\beta$, of 10. To some degree, the operator must, therefore, decide whether to focus measurements on the fine particle end of the size spectrum, or to measure larger particles. Additional constraints exist on the flow rates that can be accurately employed. While limits vary between DMAs, sample flow rates below

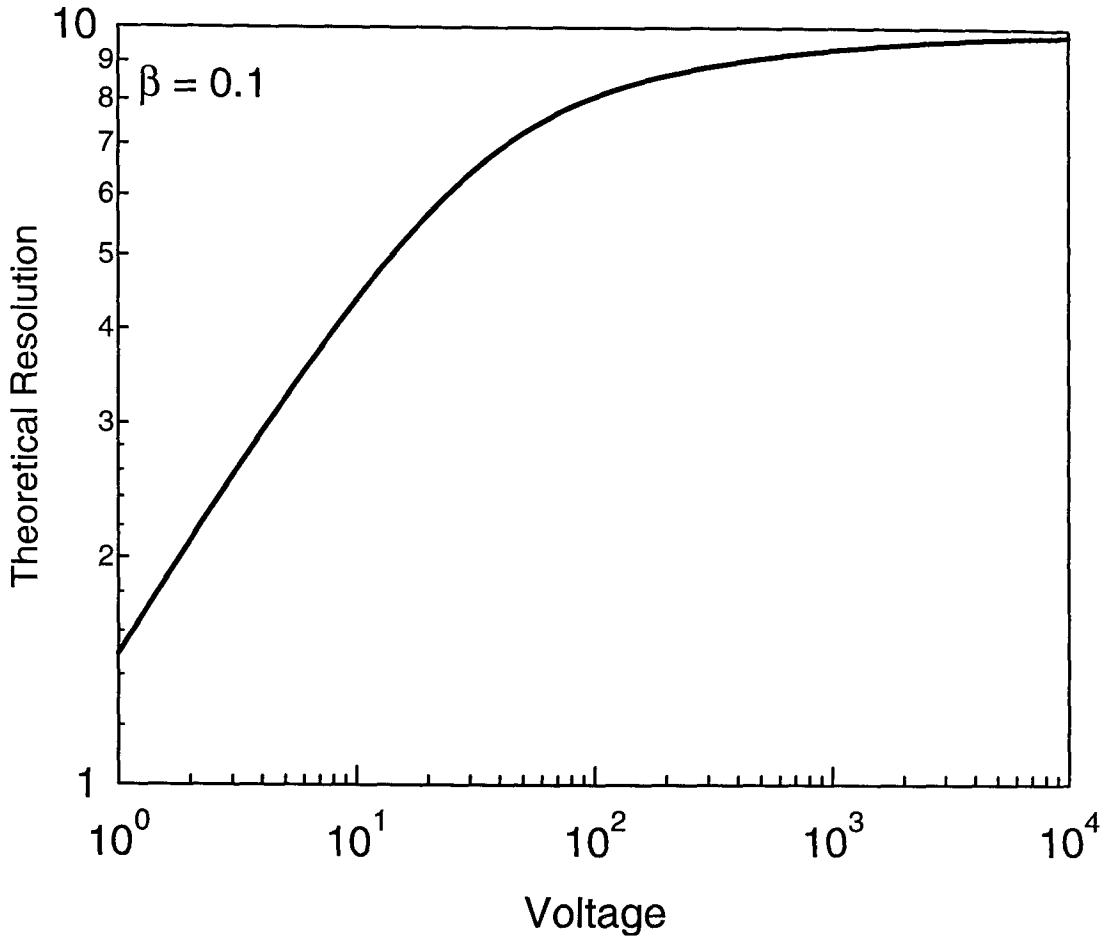


Figure 3.1: Limiting DMA resolution for a typical cylindrical DMA with an aerosol to sheath flow ratio of 0.1.

0.1 - 0.2 L/min will typically result in poor counting statistics; for the commonly used TSI 3071 cylindrical DMA, a sheath flow rate of 20 L/min will be associated with a Reynold's Number of 960, approaching the point at which flow instabilities may occur, although carefully designed and fabricated instruments have been successfully operated well beyond this point (de Juan and de la Mora, 1998). Techniques used to extend the achievable size range in DMA measurements include use of multiple DMAs operated in parallel (Flagan et al., 1991), and switching a single instrument between high and low flow rate modes (Hansson, 1997).

This paper will demonstrate a new approach to extending the range of size dis-

tribution measurements attainable with a single DMA while maintaining the short measurement times that are possible with the scanning mode. By simultaneously scanning both the DMA voltage and flow rates, the particle size range can be dramatically extended while, at the same time, improving both the limiting size resolution and counting statistics associated with the measurement.

## 3.2 Scanning Flow DMA Operation

When particles are classified using a DMA operated at constant voltage and constant flow rates, all transmitted particles follow similar trajectories in the absence of diffusion. Using a particle stream function analysis, the transmission characteristics of the DMA can be shown to be independent of the details of the gas flow velocity profile. If either the voltage or flow rates is allowed to vary, a particle stream function analysis is no longer possible, and examination of particle equations of motion is necessary. In its most general form, particle velocity is described by

$$\frac{dx}{dt} = Z_p E_x + u(x,r,t) \tag{3.3}$$

$$\frac{dr}{dt} = Z_p E_r + v(x,r,t) \tag{3.4}$$

where $E_x$ and $E_r$ are the electric field vectors in the $x$ and $r$ directions, respectively, and $u(x,r,t)$ and $v(x,r,t)$ are the gas flow velocities in the $x$ and $r$ directions, respectively. For the theoretical and experimental analyses presented here, a cylindrical DMA with dimensions similar to those of the TSI 3071 will be considered. Therefore, the following expressions are derived for a cylindrical DMA, although similar expressions exist for a radial DMA. Particles are introduced along the outer electrode in the DMA, radius $R_2$, and migrate toward the inner one, radius $R_1$. For a properly designed cylindrical DMA, the electric field in the annular gap between these electrodes is

$$E_x \simeq 0 \text{ and } E_r = \frac{V}{r \ln \frac{R_1}{R_2}} \tag{3.5}$$

The particle velocity must be known throughout its residence time in the DMA to determine the efficiency with which particles of specified mobility are classified. This task is greatly simplified if all sampled particles follow the same trajectories, i.e., $\frac{dr}{dx} \neq f(t)$. The residence time of a classified particle then varies only with the average gas flow rate during its transit in the DMA. If the flow rate variation does not change the relative flow profile within the DMA, e.g., if the flow is fully developed, the particle velocity would be given by

$$\frac{dx}{dt} = u_o(x,r)\frac{Q(t)}{Q_o} \tag{3.6}$$

$$\frac{dr}{dt} = \frac{Z_p V(t)}{r \ln \frac{R_1}{R_2}} + v_o(x,r)\frac{Q(t)}{Q_o} \tag{3.7}$$

$$\frac{dr}{dx} = \frac{Z_p Q_o}{r u_o(x,r) \ln \frac{R_1}{R_2}} \frac{V(t)}{Q(t)} + \frac{v_o(x,r)}{u_o(x,r)} \tag{3.8}$$

### 3.2.1 Voltage Scan at Constant Flow Rate

In the first report of scanning DMA operation, Wang and Flagan (1989) utilized an exponential voltage ramp while maintaining constant flow rates to accelerate the measurement of complete size distributions. The particle equations of motion for this voltage-scanning DMA are

$$\frac{dx}{dt} = u_o(x,r) \tag{3.9}$$

$$\frac{dr}{dt} = \frac{Z_p V_o}{r \ln \frac{R_1}{R_2}} e^{\pm t/\tau} + v_o(x,r) \tag{3.10}$$

$$\frac{dr}{dx} = \frac{Z_p V_o}{r u_o(x,r) \ln \frac{R_1}{R_2}} e^{\pm t/\tau} + \frac{v_o(x,r)}{u_o(x,r)} \tag{3.11}$$

Breaking the time, $t$, into the time a particle has spent in the DMA, $\Delta t$, and the time at which the particle entered the DMA, $t_{in}$, and integrating the radial velocity over time yields

$$r^2 = R_{in}^2 + \frac{2Z_p V_o(\pm\tau)}{\ln\frac{R_1}{R_2}} e^{\pm t_{in}/\tau}(e^{\pm\Delta t/\tau} - 1) + \int_{t_{in}}^{t_{in}+\Delta t} r v_o(x,r)dt \qquad (3.12)$$

where $R_{in}$ is the radial position of the particle upon entering the DMA. If, as desired, all sampled particles follow the same trajectory,

$$\int_{t_{in}}^{t_{in}+\Delta t} r v_o(x,r)dt = f(x,r) \quad \text{and} \quad \int_{t_{in}}^{t_{in}+t_{res}} r v_o(x,r)dt = k = \text{ constant} \qquad (3.13)$$

where $t_{res}$ is the transit time a classified particle will take to migrate to radial position $R_{out}$. Solution of Equation (3.12) with these limits of integration provides a relationship between the mobility of a classified particle and the time at which it entered the DMA

$$Z_p = \pm\frac{V_o(R_{out}^2 - R_{in}^2 - k)}{2\tau\ln\frac{R_1}{R_2}} \frac{1}{e^{\pm t_{in}/\tau}(e^{\pm t_{res}/\tau} - 1)}. \qquad (3.14)$$

The characteristic mobility of the classified particles leaving the DMA at any instant of time is generally taken as that of the particle that entered the DMA at the centroid of the incoming aerosol flow (expressed here as the radial position $R_{in}$), and exits at the centroid of the outgoing classified sample flow at $R_{out}$. The median mobility, $Z_p^{med}$, of the transmitted particles (and the transfer function) is, however, more relevant to ultimate inversion of the data. Substitution of Equation (3.14) into Equations (3.11) and (3.12) gives

$$\frac{dr}{dx} = \pm\frac{R_{out}^2 - R_{in}^2 - k}{2\tau r u_o(x,r)} \frac{e^{\pm\Delta t/\tau}}{e^{\pm t_{res}/\tau} - 1} + \frac{v_o(x,r)}{u_o(x,r)} \qquad (3.15)$$

$$r^2 = R_{in}^2 + (R_{out}^2 - R_{in}^2 - k)\frac{e^{\pm\Delta t/\tau} - 1}{e^{\pm t_{res}/\tau} - 1} + f(x,r) \qquad (3.16)$$

Finally, solving Equation (3.16) for $e^{\pm\Delta t/\tau}$ and substituting this relationship back into Equation (3.15) yields a time-independent expression for the particle trajectory, i.e.,

$$\frac{dr}{dx} = \pm\frac{1}{u_o(x,r)}\left(\frac{R_{out}^2 - R_{in}^2 - k}{2\tau r(e^{\pm t_{res}/\tau} - 1)} + \frac{r^2 - R_{in}^2 - f(x,r)}{2\tau r}\right) + \frac{v_o(x,r)}{u_o(x,r)} \tag{3.17}$$

The result is a transfer function that maintains a constant shape throughout a scan, and for which the centroid and median mobilities vary with $e^{\pm t/\tau}$. This simplifies the analysis of voltage-scanning DMA data, but imposes constraints on the manner in which voltage is varied. Additionally, only those particles that experience the voltage ramp throughout their entire transit are considered, i.e., particles that enter prior to the start of the ramp or exit the column after the ramp is complete are not accurately described by this first-order model. Relative to stepping mode operation, this restriction reduces the mobility range analyzed to

$$\frac{(Z_{p\max}/Z_{p\min})_{scan}}{(Z_{p\max}/Z_{p\min})_{step}} = \frac{(\bar{V}_{\max})_{scan}}{V_{\max}}\frac{V_{\min}}{(\bar{V}_{\min})_{scan}} = \frac{\int_0^{t_{res}} e^{-t/\tau}dt}{t_{res}}\frac{t_{res}}{\int_0^{t_{res}} e^{t/\tau}dt} \tag{3.18}$$

$$= -\frac{\left(\frac{V_{\max}}{V_{\min}}\right)^{-t_{res}/t_{scan}} - 1}{\left(\frac{V_{\max}}{V_{\min}}\right)^{t_{res}/t_{scan}} - 1} = \left(\frac{V_{\min}}{V_{\max}}\right)^{t_{res}/t_{scan}} \tag{3.19}$$

For a TSI 3071 DMA operated with a sheath flow rate of 3 L/min, a 60 s scan over 3 decades of voltage reduces the analyzed mobility range by a factor of approximately 2.4.

Although the shape of the DMA transfer function does not change during an exponential voltage scan, it may differ from that in the constant voltage case due to differences in the time that the particle resides in different regions of the flow. At constant voltage, the particle residence time equals the mean fluid residence time. When the voltage increases with time, a particle will pass through the low velocity, low field region near the outer electrode more slowly than it will through the high velocity core of the flow or the high field, low velocity region adjacent to the inner electrode. The reverse is true for a decreasing voltage scan. This leads to an asymmetry in the

transfer function and a shift in the median mobility of the two scans. The effect is generally small at commonly used scan rates, but the scanning DMA system should be calibrated to eliminate the resulting biases. As a first approximation, the median mobility can be estimated using Equation (3.14) with the assumption that the particle residence time is the same as the mean gas residence time. By measuring the system response to a monodisperse aerosol and adjusting the so-called plumbing time until the recovered distribution is consistent with the known size of the sampled aerosol particles, the system can be calibrated for future measurements. For plug flow, this plumbing time is simply the transit time between the DMA outlet and the detector, but when the gas velocity varies with position, it is the sum of the transit time and an adjustment that accounts for the difference between the residence time of a sampled particle, and that of the mean gas flow. From Equation (3.14), this adjustment time, $t'$, is related to the (unknown) particle residence time, $t_{res_p}$, through

$$\begin{aligned} (\exp(\pm t_{res_p}/\tau) - 1)\exp(\pm t_{in}/\tau) &= (\exp(\pm t_{res_g}/\tau) - 1)\exp(\pm(t_{in} + t')/\tau) \quad (3.20) \\ \text{or} \quad t' &= \pm\tau \ln \frac{\exp(\pm t_{res_p}/\tau) - 1}{\exp(\pm t_{res_g}/\tau) - 1} \end{aligned}$$

Even if the particle residence time during an up scan is the same as that during a down scan, this adjustment will not be, so two plumbing times must be determined.

### 3.2.2 Flow and Voltage Scan

Even with the limitations and uncertainties associated with the exponential voltage-scanning technique, the time-independent transfer function is preferable to the time-varying transfer function that would result from other voltage ramps. Therefore, for a flow-scanning DMA, it would be desirable to find a suitable set of ramps that would satisfy the constant trajectory requirement discussed above. From Equation (3.8), it is clear that, if $\frac{V(t)}{Q(t)} = \text{constant}$, $\frac{dr}{dx} \neq f(t)$ provided the velocity profile in the DMA does not change, and calculation of the DMA transfer function will be facilitated. However, contrary to this requirement, an increasing voltage must be

coupled with decreasing flow rates and vice-versa to expand the measurable size range. Unfortunately, no ramp combinations exist that satisfy both of these requirements. Moreover, unless the variation is slow and the flow is fully developed throughout the scan, the assumption that the shape of the flow profile remains constant is unrealistic when flow rates are varied. Thus, although flow-scanning increases the dynamic range of the DMA, it may complicate data analysis since the transfer function will vary with time, as will the flow profile within the DMA.

The flow in a DMA is usually approximated either as a plug flow in which the gas velocity is uniform across the flow channel, or as a fully developed laminar flow in which the velocity varies transverse to the flow, but not in the streamwise direction (at least for the cylindrical DMA). For operation at constant flow rate and field strength, these flows represent extremes that bound the actual performance. Since scanning operation may be more sensitive to the details of the velocity profile, we have examined the impact of deviations from these idealized flow fields on two measures of instrument response: (i) the integral of the transfer function over the logarithm of the mobility,

$$I_{\log Z} = \int_{-\infty}^{\infty} \Omega(\log \frac{Z_p}{Z_{p_o}}) d \log \frac{Z_p}{Z_{p_o}};$$

and (ii) the median mobility of the transfer function, $Z_p^{med}$, defined such that

$$\int_{-\infty}^{\log Z_p^{med}/Z_{p_o}} \Omega(\log \frac{Z_p}{Z_{p_o}}) d \log \frac{Z_p}{Z_{p_o}} = \frac{1}{2} \int_{-\infty}^{\infty} \Omega(\log \frac{Z_p}{Z_{p_o}}) d \log \frac{Z_p}{Z_{p_o}} \tag{3.21}$$

For a size distribution that is broad compared to the transfer function, $I_{\log Z}$ is proportional to the particle transmission rate.

The flow field within the DMA was predicted by numerically solving the Navier-Stokes equations for laminar flow (Bird et al., 1960) using a finite volume method (Patankar, 1980). A staggered grid, in which each velocity grid node lies between two volumes, is used for the calculations (Patankar, 1980). This procedure ensures that

the numerical solution yields a realistic pressure field. The SIMPLE iterative solution method is used to solve the finite volume equations (Patankar, 1980). The computer code used for the numerical simulations is a modified version of the TEACH-2E code (Gosman, 1974). For each flow rate considered, the numerical solution was obtained using 150 cells for the x- and 50 cells for the r- directions, respectively. For the theoretical and experimental analyses presented in this paper, the sheath flow rate was varied between 2 and 20 L/min, while the sheath to aerosol flow rate ratio was maintained at 10. The calculated velocity vectors and fluid streamlines corresponding to the extremes within this range are shown in Figure 3.2. While differences do exist between the 2 and 20 L/min flow fields, they are seen to be significant only immediately downstream of the aerosol inlet and immediately upstream of the sample outlet. The fastest flow ramp considered, 30s, is long enough compared to the characteristic time for viscous diffusion ($\tau_v \sim (R_{in}^2 - R_{out}^2)/\nu \sim 5$ s) that the flow may be assumed to be quasi-steady.

The transfer function was examined for scans with a sheath flow rate variation between 2 L/min and 20 L/min, and a voltage range of 10 V to 10,000 V. Since the perturbations caused by scanning DMA operations depend on the rate of change of the flow and voltage, and the variations of these parameters span the majority of the accessible ranges for the TSI long column cylindrical DMA (Model 3071 or 3081), the analysis that follows provides an estimate of the maximum perturbations that are likely for scans as short as 30 s. For plug flow, the axial particle velocity is constant and equals the mean gas velocity. For this simplified case, the voltage-scanning transfer function that was presented by Wang and Flagan can be used for combined flow and voltage-scanning operation with little modification,

$$\Omega(Z_p, t) = \max\{0, \min[(K(t) + 1 - 1/\beta), (-K(t) + 1 + 1/\beta)]\} \qquad (\text{for } Q_a = Q_s) \tag{3.22}$$

$$\text{where } K(t) = -Z_p \frac{2\pi L}{\beta \ln \frac{R_1}{R_2}} \frac{\int_{t-t_{res}}^{t} V(t')dt'}{\int_{t-t_{res}}^{t} Q_{sh}(t')dt'} \tag{3.23}$$

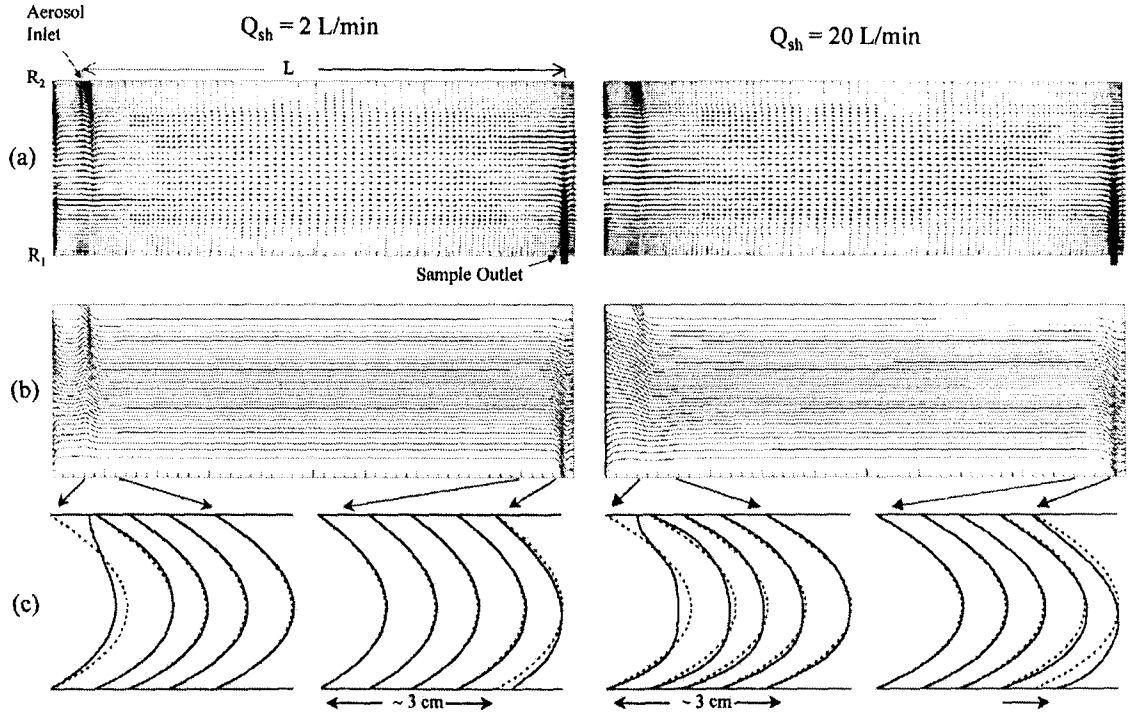


Figure 3.2: (a) Modeled velocity vectors, (b) modeled fluid streamlines, and (c) deviations between modeled (solid line) and fully developed (dashed line) flow profiles near the inlet and outlet of a cylindrical DMA with overall dimensions identical to the TSI 3071. The two cases given (2 and 20 L/min) represent the extremes employed in our analysis. For both cases, a sheath to aerosol flow rate ratio of 10 is used.

To clearly show the increasing transmission rate of particles with increasing flow rate, an effective transfer function, $\Omega'(Z_p, t)$, is defined as the product of the transmission efficiency and sample flow rate normalized to its initial value,

$$\Omega'(Z_p, t) = \Omega(Z_p, t)\frac{Q_s(t)}{Q_s(t=0)} \tag{3.24}$$

For plug flow, the integral of this expression over the logarithm of mobility varies only with sample flow rate, while the median mobility is directly related to the mean voltage and flow rates experienced over the gas residence time, i.e.,

$$\int_{-\infty}^{\infty} \Omega(\log\frac{Z_p}{Z_{p_o}})d\log\frac{Z_p}{Z_{p_o}} = C_1\frac{Q_s(t)}{Q_s(t=0)} \tag{3.25}$$

$$Z_p^{med} = C_2\frac{\int_{t-t_{res}}^{t} V(t')dt'}{\int_{t-t_{res}}^{t} Q_{sh}(t')dt'} \tag{3.26}$$

where $C_1$ and $C_2$ are constants related to $\beta$ and the DMA dimensions. For both modeled and fully developed flow, $I_{\log Z}$ and $Z_p^{med}$ were calculated by numerically integrating particle trajectories over time. The transfer functions calculated using the modeled flow fields for a 60 s ramp are shown in Figure 3.3. Following the convention given by Wang and Flagan (1989), voltage is increased (while flow rate is decreased) during an up scan (decreasing mobility) and decreased (while flow rate is increased) during a down scan (increasing mobility). The direct relationship between sample flow rate and transfer function height is apparent. Figure 3.4 shows the integral and median mobility of the transfer function as a function of time for this 60 s scan, along with the corresponding quantities for the plug and fully developed flow cases. Consistent with the use of the time offset described in the analysis of voltage-scanning data, the median mobility curves were shifted with respect to time (0.45 s) to achieve agreement. While slight deviations are seen to exist between the three cases considered, they are relatively small, with maximum errors in both $I_{\log Z}$ and $Z_p^{med}$ of approximately 2% and 6% for the developed and plug flow cases, respectively. The relationships between these maximum discrepancies and scan time

are presented in Figure 3.5. Fully developed flow better approximates the actual performance of the DMA than does plug flow. The deviations in median mobility resulting from the fully developed flow model increase slightly with decreasing scan times. Although these errors may be excessive for certain applications, they are of comparable magnitude to other errors common in size distribution measurements such as those related to charging probability uncertainty and flow control.

One further complication arising from this method is the pressure variation within the DMA that is caused by flow rate dependent finite pressure drops in the entrance and exit regions of the DMA and across the laminar flow elements that are used to monitor the flow rates. This leads to a slight imbalance in the flow rates since the density within the column will change in the course of the measurements. The pressure drop within the classification region of the DMA is small, so impacts of the pressure drops can be examined by considering a mole balance on the DMA column. The accumulation of material within the DMA can be expressed as the difference between the incoming and outgoing flows, i.e.,

$$\left(\frac{dc}{dt}\right)_{DMA} = \frac{c(Q_a + Q_{sh} - Q_s - Q_e)}{\mathcal{V}_{DMA}} \tag{3.27}$$

where $c$ is the molar concentration of the gas within the DMA and $\mathcal{V}_{DMA}$ is the volume of the DMA. As will be described below, the sheath and excess air flows are connected through a low volume recycle loop, so $Q_{sh} = Q_e$. Also, if the pressure within the recycle loop is directly related to the pressure within the DMA, it is the combined DMA / recycle loop volume that is relevant in Eq. (3.27). Applying the ideal gas law and assuming constant temperature yields a predicted flow imbalance between the sample and aerosol flows of

$$Q_a - Q_s = \frac{\mathcal{V}_{DMA}}{p}\frac{dp}{dt} \tag{3.28}$$

Measurements of the DMA pressure as a function of aerosol flow rate are shown in Figure 3.6. The combined volume of the DMA and recycle loop, $\mathcal{V}_{DMA}$, was

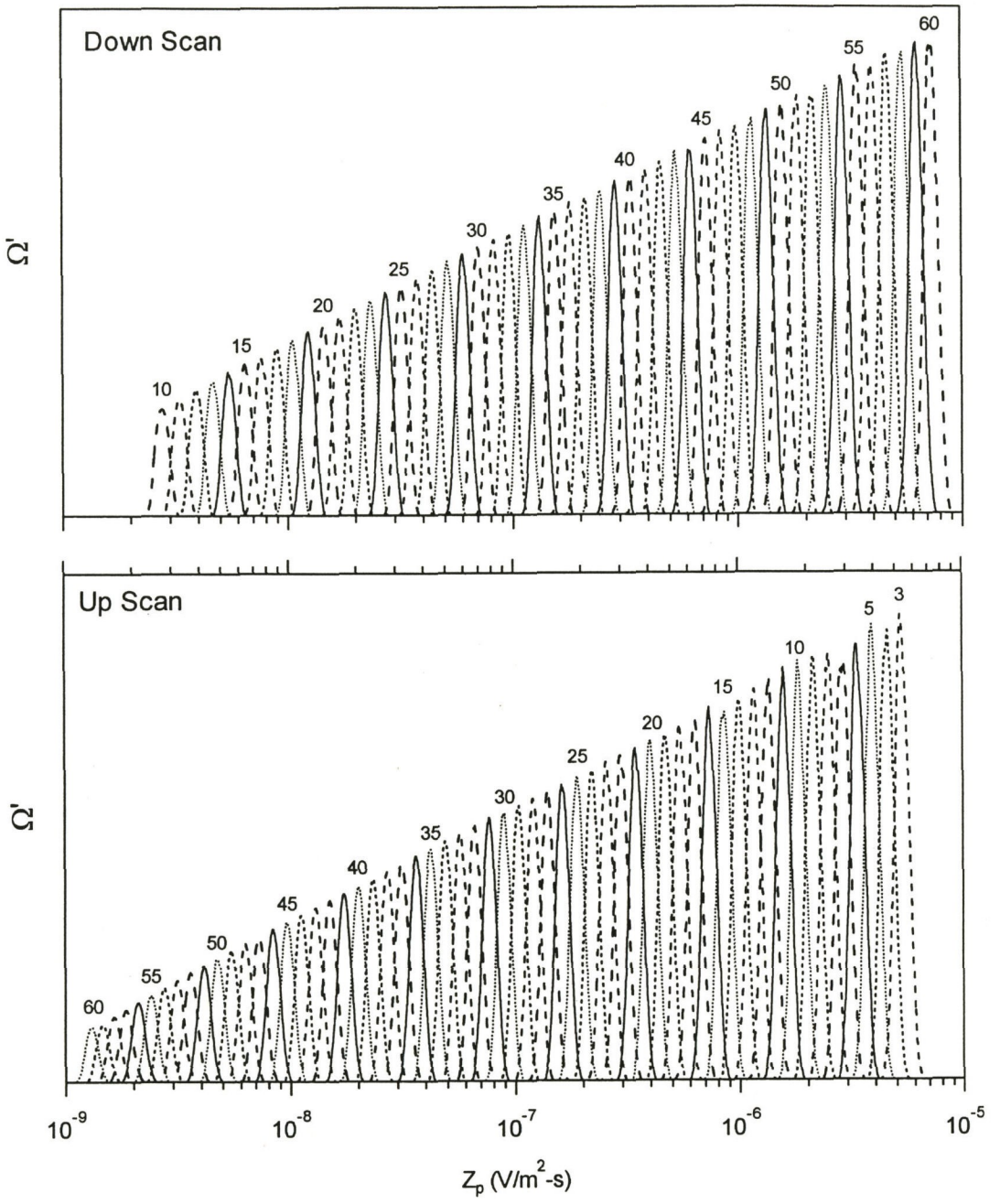


Figure 3.3: DMA transfer functions calculated using modeled flow fields for a 60 s scan during which the sheath flow was varied linearly from 2 to 20 L/min as the voltage was ramped from 10 to 10000V. To clearly show the variation in the transfer functions as a function of flow rate, only those for which particles experienced ramping flows and voltage throughout their transit are shown.

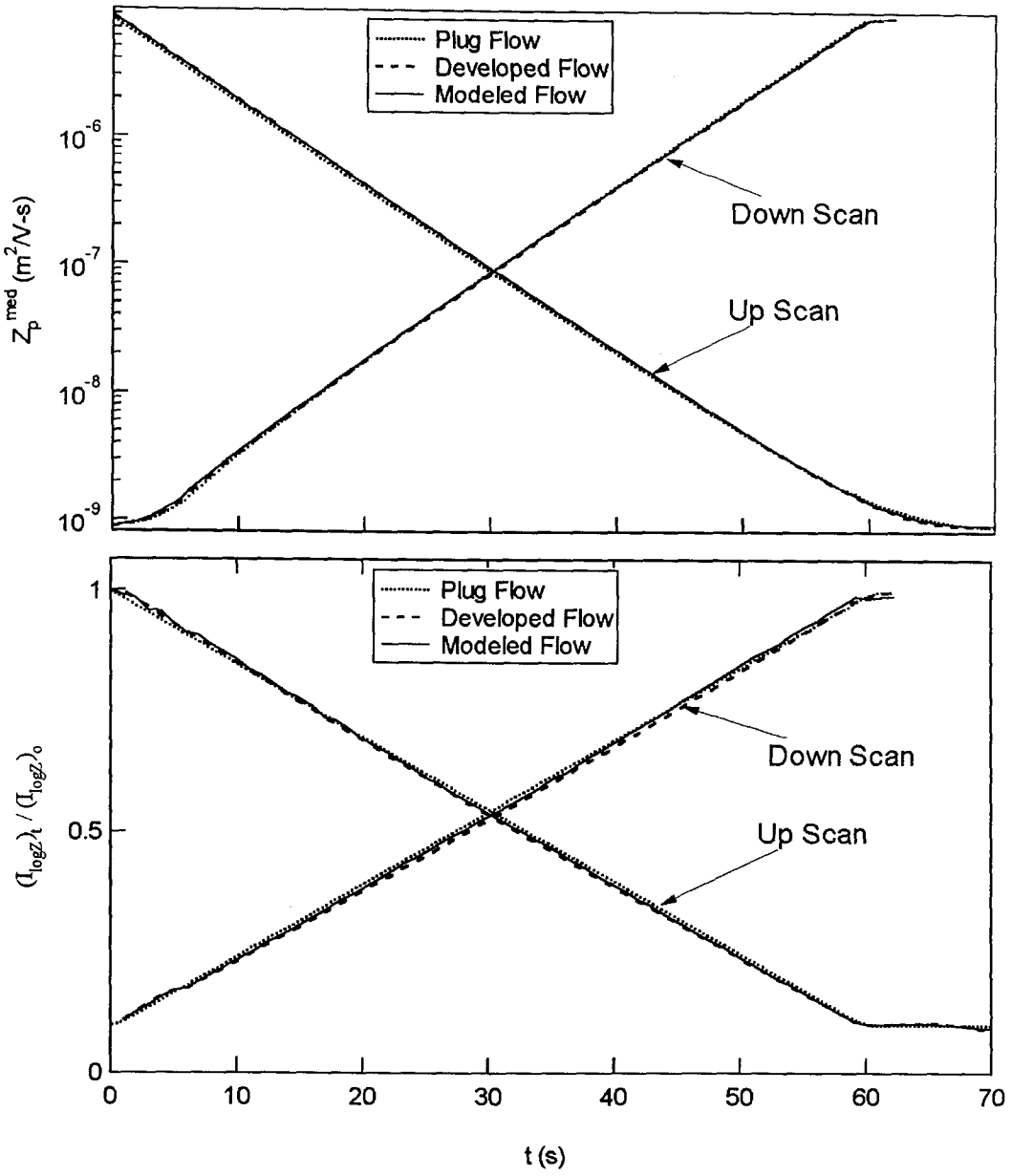


Figure 3.4: Calculated $Z_p^{med}$ and $I_{\log Z}$ for a 60 s scan during which the sheath flow was varied linearly from 2 to 20 L/min as the voltage was ramped from 10 to 10000V. Calculations were performed for plug flow, fully developed flow, and modeled flow.

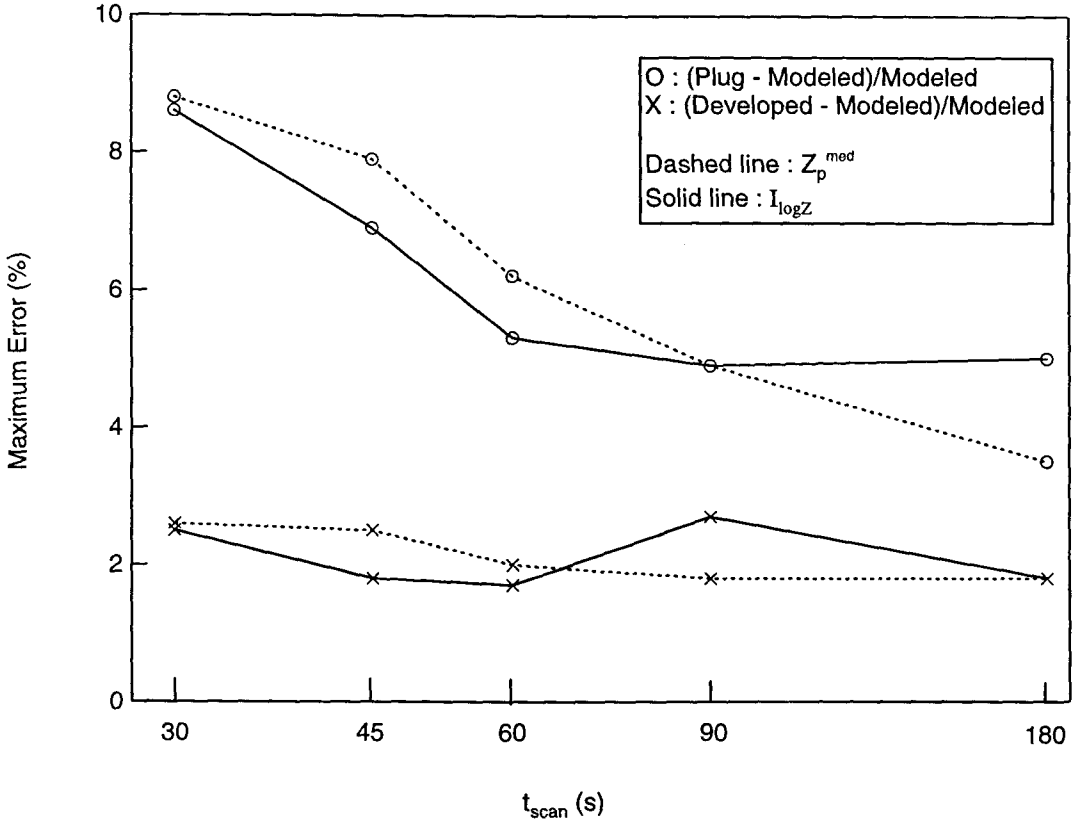


Figure 3.5: Maximum error in the determination of the integral and median mobility of the transfer function from assuming either plug flow or fully developed flow within the DMA.

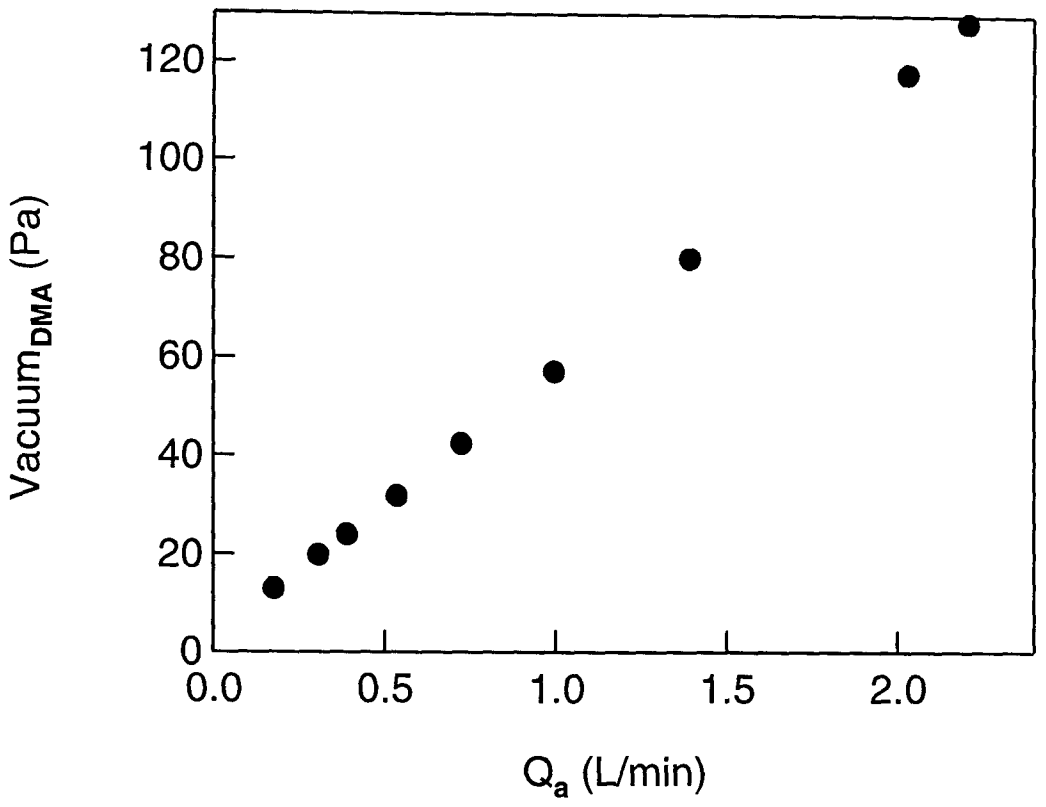


Figure 3.6: Vacuum within the DMA due to the pressure drop associated with the aerosol flow.

approximately 1 $L$. For a one minute linear ramp in flow rate from 2 to 20 L/min, the deviation calculated using Eq. (3.28) between $Q_s$ and $Q_a$ is less than 1%. This discrepancy could become larger if the pressure drops within the DMA or the metering elements were larger, if the DMA volume were larger, of if a faster flow ramp were employed.

The experimental apparatus is illustrated in Figure 3.7. In order to ensure that the sheath and excess flows are balanced as the flows are scanned, a closed loop recycle system (Wang et al., 1992) was used. The variable recycle rate was facilitated by using a regenerative blower (EG&G Rotron HDC, SE12RE21). The regenerative blower is compact and lightweight, and due to the low pressure operation, heats the gas less than the diaphragm pump used in the earlier implementation of sheath air recycle,

reducing the risk of evaporating volatile aerosols in the course of measurement[1]. The aerosol flow was controlled by using a bypass flow that passed through a proportional solenoid valve (MKS 0248A-50000SV). The bypass flow was filtered and combined with the sample flow immediately after exiting the DMA so that the flow entering the TSI 3010 Condensation Particle Counter (CPC) remained constant in spite of the variable flows through the DMA. This not only facilitates the use of a particle detector or other in-line constant-flow apparatus, but also simplifies the final data analysis since the particle losses in the entrance and exit plumbing are constant and the plumbing time between the DMA and the CPC is only a weak function of the flow rates. All volumetric flow rates were measured using differential pressure transducers across laminar flow elements.

LabView (National Instruments) software was used to monitor all parameters and execute all control functions through a laboratory computer. Differential pressure transducer signals were measured and CPC pulses were counted using an A/D card (National Instruments PC-LPM-16), while a 12-bit D/A card (National Instruments AT-AO-6) was used to provide the control voltages to the regenerative blower, control valve, and a high voltage module. The wide dynamic range of the DMA voltage was accommodated by generating a signal proportional to the logarithm of the voltage and using an analog exponentiation circuit to drive the high voltage module (Bertan 602c-100). The control software was based on built-in proportional-integral-differential (PID) controller modules in the LabView software. The data were analyzed in real-time immediately following each scan with a recently developed data inversion routine that accounts for the smearing of the DMA response due to the residence time distribution of the CPC (Russell et al., 1995) and the DMA transfer function.

The performance of the scanning DMA was examined using a mobility classified aerosol. A nebulizer / diffusion dryer system was used to produce a polydisperse aerosol consisting of dry NaCl particles. The dried aerosol was processed through a

[1]It should be noted that for use in a closed loop such as this, the optional seal offered by EG&G Rotron is necessary to prevent leaks that will result in a flow imbalance.

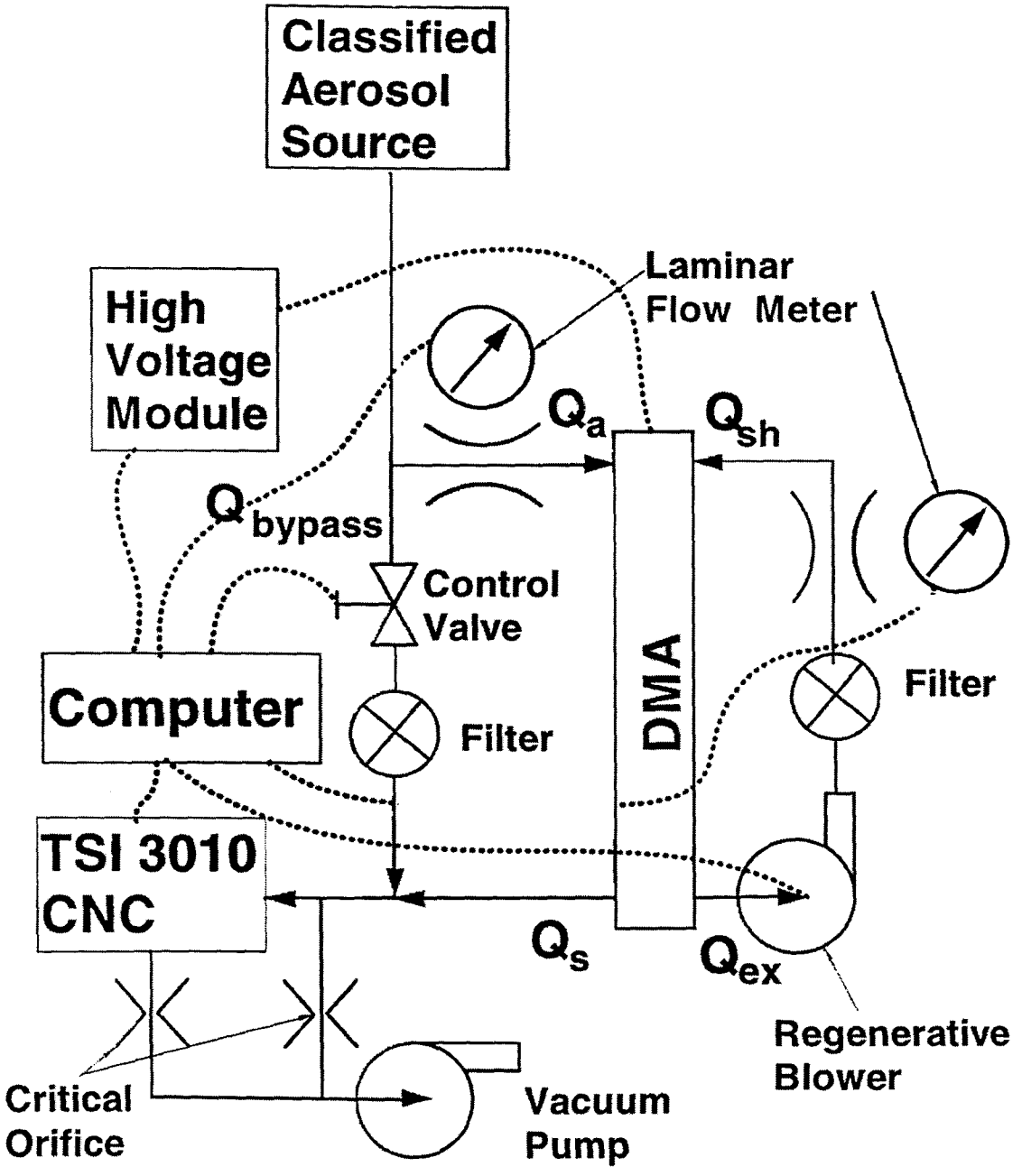


Figure 3.7: Schematic of experimental apparatus.

mixing chamber with a mean residence time of approximately 5 minutes to minimize any fluctuations. A bipolar neutralizer containing 2 mCi of polonium-210 was used to neutralize the aerosol, and a cylindrical DMA identical to the one used for the scanning measurements was used for classification. This source aerosol was found to be extremely stable over a period of hours.

## 3.3 Results and Discussion

For a given set of voltage and flow rate limitations associated with a DMA, there exists an infinite number of possible ramp combinations, several of which are examined below. Although the quantitative results presented are for the cylindrical DMA discussed above, the general trends and benefits described can be achieved with DMAs of any design, subject to the additional constraint that the range and rate of flow rates scanned not lead to flow instabilities.

The most obvious advantage of the flow-scanning mode of DMA operation is the extension of the range of particle sizes that can be accurately measured. Figure 3.8 compares the range of particle measurements that is attainable with a 10 V to $10^4$ V voltage scan with a constant sheath flow rate at an intermediate value of 5 L/min with that covered when the flow rate is decreased with time from 20 L/min to 2 L/min. The minimum classified particle size decreases from 9.8 nm to 4.8 nm, while the maximum particle size increases from 537 nm to 1160 nm when flow-scanning is implemented, extending the sizing range by a factor of 4.4. For a 60 s scan, this factor increases to 6.0 if only those particles that experience the exponential ramp are considered for the voltage-scanning method.

While improving the dynamic range of the DMA may be the most obvious benefit of flow-scanning, it is by no means the only reason for adding this feature. If, as in the present work, the ratio of the aerosol to sheath flow rates is kept constant as the flow rate is scanned, an increase in the flow rate will increase the number of particles reaching the detector. In a clean environment, this can lead to substantial improvements in the uncertainties in number concentration measured. Consider mea-

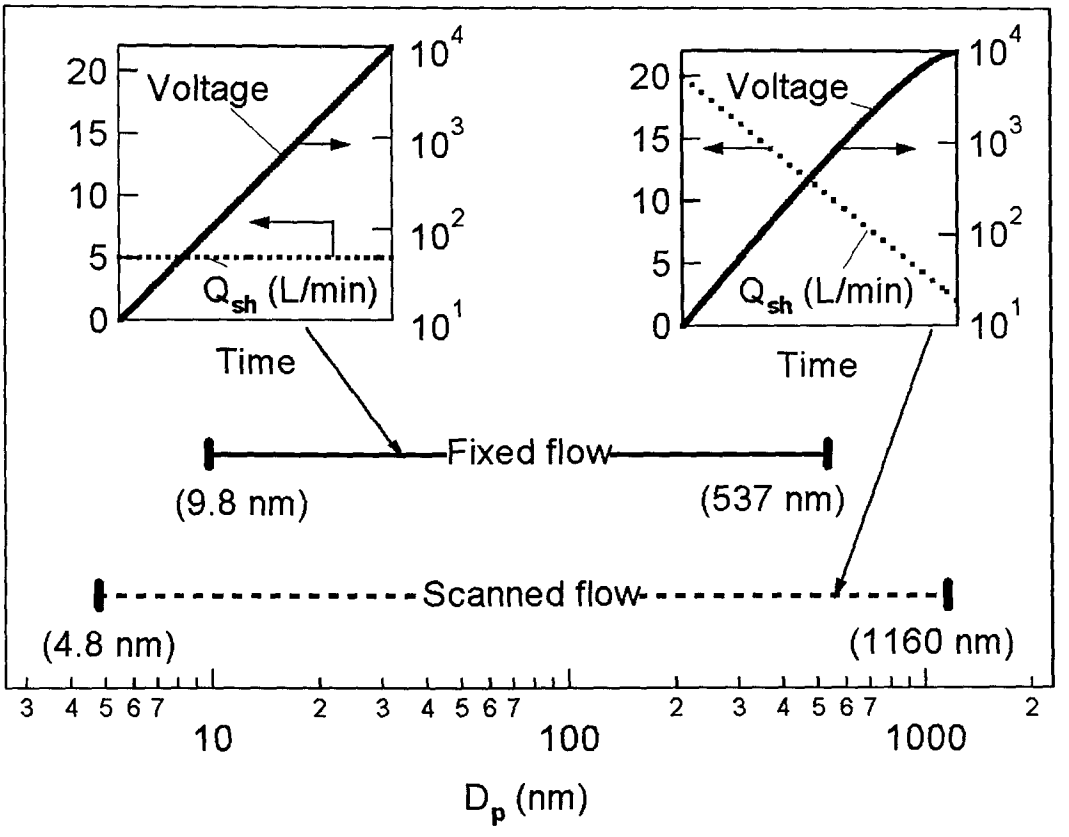


Figure 3.8: Theoretical improvement in the measurable size range of a cylindrical DMA through the implementation of scanning flow rates. The fixed flow and scanning flow ramps used are shown as insets.

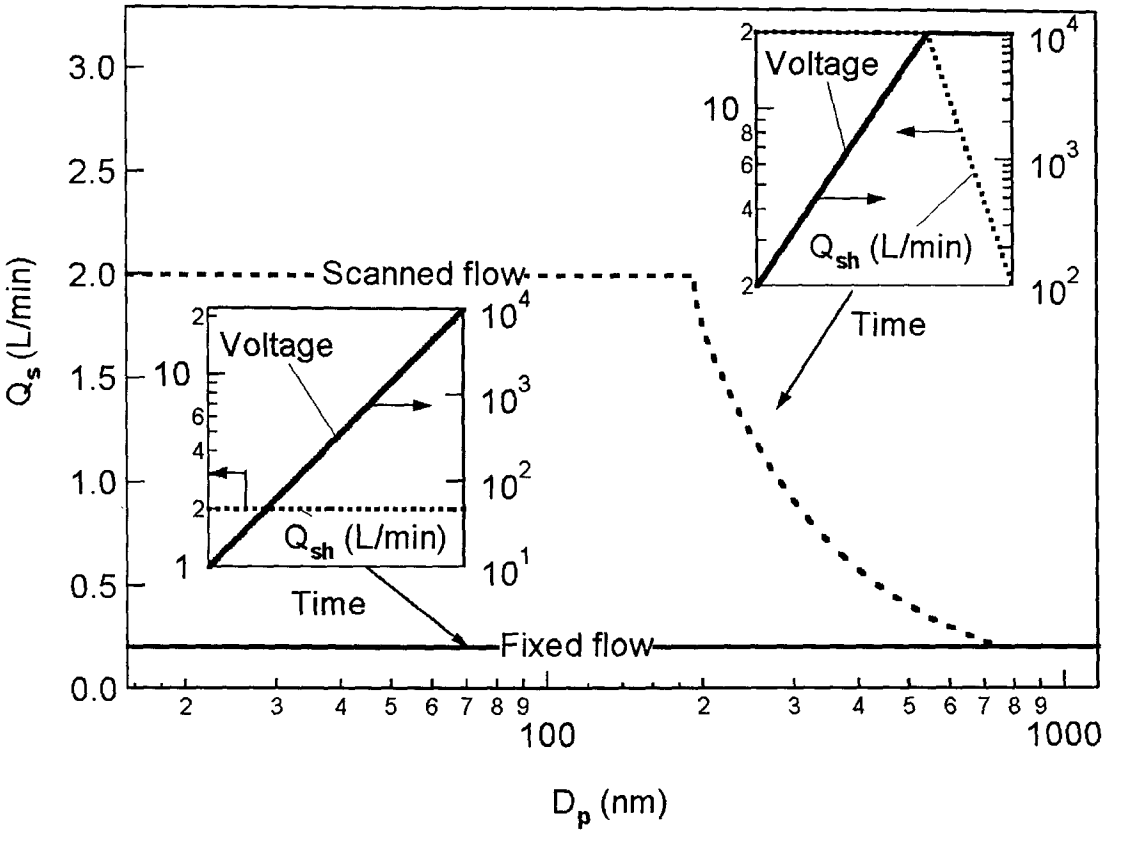


Figure 3.9: Theoretical improvement in the monodisperse flow (and therefore counting statistics) through the implementation of scanning flow rates.

surements with a maximum size of 1 $\mu$m using the present cylindrical DMA. Given the breakdown potential of about 10,000V, classification of these particles requires a flow rate of approximately 2 L/min. In scanning flow operation designed to maximize counting statistics, the flow rate at low voltage is increased by an order of magnitude, to 20 L/min, decreasing only when the particles can no longer be classified at this high flow rate as illustrated in Figure 3.9. This results in a factor of $\sqrt{10}$ decrease in the uncertainty in the estimate of the particle concentration over a wide size range.

The attainable resolution can also be dramatically enhanced by maximizing the classification voltage at every instant in the scan. Figure 3.10 presents a scan designed to increase resolution, while maximizing the flow scan time in order to facilitate

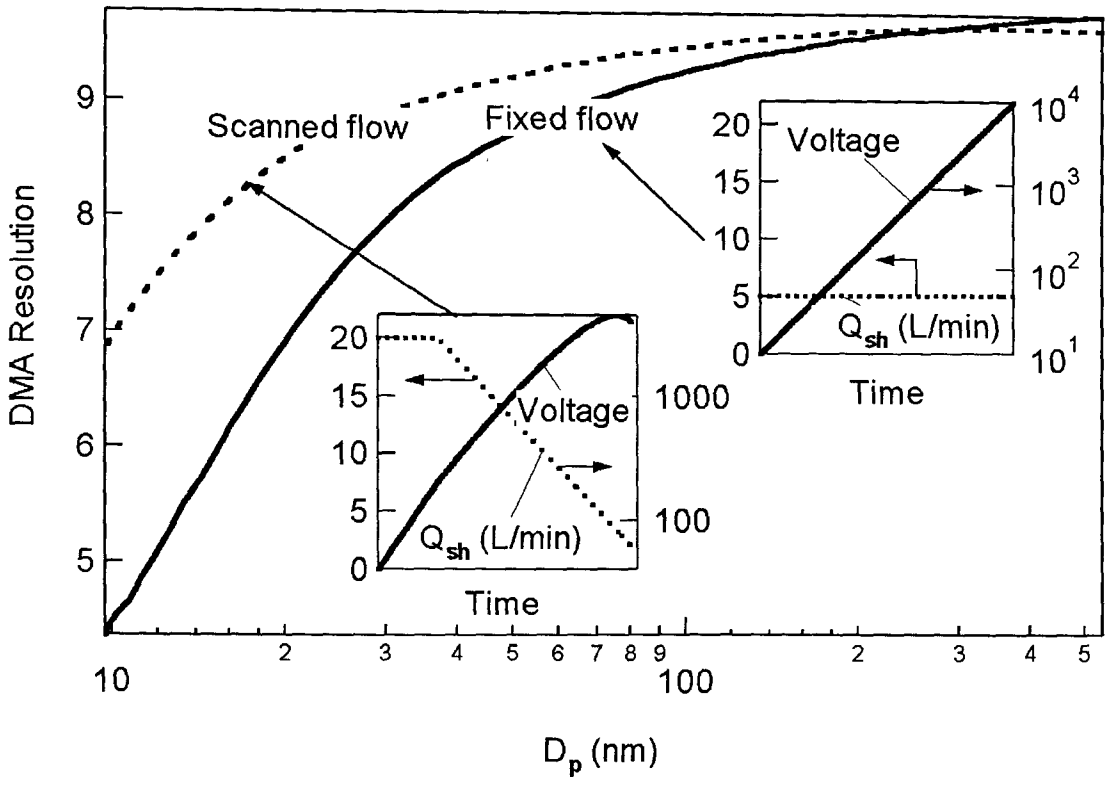


Figure 3.10: Theoretical improvement in the limiting DMA resolution through the implementation of scanning flow rates.

accurate control. In this scan, the flow rate is first maintained at its maximum in order to allow the voltage to be increased as rapidly as possible. When a point is reached at which the resolution is deemed satisfactory, the flow rates begin their linear ramp, slowing the rate of change of the applied voltage. As indicated from calculations based on the Stolzenburg (1988) transfer function, the resolution for this scan profile is dramatically better than that of the conventional fixed flow rate operation, $Q_{sh} = 5$ L/min, over the same range of particle size. The resolution for the smallest particles classified is about 60% higher in the flow-scanning mode than when the voltage is scanned alone.

Experimental implementation of flow-scanning operation of the DMA requires that the flow rates accurately follow the prescribed time profile. The response of the

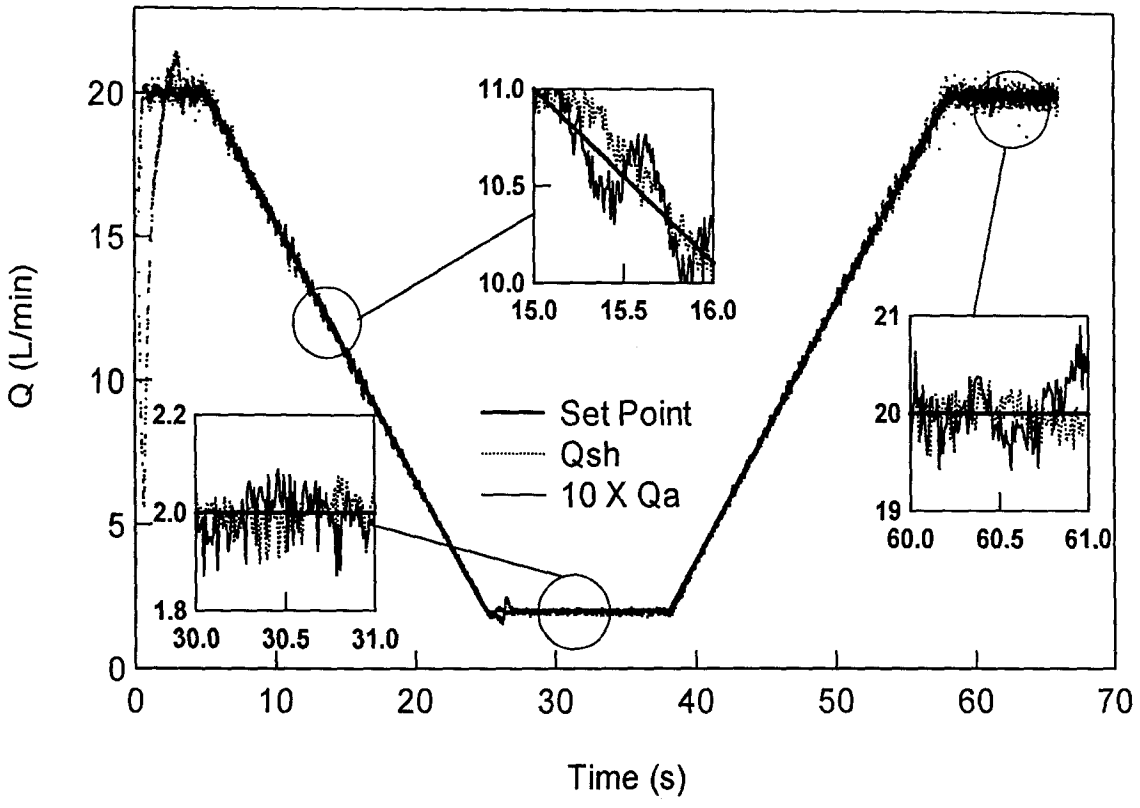


Figure 3.11: Measured sheath and aerosol flow rates during a 20 s linear flow scan. The aerosol flow rate is multiplied by 10 to account for the aerosol to sheath flow ratio of 0.1.

DMA flows to the imposed ramp is shown in Figure 3.11 for a 20 s ramp. A linear ramp has been employed here to facilitate flow control. The sheath flow rate and the aerosol flow rate (multiplied by $10 = \beta^{-1}$) are compared with the set point. The flow control was accurate and stable for this rate of change of the flows. Magnified regions of the profile show that the maximum deviation from the set point was less than 5% over the entire flow rate range. It is the average deviation over the residence time of the particles within the DMA ($\sim$ 1.1 to $\sim$ 11 s) that determines the uncertainty in the measured mobility, and this quantity is much smaller ($\sim$1%).

In order to examine the accuracy of the inverted distributions obtained using a flow ramp, a mobility classified aerosol was measured using a single DMA operated using

Table 3.1: Ramp parameters used for comparison between voltage and flow scans.

| | $V_{\min}$ (volts) | $V_{\max}$ (volts) | $Q_{\min}$ (L/min) | $Q_{\max}$ (L/min) | $t_{scan}$ (sec) |
|---|---|---|---|---|---|
| $V$ Scan | 250 | 2500 | 5.0 | 5.0 | 60 |
| $V+Q$ Scan | 400 | 1200 | 2.5 | 8.0 | 60 |
| $Q$ Scan | 750 | 750 | 2.0 | 20.0 | 60 |

three different ramps in succession. An exponential voltage ramp, an exponential flow ramp, and a coupled voltage / flow ramp are compared in Figure 3.12. In order to compare the flow ramp directly with the voltage ramp, the range of mobilities scanned was limited to the range over which the flow rates could be accurately controlled. Therefore, each of the ramps scanned over approximately one order of magnitude in mobility during a 60 s scan, resulting in an exponential time constant of 26 s. The specific parameters for each of the ramps are listed in Table ??. Agreement between the different ramps is excellent, well within the expected experimental uncertainty.

Faster scans are required to measure rapidly changing aerosols or to achieve acceptable spatial resolution in measurements made aboard aircraft at high flight speeds. Figure 3.13 shows distributions recovered using flow scans of 30 s and 60 s at constant voltage. Although slight deviations appear in the faster measurements, the errors introduced would be acceptable for many applications. As the flow scan time is decreased further, the recovered distributions retain the same mobility peak, but broaden somewhat. Flow irregularities may be responsible for a portion of this broadening, but factors unrelated to the flow ramp itself also contribute, most notably, the finite response time of the condensation nucleus counter. For the flow rate range used in these analyses, ramp times shorter than 10 to 15 s led to poor flow control and significant errors in the final distribution. Better recirculating pumps, control valves, and pressure transducers might alleviate some of this uncertainty.

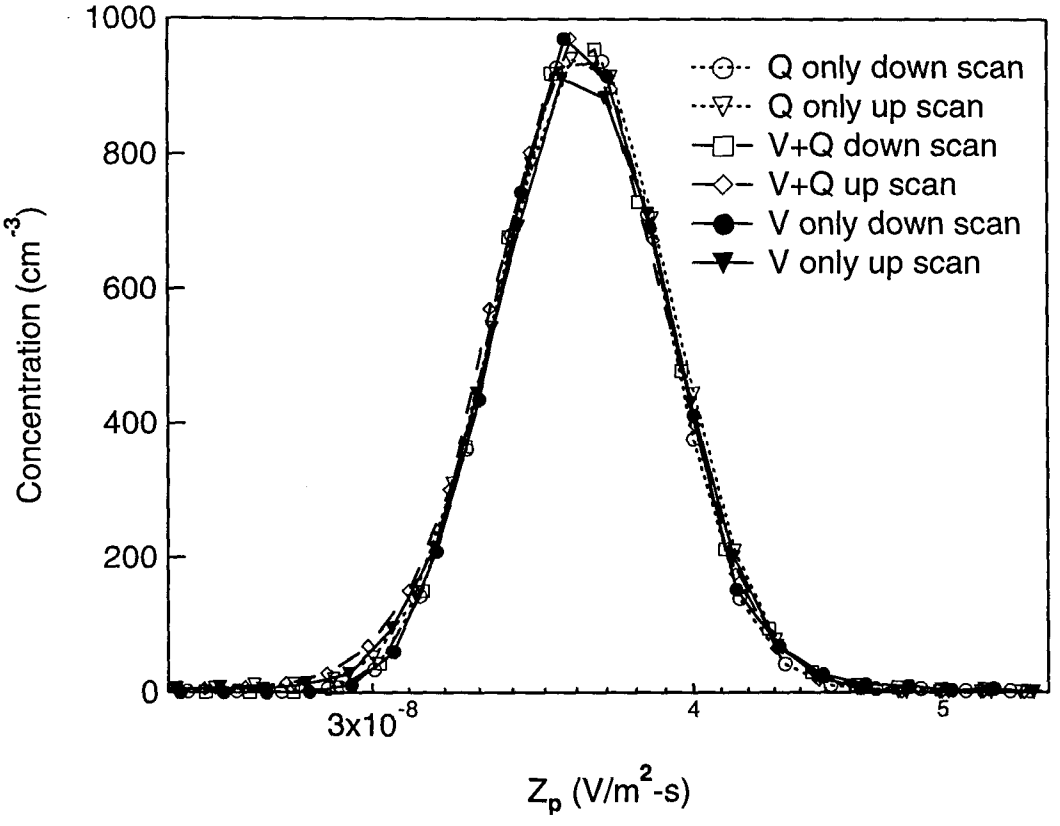


Figure 3.12: Comparison of recovered mobility distributions obtained using a voltage ramp, a flow ramp, and a combined voltage and flow ramp. The ramp parameters used are listed in Table 3.1.

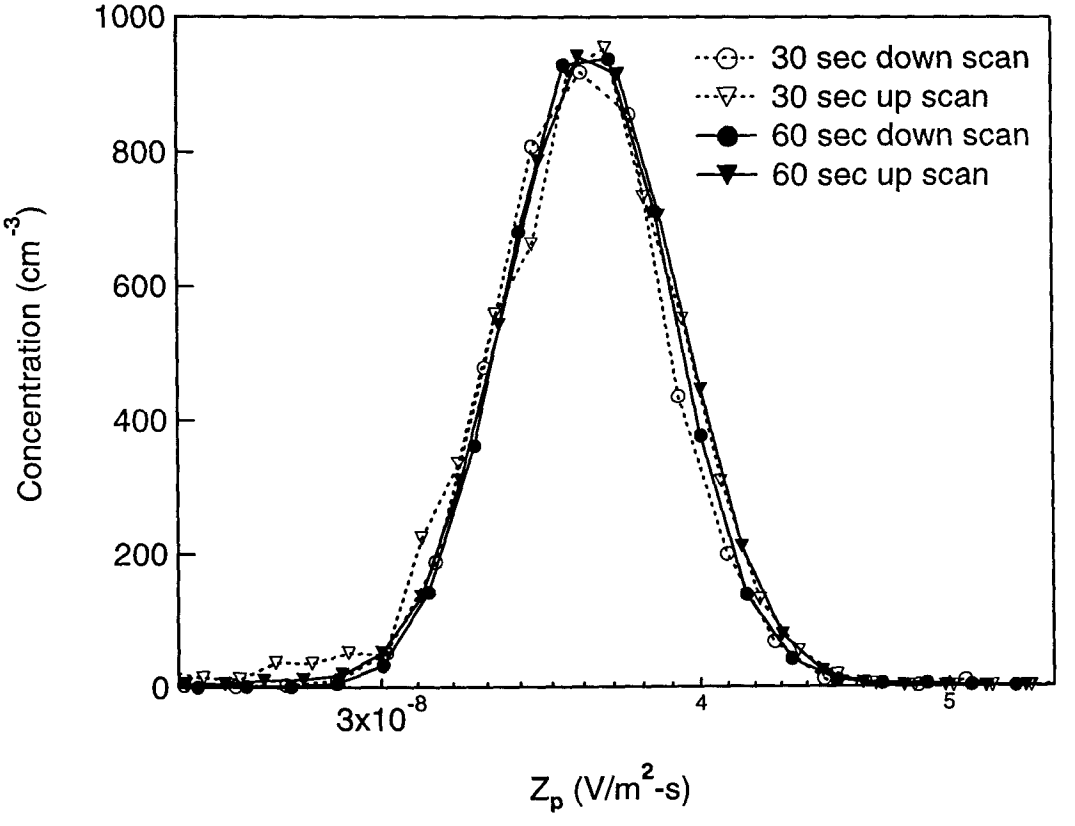


Figure 3.13: Effect of decreasing the flow ramp time from 60 to 30 s. The sheath flow was ramped between 2 and 20 L/min.

## 3.4 Summary

A DMA has been successfully operated with time-varied flow rates. Flow-scanning DMA measurements have several advantages over a DMA that relies only on voltage changes to scan across particle mobility. Constrained only by the requirements that laminar flow be maintained and electrostatic breakdown does not occur, optimization of the flow and voltage ramps can be used to increase the measurable size range, to improve counting statistics, or to enhance DMA resolution. However, unlike the voltage-scanning DMA, classified particles may follow different trajectories through the DMA, thereby complicating data analysis. The result is a trade-off between the benefits of flow-scanning and the associated added uncertainties. Accurate control of the necessary flow rates over an order of magnitude range was accomplished for ramp times as small as 20 s. Excellent agreement was found between mobility distributions recovered from scans utilizing only a voltage ramp, scans utilizing only a flow ramp, and scans utilizing coordinated voltage and flow ramps. Slight deviations in the recovered distributions occur for flow ramp times of 30 s while more pronounced broadening occurs for ramps approaching the limitations of the flow control itself. These benefits require no modification to the DMA and can be achieved without significantly compromising the simplicity and reliability of a conventional DMA measurement system.

# Chapter 4 In Situ Aerosol Size Distributions and Clear Column Radiative Closure During ACE-2

*Tellus*, in press

**Abstract**

As part of the second Aerosol Characterization Experiment (ACE-2) during June and July of 1997, aerosol size distributions were measured on board the CIRPAS *Pelican* aircraft through the use of a DMA and two OPCs. During the campaign, the boundary layer aerosol typically possessed characteristics representative of a background marine aerosol or a continentally influenced aerosol, while the free tropospheric aerosol was characterized by the presence or absence of a Saharan dust layer. A range of radiative closure comparisons were made using the data obtained during vertical profiles flown on four missions. Of particular interest here are the comparisons made between the optical properties as determined through the use of measured aerosol size distributions and those measured directly by an airborne 14-wavelength sunphotometer and three nephelometers. Variations in the relative humidity associated with each of the direct measurements required consideration of the hygroscopic properties of the aerosol for size distribution based calculations. Simultaneous comparison with such a wide range of directly measured optical parameters not only offers evidence of the validity of the physicochemical description of the aerosol when closure is achieved, but also provides insight into potential sources of error when some or all of the comparisons result in disagreement. Agreement between the derived and directly measured optical properties varied for different measurements and for different cases. Averaged over the four case studies, the derived extinction coefficient at 525 nm exceeded that measured by the sunphotometer by 2.5% in the clean boundary layer, but underestimated measurements by 13% during pollution events. For measurements within the free troposphere, the mean derived extinction coefficient was 3.3% and 17% less than that measured by the sunphotometer during dusty and non-dusty conditions, respectively. Likewise, averaged discrepancies between the derived and measured scattering coefficient were -9.6%, + 4.7%, +17%, and -41% for measurements within the clean boundary layer, polluted boundary layer, free troposphere with a dust layer, and free troposphere without a dust layer, respectively. Each of these quantities, as well as the majority of the >100 individual comparisons from which they were averaged, were within estimated uncertainties.

## 4.1 Introduction

Despite an intensive effort to understand the effect of aerosols on regional and global scale radiation budgets, many questions remain unresolved. Among these are questions regarding regionally representative physical and chemical aerosol characteristics and the associated impact of the aerosol on the local radiation balance, directly, due to upscatter and absorption of solar radiation, and, indirectly, through altering cloud properties. Large scale field campaigns have proven to be particularly useful in providing answers in that they allow for simultaneous measurement of a broad spectrum of interrelated gas, aerosol, cloud, and radiation properties. Data resulting from these campaigns can ultimately be incorporated into models that predict radiative forcing resulting from potential changes in aerosol and precursor emissions and into retrieval algorithms necessary for evaluation of remote sensing data. Such models allow extrapolation of local observations to more extensive, climatically significant areas. Prerequisite to successful prediction of any kind, however, is the ability to demonstrate agreement between directly measured optical and cloud formation characteristics and those calculated on the basis of simultaneously measured aerosol microphysical properties. This so-called closure has been attempted with varying degrees of success by a number of research groups using a variety of sets of overdetermined measurements and computational techniques (Clarke et al., 1996; Hoff et al., 1996; Hegg et al., 1997; Howell and Huebert, 1998; Redemann et al., 1998).

The variety of measurements made during ACE-2 provided a unique opportunity to attempt a range of aerosol radiative closure comparisons. Among these comparisons, a distinction can be made between those of an individual optical measurement and the associated quantity calculated from the physicochemical properties of the aerosol, and those from multiple direct measurements. In theory, the latter type of comparison could be accomplished with no knowledge of aerosol microphysics. In practice, however, even for the relatively straightforward comparison between measured aerosol scattering and absorption coefficients and simultaneously measured extinction coefficient, an understanding of the aerosol size distribution is necessary to

account for such biases as the angular sensitivity associated with nephelometers, or the expected growth, evaporation, or loss of particles associated with either nephelometers or absorption photometers. The same conclusion is true for direct comparisons with satellite or lidar data, which, in general, require knowledge of such quantities as the aerosol scattering phase function and single scatter albedo, which, as before, could be measured directly, but in practice, generally require a description of the aerosol microphysics. As a result, essentially all potential comparisons, to some extent, necessitate an understanding of the aerosol itself. Assumptions made for specific classes of aerosols can be used in place of direct size distribution and composition measurements, but likely at the expense of accuracy. The focus here is on the radiative closure between directly measured scattering and extinction coefficients and those calculated based on the aerosol size distributions. Schmid et al. (2000) expand upon this analysis by utilizing the aerosol size distributions described here to aid in the evaluation of closure between additional measurements.

The second Aerosol Characterization Experiment (ACE-2) was conducted in June and July of 1997 in the Northeastern Atlantic in a region bounded roughly by the Canary Islands of Spain to the south and Sagres, Portugal to the north. A more detailed overview of the objectives, experiments, and outcome of the campaign is described by Raes et al. (2000). During the summer months, air masses arriving in the studied area have a variety of origins, including the central North Atlantic, Western Europe, and North Africa, which bring background marine, aged pollution, and mineral dust aerosols, respectively. During this campaign, the CIRPAS *Pelican* flew 21 scientific missions out of Tenerife, Spain (one of the Canary Islands), as part of the coordinated LAGRANGIAN, CLEARCOLUMN, and CLOUDYCOLUMN experiments, which are described by Johnson et al.(2000), Heintzenberg and Russell (2000), and Brenguier et al. (2000). The relatively large number of flights resulted in a data set sufficient to describe not only the average characteristics of each of the aerosol types described but also the variability observed within these broad categories. This paper discusses aerosol size distributions measured on the *Pelican* during ACE-2 and clear column radiative closure for four flights that are thought to represent the

range of conditions prevalent in the region of study.

## 4.2 Instrumentation and Analysis

### 4.2.1 Aerosol Size Measurements

#### ACAD

The differential mobility analyzer (DMA) system used on board the *Pelican* was the Caltech Automated Classified Aerosol Detector (ACAD), which is the improved successor to a package operated during the MAST, ACE-1, and TARFOX experiments (Russell et al., 1996b). The key components of the instrument are a radial DMA designed for classification of particles smaller than a few tenths of a micrometer diameter, and a modified TSI 3010 condensation particle counter capable of a detection efficiency exceeding 90% for 4.5 nm diameter particles. Active flow controllers maintained each of the system's flow rates to within 1% of their specified values. A computer-controlled, high-resolution, 18-bit digital to analog chip was used to scan the voltage applied to the DMA over 45 s. To compensate for the reduction in electric field strength sufficient to result in arcing within the DMA with decreasing air density, while at the same time extending the measured size range to the maximum particle size possible, the peak applied voltage was varied automatically. The resulting size range analyzed is approximately 5 to 190 nm and varies relatively little with changing altitude. The ACAD was calibrated prior to the ACE-2 period and accurately recovered both the peak size and total number concentration of monodisperse calibration aerosols as small as 7 nm diameter. The sample flow for the ACAD entered through a community inlet and subsequently passed through a cyclone with a nominal 2.5 $\mu$m cut size, although this cutoff had a negligible effect on the small particles of interest.

## PCASP

The first of two optical particle counters (OPCs) utilized during ACE-2 was the Passive Cavity Aerosol Spectrometer Probe (PCASP-100X) manufactured by Particle Measuring Systems (PMS). The PCASP makes use of a large scattered light collection area to enable detection of particles as small as approximately 0.1 $\mu$m diameter. The PCASP sample inlet is designed to minimize inertial particle losses, thereby enabling penetration and detection of particles exceeding 3 $\mu$m diameter. As with all OPCs, inference of particle size with the PCASP is complicated by the fact that the light scattered by a particle is a function not only of its size, but also of its index of refraction and shape. To account for the influence of particle refractive index, the size calibration performed prior to ACE-2 using polystyrene latex particles (PSL, $m = 1.59 - 0i$) was used along with Mie theory to calculate the expected scattered light intensity over the PCASP's collection area corresponding to each of the particle size bins. Several hundred effective calibrations were then generated for the range of complex refractive indices expected by iteratively calculating the particle size necessary to result in a collected light intensity equivalent to that calculated using the original PSL calibration. Figure 4.1 shows the relationship between the size as calibrated with PSL and the corresponding effective calculated size. Underestimation of particle size based on PSL calibration, as seen in this figure, is representative of almost all relevant refractive indices. Assumed aerosol chemical composition, which is discussed below, along with the relative humidity within the instrument, is then used to determine a sampled particle's refractive index, from which size can be determined through the use of the generated effective calibrations.

Tandem differential mobility analyzer (TDMA) experiments conducted in the boundary layer at a site on Tenerife during ACE-2 indicated that 80% or more of the particles were hygroscopic in nature, having wet diameters (RH $\sim$ 80 - 90%) typically in excess of 1.5 times larger than their corresponding dry diameters (RH $\sim$ 10%) (Swietlicki et al., 2000). Particles of this type are expected to be spherical at the relative humidity range of approximately 70 - 90% characteristic of the bound-

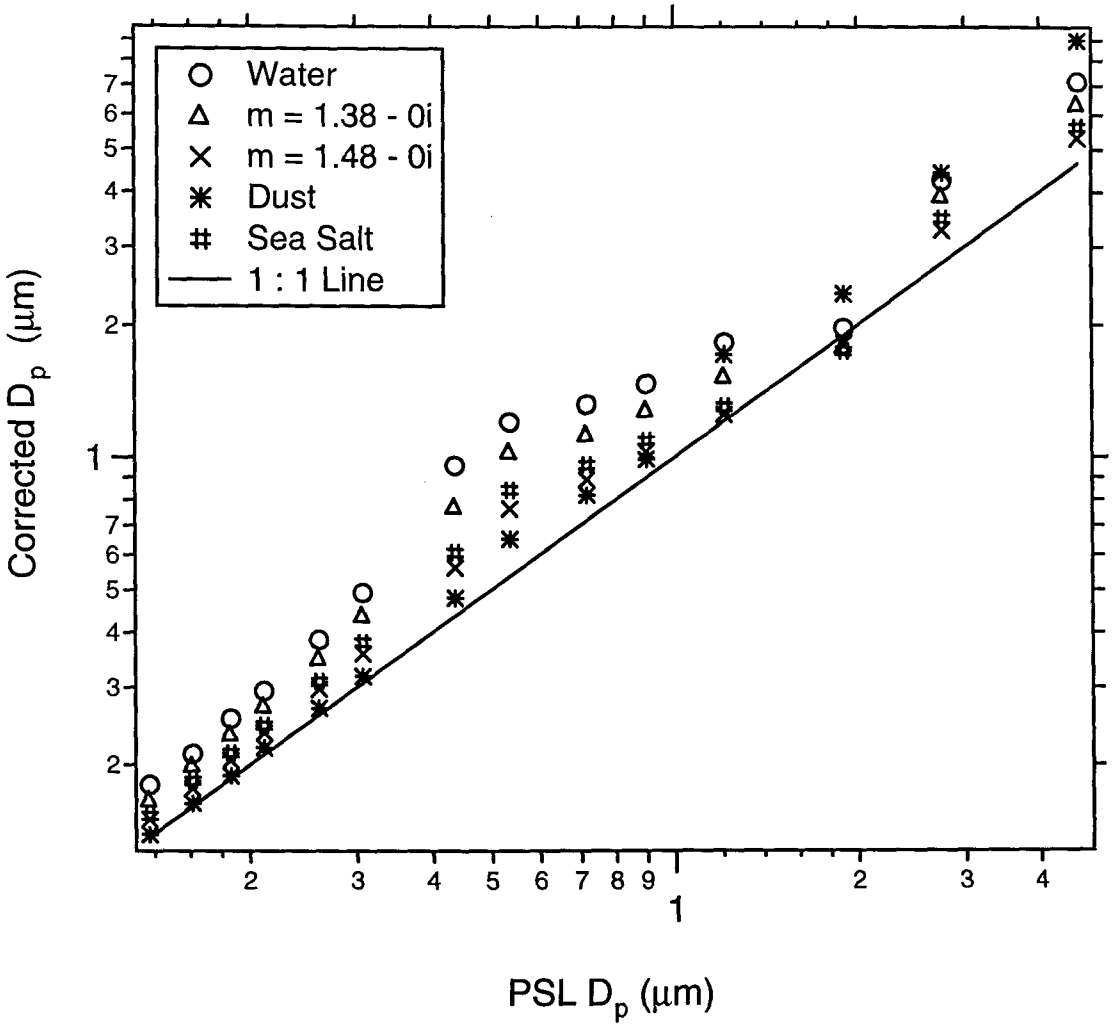


Figure 4.1: Theoretical particle size required to result in the same collected light intensity in the PCASP as a PSL particle of a given size.

ary layer. While these particles will partially evaporate as a result of the heating associated with the PCASP as discussed below, they are expected to remain spherical since the corresponding range of instrument humidity is approximately 55 - 75%, which is above the crystallization point for the species of interest. Therefore, for the boundary layer aerosol, the Mie theory calculations performed are applicable. On the other hand, dust, crystalline salt, and externally mixed carbon particles present in the free troposphere are not necessarily spherical. To estimate the effect this would have on particle size assignment by the PCASP, the modeled phase functions of nonspherical particles described by Mishchenko et al. (1997) were considered. In general, the phase functions resulting from particles much smaller than the wavelength of light used (633 nm) closely approach those of ideal spheres. Assuming that larger, dust-like particles are spherical will result in an over-prediction of the phase function between about 30 and 80°, and an even larger under-prediction between approximately 90 and 150°, as shown in Figure 4.2 for a distribution of particles thought to be representative of mineral dust. Fortunately, the PCASP collection geometry, which receives light scattered between 35 and 120°, results in a partial cancellation of these opposing discrepancies. The effective particle sizes corresponding to each of the bins as described above are found to vary typically by less than 5% from those calculated using Mie theory.

### FSSP

Mounted on the wing opposite to the PCASP was a PMS Forward Scattering Spectrometer Probe (FSSP-100). The FSSP, which makes use of an external laser / detector, causes only minimal perturbation of particles or droplets of 20 $\mu$m diameter or more. Since the *Pelican* did not sample in-cloud properties for any extended period of time, the size range measured with the FSSP during ACE-2 differed from that more commonly measured for cloud droplet sizing, and instead particles ranging from 0.5 to 8.0 $\mu$m were binned in 16 diameter intervals. However, measurement of the scattered intensity in the near forward direction, as with the FSSP, results in significant oscillations superimposed on the general increase in intensity with particle

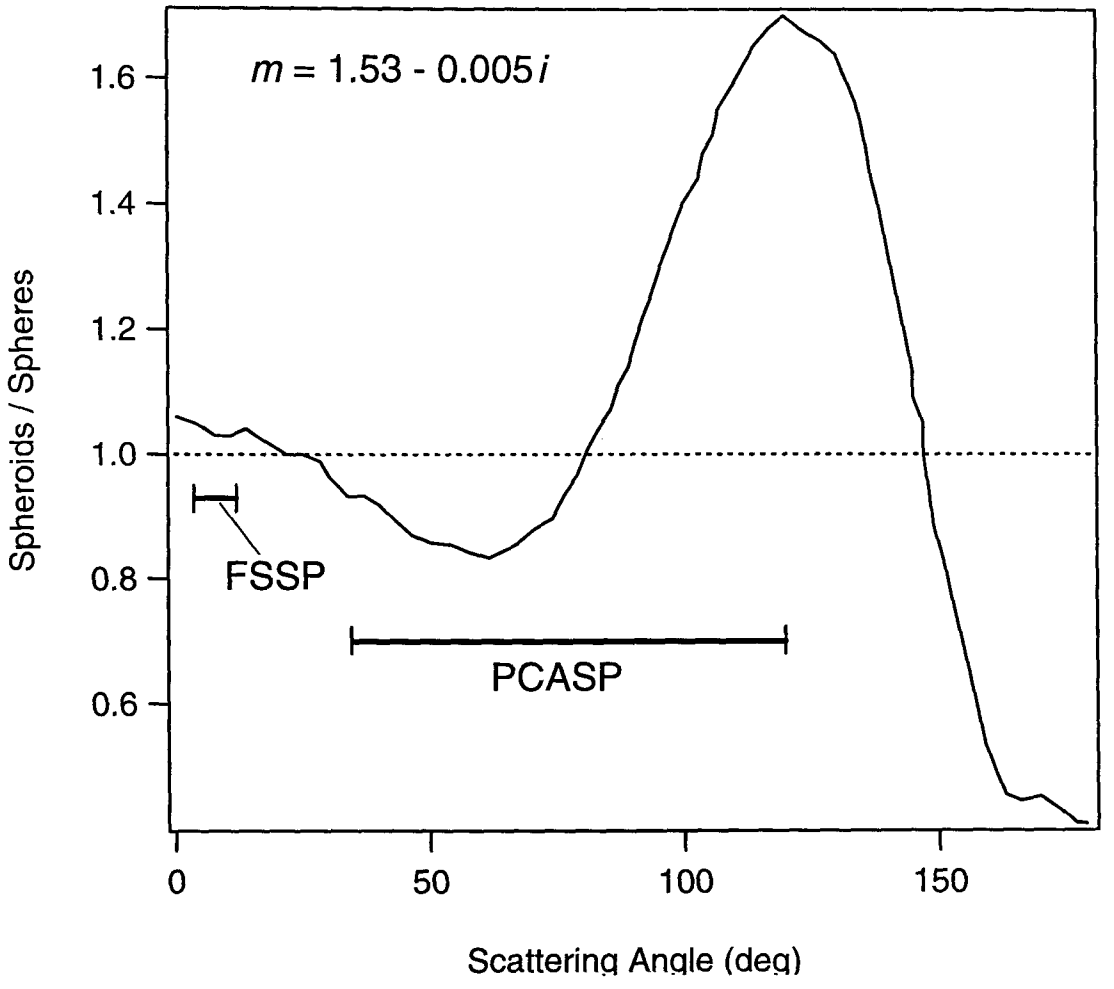


Figure 4.2: Ratio of nonspherical to spherical phase functions published by Mishchenko et al. (1997). These data correspond to a distribution of particles thought to be representative of mineral dust aerosols. Also shown are the collection angles for both the PCASP and the FSSP.

size in the range used, as can be seen in Figure 4.3. As with the PCASP, particle refractive index influences the measurement, but the lack of a unique particle size corresponding to certain values of scattered intensity prohibits generation of meaningful effective calibrations as described in the previous section. Rather than using all 16 intervals, 3 composite bins were chosen that have little overlap in the corresponding theoretical scattering intensity. These bins have nominal particle diameter ranges of 0.5 to 3.0 $\mu$m, 3.0 to 4.5 $\mu$m, and 4.5 to 8.0 $\mu$m. Similar to the PCASP, the sizing ability of the FSSP is expected to be largely unaffected by nonspherical particles, but unlike the PCASP, this is not due to offsetting errors, but rather is a result of the weak influence of particle shape on the near forward (4 to 12°) scattering measured as shown in Figure 4.2.

The FSSP was only operational during the first nine flights. For later missions, size distributions measured by the PCASP were extrapolated to account for scattering and absorption by particles larger than the $\sim$ 3 to 5 $\mu$m limit (depending on the refractive index) of the PCASP. Boundary layer extrapolations were based on trends observed while the FSSP was operational, whereas extrapolation in the dust layers encountered were based on FSSP measurements made on board the *Merlin* aircraft (Brenguier, 2000). Fits used for both of the extrapolations are shown in Figure 4.4. The expected error from these extrapolations will be discussed in the individual case studies.

### 4.2.2 Integration of Sizing Measurements

Combining the three aerosol size distribution measurements into a consistent data set requires knowledge of the influence of the sampling process on each particle prior to detection. Typically, the most significant effect is the potential growth or evaporation of a hygroscopic particle. No significant heating is expected to be associated with the FSSP, and therefore, the sampled particles are thought to be at equilibrium at ambient relative humidity. The sample stream reaching the DMA was, in general, several degrees Celsius above ambient, resulting in a reduced relative humidity, and

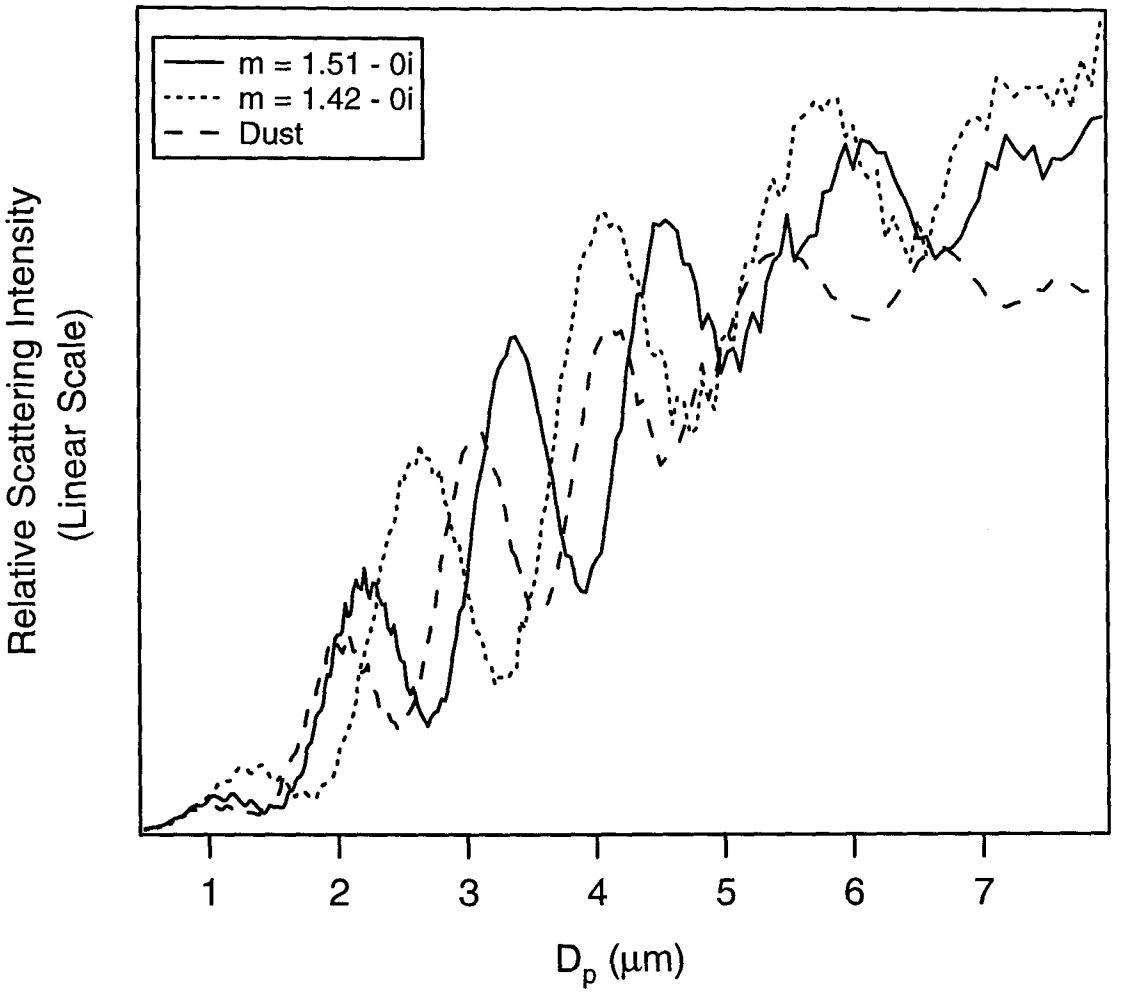


Figure 4.3: Collected scattered light intensity as a function of particle size and index of refraction for the FSSP.

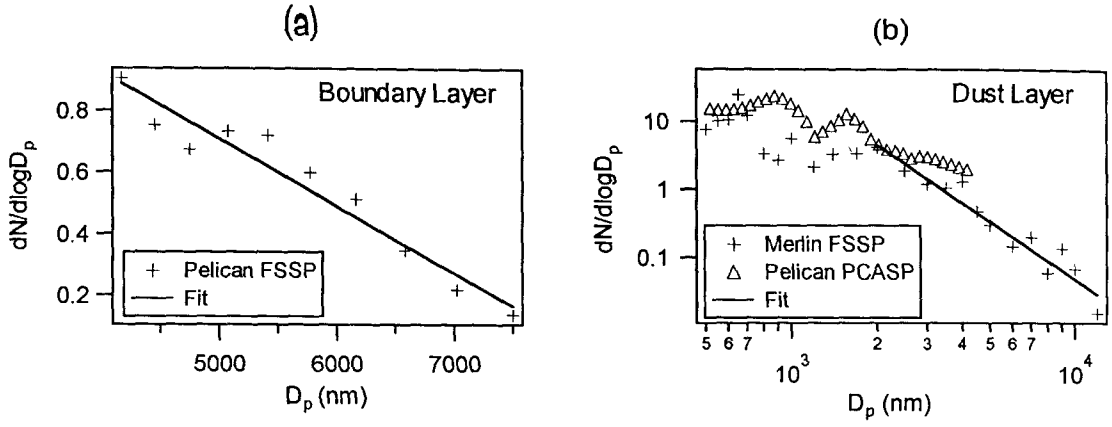


Figure 4.4: Extrapolations used during ACE-2 when no FSSP data were available. The extrapolation used for boundary layer measurements (a) was based on measurements made on the *Pelican* during similar conditions. That for the dust layers (b) was based on data obtained on board the *Merlin* (Brenguier et al., this issue) while measuring the same dust event as the Pelican.

consequently, partial evaporation of some particles. However, the degree of evaporation could be predicted since relative humidity was measured at the exit of the DMA. During the ACE-2 experiment, the PCASP de-icing heaters remained off to allow sampling of an aerosol more closely resembling that present at ambient conditions. Without the heaters, assessing the degree to which particles evaporate within the PCASP is more complicated as no direct measurement of humidity is made, and kinetic limitations on evaporation may be important. Upon entering the inlet of the PCASP, the sampled air is heated by approximately 1.5 °C due to the ram-heating associated with a decelerating flow, although a fraction of this ram heating is potentially offset by the subsequent acceleration of the gas as it enters the sampling cavity. Additionally, the sheath air that is used to focus the sample within the view volume is heated since it is largely recirculated and passes through a pump during each loop. This warm sheath air initially surrounds the intake tube and may therefore transfer heat to the sample indirectly by heating the tubing walls. Sheath and sample flows then join and are accelerated through a nozzle into the sample chamber during which time the intimate contact between the two air streams may lead to further heating.

Biswas et al. (1987) analyzed this effect in a Royco 226 OPC, which has a flow system very similar to that of the PCASP, and found that the sheath air was heated by 2 to 3 °C. The time the sample stream spends in direct contact with the sheath air may be insufficient to allow larger particles to come to equilibrium under the new conditions. Therefore, in order for larger particles to equilibrate at the relative humidity associated with the heated sheath air, the discussed transfer of heat across the intake tubing walls would be necessary. While these uncertainties related to the heating within the PCASP have not been fully resolved, a combined ram effect and sheath air heating of 3.5 °C was assumed. The sensitivity of calculated optical properties of the aerosol to this assumption is discussed in the results.

Adjusting for these relative humidity differences requires knowledge of the behavior of the sampled particles, which, in turn, generally necessitates an understanding of the chemical make-up of the individual particles, information not often available at the same temporal and size resolution as the size measurements, as is the case here. Therefore, for each flight, size-dependent aerosol composition for the boundary layer and free troposphere was assumed using available measurements. These chemical compositions also allow for determination of the hygroscopic and optical properties needed for comparisons with the various optical measurements. As part of the ACE-2 study, aerosol chemical composition measurements were made at several land-based locations, including two sites in particular on Tenerife: Punta Del Hidalgo (PDH) located at the Northern end of the island at an elevation of 30 m, and Izaña (IZO) located at 2360 m along a ridge in the central region of the island. The prevailing low-level winds in this region of the Atlantic generally come from the north and therefore PDH served as the first area of the island arriving air masses encountered and thus provided details of the undisturbed marine boundary layer. IZO often experienced upslope winds throughout the day, while measurements made during the night were thought to be characteristic of the undisturbed free troposphere. Particulate chemical species measured at both of these locations included $NH_4^+$, $SO_4^{2-}$, $Na^+$, $Cl^-$, and both elemental (commonly referred to as black) and organic carbon (Putaud et al., 2000). A distinction between fine and coarse mode aerosols was made using nominal

particle cut diameters of 1 $\mu$m and 2 $\mu$m for the PDH and IZO samples, respectively.

Using these data, size-resolved chemical compositions were then generated corresponding to the boundary layer and free troposphere for each flight. This was accomplished through the use of assumptions relating the concentrations of the various components, while also requiring that the fine and coarse mass fractions calculated using these assumed compositions, in conjunction with the measured size distributions, agreed with the actual measurements made at PDH and IZO. Compositions for the free tropospheric aerosol during Saharan dust episodes were based in part on the measurements made at IZO, but it was assumed that the majority of the supermicrometer mass resulted from dust particles. This assumption was necessary as the filter and impactor analyses performed did not account for the total mass associated with the dust. The assumed degree of neutralization of the sulfates ($H_2SO_4$, $NH_4HSO_4$, or $(NH_4)_2SO_4$) was based largely on the trends observed in the ratio of ammonium to sulfate relative to particle size. The similar hygroscopic properties of each of these compounds limits the error in growth / evaporation calculations associated with an inaccurate assumption. Examples of aerosol chemical compositions are presented for each of the four case studies described below. Filter measurements were also made on board the *Pelican* during ACE-2 (Schmeling et al., 2000). However, since these samples were not size-resolved, and often combined the contributions from the free troposphere and boundary layer, they did not provide the necessary information for size-resolved compositions.

External mixtures of sea salt and sulfate particles were assumed to enable the use of published single salt solution thermodynamics data for particle growth / evaporation calculations. While this assumption may lead to some error if there is substantial internal mixing of sea salt and sulfates, it has been shown by Tang (1996) that the degree of mixing leads to insignificant differences in hygroscopic or optical properties of common sulfates and nitrates. Dust particles were also assumed to be mixed externally, which is supported in part by TDMA data taken on Tenerife during ACE-2, which consistently showed hygroscopic and non-hygroscopic fractions with little or no overlap (Swietlicki et al., 2000). Organic and elemental carbon were assumed to be

predominantly internally mixed with the sulfates, although a specified fraction was also considered to be internally mixed with the sea salt, and the remainder externally mixed. That elemental carbon is expected to be internally mixed with the salt particles is supported by volatility measurements made under similar conditions in the North Atlantic, which showed evidence of a non-volatile residual that was present in the majority of particles and that was composed partially or entirely of elemental carbon (Clarke et al., 1996). No similar evidence is available regarding the mixing state of particulate organic carbon, but it is thought that it is emitted largely from land sources (Cachier et al., 1986) and therefore has had a considerable amount of time en route to accumulate salt species through coagulation and condensation. All internally mixed particles were considered to be homogeneous, an assumption that most likely does not result in substantial errors in optical calculations, as is discussed below.

Given the assumed aerosol composition, the response of a size distribution to changes in relative humidity can be deduced. The hygroscopic behavior of each of the salts considered can be predicted by the following relationship that combines solute and Kelvin terms,

$$\frac{RH}{\gamma_w x_w} = \exp\left(\frac{4\sigma_s MW_w}{RT\rho_s D_p}\right), \tag{4.1}$$

where $RH$ is the relative humidity, $\gamma_w$ the activity coefficient of the water, $x_w$ the mole fraction of water, $\sigma_s$ the surface tension of the solution, $MW_w$ the molecular weight of water, $R$ the ideal gas constant, $T$ the temperature, $\rho_s$ the solution density, and $D_p$ the particle diameter. Data obtained through the use of an electrodynamic balance have provided empirical relationships describing the activity and density of concentrated, and even supersaturated, aqueous mixtures of common salts (Tang and Munkelwitz, 1994; Tang, 1996) as well as actual sea salt (Tang et al., 1997). Surface tension increases roughly linearly with increasing solute concentration (Pruppacher and Klett, 1997). An iterative algorithm can then be implemented to determine the size change a particle of known composition undergoes resulting from variations in

relative humidity. For aqueous particles present at relative humidities between the crystallization and deliquescence humidities for the particular salt, a supersaturated solution is assumed. In essence, this is equivalent to assuming all particles above their crystallization point have previously deliquesced. The observed relative humidity within the boundary layer during the study had a mean and standard deviation of 78±7%, which is sufficient for deliquescence for most of the salts considered. For periods during which the humidity was slightly lower than the deliquescence point of a given salt species, this assumption may result in some error, although many of the particles are still likely to have been previously exposed to sufficiently high humidities. The corresponding mean and standard deviation of the relative humidity in the free troposphere was 18±10%, which is below the crystallization point for most of the salts considered and would result in minimal growth even for the non-crystallized aerosols. Dust, elemental carbon, and organic carbon were assumed to be non-hygroscopic, and, if internally mixed, were only considered to affect the Kelvin term in Equation (4.1). While mineral dust and elemental carbon are expected to be primarily hydrophobic, this assumption is known not to hold for some organic species likely to be present (Saxena et al., 1995). Although there are little direct data supporting or disputing this approximation, it is indirectly supported by the inverse, though weak, relationship between the organic mass fraction measured at PDH and the average TDMA analyzed growth factor of the hygroscopic fraction during the same time period.

Given the assumed or measured relative humidity within each of the sizing instruments, the evaporation / growth adjustments described above can be made to the corresponding data to determine the complete aerosol size distribution expected to be present at ambient conditions. For the typical 15 - 20% decrease in relative humidity associated with the PCASP, the relative magnitude of this adjustment for an aqueous ammonium sulfate particle ranges from approximately 10 to 25% corresponding, respectively, to an ambient humidity range of 70 to 90%. For particle size ranges over which the DMA and PCASP data overlapped, the two measurements were simply averaged. The consistent agreement between the PCASP and the FSSP at

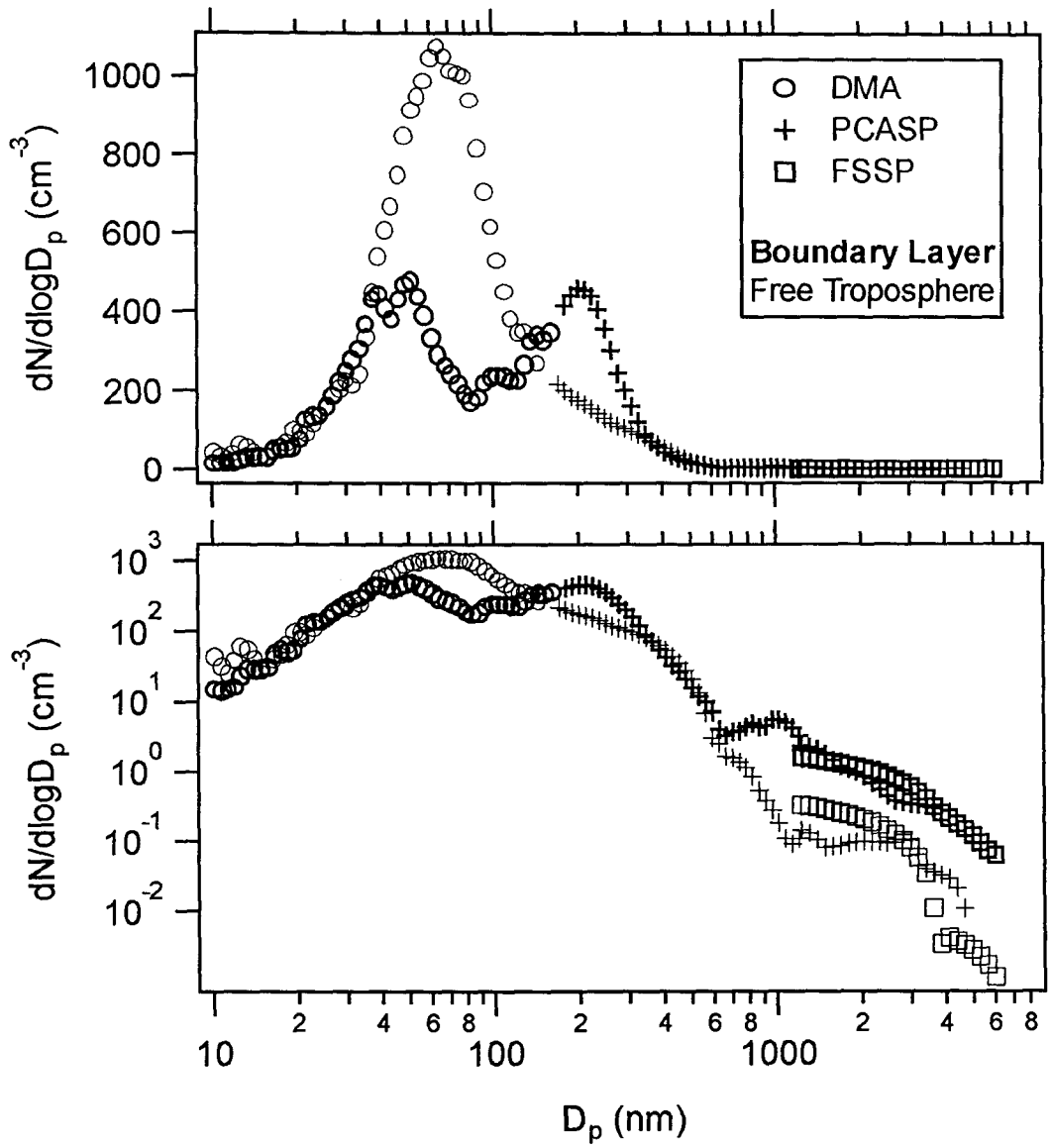


Figure 4.5: Comparison of the recovered size distributions from the DMA, PCASP, and FSSP both in the boundary layer and the free troposphere during ACE-2. Each of the distributions was either measured at, or adjusted, to ambient relative humidity.

approximately 2.5 $\mu$m was used as a cutoff point, below which the PCASP data were assumed to be more accurate, and above which the FSSP data (when available) were used. To allow simple averaging and comparison of data, all of the size distributions were interpolated onto a fixed set of logarithmically spaced diameters. Generally, agreement in the number concentration measured by the DMA and the PCASP was within 10 to 20% in the overlapping region. For measurements within the boundary layer, discrepancies between the concentrations recovered by the PCASP and those recovered by the FSSP were usually less than 30% in the overlapping range, whereas for measurements made in the free troposphere the corresponding discrepancies occasionally exceeded a factor of 2, at least in part due to poor counting statistics. Figure 4.5 shows the agreement between the size distributions from the three instruments during the flight on June 21. Among the platform intercomparisons performed during ACE-2, those with the land site at PDH and with the C-130 were of particular interest for the size distribution measurements, as similar data were taken on each platform. Figure 4.6 shows the results of these intercomparisons conducted on July 14. For direct comparison with the low humidity measurement at PDH, the *Pelican* distribution was theoretically dried. While some discrepancies are seen to exist between the measurements made, they are thought to be within experimental error and could potentially be explained by the sampling of slightly different air parcels even when in close proximity.

### 4.2.3 Particle Index of Refraction

For accurate evaluation of optical particle measurements, as well as for eventual comparisons with the direct optical measurements made on board the aircraft, knowledge of particle index of refraction is necessary. Subsequent to calculating the wet particle size of a salt particle, and therefore the solute concentration, refractive index can be determined in a straightforward manner through the use of the partial molal refraction approach described by Moelwyn-Hughes (1961). Elemental carbon was assumed to have a constant refractive index of $1.96 - 0.66i$ (Seinfeld and Pandis, 1998),

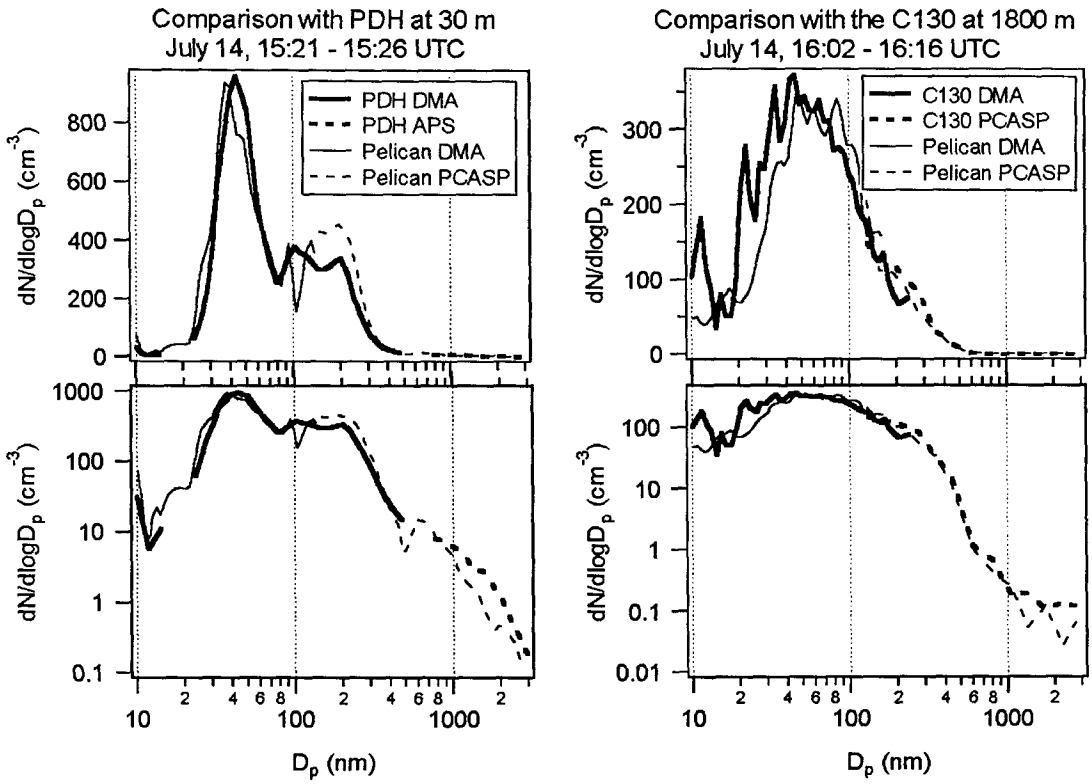


Figure 4.6: Results of size distribution intercomparisons performed with a land site (PDH) and another aircraft (C130) during ACE-2. The distribution measured at PDH incorporated data from both a DMA (R. Van Dingenen, personal communication, 1998) and an Aerodynamic Particle Sizer (E. Swietlicki, personal communication, 1998), while that on the C130 combined data from a DMA (C. O'Dowd, personal communication, 1998) and PCASP (D. Johnson et al., this issue). Pelican size distributions were theoretically dried for comparison with the PDH data, while the measurements made during the C130 intercomparison were of the dried aerosol.

while a value of 1.55 - $0i$ was used for organic carbon (Larson et al., 1988). The index of refraction of dust particles was based on the previous analysis of samples taken on Tenerife by Patterson et al. (1977), which indicated a relatively constant real component of 1.56 along with an imaginary component inversely related to the wavelength of the incident light. An approximate fit of these data over the visible spectrum yields an imaginary component of $0.17\text{x}10^{-0.0025\lambda}$ where $\lambda$ is the incident wavelength in nm. For internal mixtures of elemental and organic carbon with salts, the effective index of refraction was assumed to be the volume-weighted refractive indices of the individual components. Were the particles internally homogeneous, this assumption would be reasonably accurate, but particularly for elemental carbon, this assumption is physically unlikely. However, modeling results by Ackerman and Toon (1981) demonstrate that while the single scatter albedo and scattering phase function of homogeneous and inhomogeneous (modeled as concentric shells) sulfate / elemental carbon particles do differ, for the elemental carbon concentrations observed during ACE-2, these differences are unlikely to result in significant errors.

### 4.2.4 Optical Measurements

While the *Pelican* payload provided measurement of a wide range of aerosol characteristics, because of the goal of achieving radiative closure, the optical parameters of the aerosol were characterized more comprehensively than any other single property. Among the instrumentation used to accomplish this was a 14-wavelength sunphotometer and three nephelometers.

#### NASA Sunphotometer

The 14-wavelength NASA Ames airborne tracking sunphotometer continuously measured the optical depth of the column of air between the aircraft and the top of the atmosphere (Schmid et al., 2000). By subtracting from this value the optical depth due to Rayleigh scattering by gas molecules and absorption by certain gas species, the aerosol optical depth for wavelengths between 380 and 1558 nm was deduced

as a function of altitude. The derivative of a continuous measurement of optical depth made during an ascent or descent produces the altitude-dependent extinction coefficient, $\sigma_{ext}$ ($m^{-1}$),

$$\sigma_{ext} = \frac{d\tau(z)}{dz} \tag{4.2}$$

where $\tau(z)$ is the sunphotometer measured optical depth between the instrument's altitude, $z$, and the top of the atmosphere.

For comparison with the sunphotometer data, aerosol size distributions, adjusted to ambient relative humidity, were used in conjunction with the size-resolved chemical compositions as inputs into Mie theory, from which the extinction coefficient was calculated by summing the integrated extinction coefficients resulting over the range of chemical compositions,

$$\sigma_{ext} = \sum_{i=1}^{k} \int_{Dp1}^{D_{p2}} \frac{\pi}{4} D_p^2 Q_{ext}(D_p, \lambda, m(D_p, i, RH)) n(D_p, i, z) d\log D_p, \tag{4.3}$$

where $i$ represents the particular composition (i.e., $NH_4HSO_4$, NaCl, etc.), $k$ is the number of separate composition types considered, $D_p$ is the particle diameter over which the integral is performed, $D_{p1}$ and $D_{p2}$ are the minimum and maximum diameters measured, respectively, which would ideally be 0 and $\infty$, $Q_{ext}$ is the particle extinction efficiency, $\lambda$ is the wavelength of the incident light, $m(D_p, i, RH)$ is the complex index of refraction of the particle, which is a function of the particle's size, composition, and the ambient relative humidity, $RH$, and $n(D_p, i, z)$ is the size distribution function of species $i$.

While the above calculations were performed for each of the 14 wavelengths measured by the sunphotometer, detailed comparisons were made for three wavelengths (448, 525, and 667 nm) that are not significantly affected by gas phase absorption, and for which assumptions concerning the refractive indices used were most relevant. The optical parameters calculated are obviously sensitive to the accuracy with which the chemical make-up of the aerosol is estimated, and also to the assumptions con-

cerning particle shape, particularly within the mineral dust layers. Sensitivity to particle shape is somewhat reduced because of the fact that, unlike the relatively large discrepancies present between the phase functions of spherical and nonspherical particles, the error in corresponding extinction cross sections is expected to have a maximum of 15%, and a more likely value of about 5%, for the particular dust aerosols sampled (Mishchenko et al., 1997). The potential error resulting from the size distribution extrapolations will be discussed subsequently.

### Nephelometers

Three separate integrating nephelometers were utilized on the *Pelican*; a TSI 3563 3-color nephelometer capable of measuring both total scattering and hemispherical backscattering, and two Radiance Research nephelometers operated at different relative humidities, collectively referred to as a passive humidigraph. The sample stream reaching the TSI nephelometer typically had a relative humidity below 40% within the boundary layer. Detailed results obtained with the TSI and humidigraph nephelometers are described in Öström and Noone (2000) and Gassó et al. (2000), respectively. Located in the nose area of the plane, all three of the instruments sampled from the community inlet downstream of the cyclone. An ideal nephelometer makes use of a Lambertian light source to measure directly the scattering coefficient of an aerosol population, whereas actual nephelometers suffer from non-ideal light sources and an inability to detect light scattered by particles in the near forward or near backward direction.

Comparison of the derived aerosol optical properties with those measured by the nephelometers requires slightly more analysis than did the calculations performed for comparison with the sunphotometer. First of all, only a subset of the full spectrum of particles will reach the nephelometers because of losses within the cyclone. While the cyclone has a nominal 50% cut size of 2.5 $\mu$m diameter for a unit density particle at STP, consideration of the particle density and gas viscosity is necessary to predict accurately which particles are removed. Although the change in cut size may be relatively insignificant for aqueous particles in the boundary layer, for dust particles

that have densities on the order of 2.6 g $cm^{-3}$ (Tegen and Fung, 1994), the cutoff will be reduced by about 40%. Penetration efficiency as a function of particle diameter was then determined using an s-curve relationship appropriate for the cyclone. For those particles that do penetrate the cyclone, theoretical growth / evaporation calculations are used to predict the equilibrium size of the particle at the relative humidities measured within each of the nephelometers. Frequently, the humidity of the gas stream entering the humidigraph is below the crystallization point of certain salt compounds. When this occurs, only if the humidity in the humidified nephelometer is above the deliquescence point for the given salt is an aqueous solution assumed.

Anderson et al. (1996) investigated the non-idealities in the light source as well as the truncation of near forward and near backward scattered light for the TSI 3563 for measurement of both total scattering and hemispherical backscattering. No similar data are available for the Radiance Research nephelometers, so their characteristics were assumed to be equivalent to those of the TSI instrument. The resulting angular sensitivity can be utilized to determine the expected scattering intensity as measured by the nephelometer, $\sigma_{sca,neph}$,

$$\sigma_{sca,neph} = \sum_{i=1}^{k} \int_{Dp1}^{D_{p2}} \eta(D_p, \rho(i, RH), \mu) \frac{\pi}{4} D_p^2 \; Q_{sim}(D_p, \lambda, m(D_p, i, RH), f(\Theta)) n(D_p, i, z) d\log D_p \tag{4.4}$$

where $\eta(D_p, \rho(i, RH), \mu)$ is the penetration efficiency through the cyclone and associated tubing for a particle of a given size and density contained within a gas with viscosity, $\mu$, and $Q_{sim}$ is the expected scattering efficiency for a nephelometer with angular sensitivity, $f(\Theta)$ (Anderson et al., 1996).

## 4.3 Results and Discussion

During the six-week period of intensive sampling associated with ACE-2, the *Pelican* flew 21 missions ranging in duration from just over two hours to more than ten hours. The diverse payload on board the *Pelican* allowed for participation in the coordinated CLEARCOLUMN, CLOUDYCOLUMN, and LAGRANGIAN experiments. The large volume of size distribution data recorded during ACE-2 precludes description of the findings of each of the separate flights. Instead, an attempt is made to categorize the measured aerosols into groups with similar characteristics and, in general, similar origins. An in depth analysis of four of the flights is given here with the goal of evaluating radiative closure.

The first mission flown by the *Pelican* during ACE-2 was on June 18, 1997. It was not until the 12th flight on July 7, however, that an air mass arrived in the area of study that clearly possessed characteristics suggesting significant influences from non-marine sources. Prior to July 7, and occasionally at later dates, back trajectories as calculated by the Royal Netherlands Meteorological Institute (KNMI) using the European Centre for Medium Range Weather Forecasts (ECMWF) model suggested that both the boundary layer and free tropospheric air had spent several days over the North Atlantic. This length of time is generally sufficient to reduce substantially any influence from previous land-based emissions of aerosols or their precursors. Following this initial period, during which only relatively clean air masses were encountered, the calculated back trajectories typically showed air parcels arriving in the local boundary layer had either passed over the Iberian Peninsula, or just adjacent to it. As a result, relatively small changes in the path taken by an air mass arriving in the ACE-2 area could have significant impacts on the properties of the sampled aerosol. At approximately the date the boundary layer trajectories shifted towards Europe, the source region of the free tropospheric aerosols switched from the Atlantic to Northern Africa. On multiple occasions, these air parcels arriving from Africa contained substantial quantities of Saharan dust particles.

### 4.3.1 Overall Aerosol Properties

#### Boundary Layer

**Background Marine** Consistent with previous measurements made during relatively clean conditions in the Northeastern Atlantic, submicrometer number size distributions were found to be bimodal in nature, possessing distinct nuclei and accumulation modes (Jensen et al., 1996; Russell et al., 1996a; Raes et al., 1997). The nuclei mode, which is thought to form as a result of particle nucleation followed by growth due to condensation and coagulation, peaked at around 60 nm. While this peak size was found on occasion to be as low as approximately 30 nm, no appreciable concentration of even smaller particles representative of recent nucleation events were observed within the boundary layer. Although the absence of recently formed particles in the marine boundary layer is not unusual for this region, the limited counting statistics associated with detecting these particles with a rapidly scanning DMA may result in an inability to accurately measure relatively small concentrations of these ultrafine aerosols. Subsequent processing of the particles within the nuclei mode, particularly within clouds (Hoppel et al., 1986), serves to form the accumulation mode. While the majority of particles were smaller than 1 $\mu$m, most of the aerosol mass within the clean boundary layer always resided in particles $> 1$ $\mu$m that are presumably composed of sea salt.

Mie theory calculations were performed using the recovered size distributions and assumed compositions to evaluate the relative importance of the fine and coarse mode fractions to the optical properties of the aerosol. Although there is nothing intrinsically special about the 1 $\mu$m division, it does offer, roughly, a distinction between the sulfates and carbon particles that are thought to be largely present in the fine mode, and the sea salt, and possibly dust particles, composing most of the coarse mode. On average, for these clean boundary layer aerosols, the submicron and supermicron particles were found to contribute approximately equally both to the total aerosol extinction coefficient and to the total aerosol hemispherical backscattering coefficient, a quantity slightly more indicative of the radiative forcing resulting from an aerosol

population.

While the bimodal number distribution and supermicron mass mode were present in all of the distributions measured, large variations existed in the properties of each of these modes as well as in the distribution as a whole. This is clearly shown in Table 4.1, which presents the mean and range of a number of key parameters describing the clean boundary layer as well as the other aerosol types described in more detail below. Since the primary focus of this paper is radiative closure using in situ measurements, the particle size distribution either measured at, or theoretically adjusted to, ambient relative humidity is most relevant. Each of the quantities listed in Table 4.1 was, therefore, calculated with respect to the ambient distributions.

**Polluted Boundary Layer** During periods for which the air masses arriving in the boundary layer crossed sections of Western Europe, total number concentrations increased to over 1000 $cm^{-3}$, and for the most polluted case, exceeded 4000 $cm^{-3}$. In addition to the enhanced number concentrations of these continentally influenced aerosols, the intensive properties of the associated size distributions changed as well. The most obvious difference in the number distribution associated with the polluted aerosols relative to those measured during background conditions is the lessening importance of the nuclei mode relative to the accumulation mode. Of the four flights during which these enhanced number concentrations were measured, the size distributions corresponding to the three most polluted cases showed little or no nuclei mode. The aerosol measured during the remaining case did have a discrete nuclei mode, although the trough separating it from the accumulation mode was significantly more shallow than observed during the relatively clean cases. Evidence of this shift towards monomodality with increasing continental influence has been observed in the North Atlantic by others (Jensen et al., 1996; Russell et al., 1996). This results from an increase in the aerosol surface area available in the accumulation mode that acts as a sink for condensable species that might otherwise form new particles or add to nuclei mode particles. Although a slight majority of the volume (at ambient

Table 4.1: Average and range of parameters describing the aerosol types sampled during ACE-2. Properties described are the aerosol number concentration, $N_{total}$, the number median diameter, $D_p^{num}$, the surface area median diameter, $D_p^{SA}$, the volume median diameter, $D_p^{vol}$, the diameter corresponding to the peak in the nuclei mode, $D_p^{nuc}$, the diameter corresponding to the peak in the accumulation mode, $D_p^{acc}$, the diameter corresponding to the minimum between the nuclei and accumulation modes, $D_p^{\min}$, the ratio of the number of particles in the nuclei mode to the number in the accumulation mode, $\frac{N_{nuc}}{N_{acc}}$, the ratio of the extinction resulting from the submicron aerosol fraction to that resulting from the supermicron aerosols, $\frac{\sigma_{ext}(<1\mu m)}{\sigma_{ext}(>1\mu m)}$, and the similar ratio for hemispherical backscattering, $\frac{\sigma_{bsca}(<1\mu m)}{\sigma_{bsca}(>1\mu m)}$. Each of the quantities corresponds to size distributions either measured at, or adjusted to, ambient relative humidity. Cl. = Clean, Po. = Polluted.

| | Cl. BL | Pol. BL | Cl. FT | Pol. FT | Dust FT |
|---|---|---|---|---|---|
| *# Cases* | 10 | 4 | 8 | 1 | 3 |
| $N_{total}$ $(cm^{-3})$ | 492 (288–720) | 2350 (1050–4110) | 363 (240–434) | 692 | 281 (272–290) |
| $D_p^{num}$ $(nm)$ | 123 (32–224) | 170 (142–193) | 63 (50–73) | 91 | 83 (78–89) |
| $D_p^{SA}$ $(nm)$ | 818 (307–1950) | 392 (342–441) | 136 (113–158) | 147 | 2310 (2030–2600) |
| $D_p^{VOL}$ $(nm)$ | 3670 (2200–4700) | 2890 (2000–3940) | 1740 (890–2950) | 895 | 4300 (3860–4740) |
| $D_p^{nuc}$ $(nm)$ | 58 (27–80) | 101 (89–112) | 64 (34–95) | 112 | 98 (89–106) |
| $D_p^{acc}$ $(nm)$ | 237 (225–252) | 243 (178–317) | *NA* | *NA* | *NA* |
| $D_p^{\min}$ $(nm)$ | 130 (89–159) | 184 (178–189) | *NA* | *NA* | *NA* |
| $\frac{N_{nuc}}{N_{acc}}$ | 1.85 (0.55–5.24) | 1.51 (1.27–1.75) | *NA* | *NA* | *NA* |
| $\frac{\sigma_{ext}(<1\mu m)}{\sigma_{ext}(>1\mu m)}$ | 0.92 (0.16–2.18) | 2.19 (1.32–3.54) | 1.85 (0.85–2.75) | 5.32 | 0.14 (0.11–0.16) |
| $\frac{\sigma_{bsca}(<1\mu m)}{\sigma_{bsca}(>1\mu m)}$ | 0.98 (0.22–2.27) | 2.00 (1.37–2.91) | 3.88 (1.92–5.66) | 14.4 | 0.22 (0.15–0.29) |

RH) still resides in the supermicron aerosol fraction, the submicron fraction was found to contribute an average of about twice as much to both the extinction and backscattering coefficients.

### Free Troposphere

The distinction between free tropospheric aerosols that contained significant quantities of mineral dust and those that did not was relatively sharp. During three flights in particular, when mineral dust was present aloft, the coarse mode aerosol mass exceeded 10 $\mu$g m$^{-3}$, while values of less than 1 $\mu$g m$^{-3}$ characterized the non-dusty flights. However, this categorical distinction does not preclude the presence of sufficient dust particles to dominate the total mass of the "non-dusty" aerosol, but rather serves as a simple division between those cases where dust was likely to play a significant role in the total columnar optical depth, and those where it was not.

**Free Troposphere without Mineral Dust** Back trajectories corresponding to most of the non-dusty cases remained over the North Atlantic for several days, although in two instances they passed over sections of Africa. From previous measurements made at IZO, Raes et al. (1997) observed that the aerosol number distribution within the free troposphere during clean conditions consisted of a single, nuclei sized mode with an integrated number concentration of approximately 425 cm$^{-3}$ at STP. Size distributions measured on board the *Pelican* during ACE-2 support these findings. The location of this single mode varied little over the measurement period, although the total number concentration changed by almost a factor of two. No clear indication of high concentrations of freshly nucleated particles was observed during any of the flights. A maximum altitude of 3.9 km was achievable by the *Pelican*, so nucleation occurring at even higher altitudes was still a possibility. Aerosol properties measured during the June 21 flight were sufficiently different from the remaining cases that they are presented separately in Table 4.1. The increased number concentration and median diameter measured during this flight suggest atypical sources or processing of some kind, although the calculated back trajectories suggest

that the origin of this air mass was a region of the North Atlantic similar to most of the other clean cases. Similar to the polluted boundary layer, both extinction and backscattering were dominated by submicron particles. However, relative to both the volume and extinction associated with the aerosol within the boundary layer, the contribution from the clean free tropospheric aerosol is almost negligible.

**Free Troposphere with Mineral Dust** The free troposphere number distributions for Saharan dust laden aerosols were, in fact, very similar to those corresponding to clean conditions, possessing a single mode consisting of several hundred particles $cm^{-3}$. Only when aerosol volume or extinction is plotted relative to particle size is the presence of the larger dust particles apparent. As will be discussed in the section describing the case studies, these relatively few particles resulted in extinction coefficients of the same magnitude as those resulting from continentally influenced, boundary layer aerosols. Although the total aerosol mass in these cases is subject to error due to the extrapolations used, the majority of the associated extinction is seen to result from particles within the PCASP range (at least when the range is adjusted to account for index of refraction). One of the most interesting features of the observed dust layers was the gradient in concentration encountered as a function of altitude. The extinction resulting from mineral dust in the free troposphere was observed to increase by as much as two orders of magnitude over as little as a kilometer in altitude change. The sampling site at IZO was located within this gradient, and therefore, slight shifts in the height of the dust layer could have pronounced impacts on the measurements made there. Even larger error could be incurred if lower elevation, ground-based, measurements were used as a basis to estimate the columnar optical properties.

### 4.3.2 Phase Functions

To offer further insight into the optical characteristics of each of the aerosol types discussed above, as well as to provide potential inputs for remote sensing algorithms, scattering phase functions were calculated. Average phase functions were calculated

for the free tropospheric and boundary layer aerosol measured during each flight. The mean and standard deviation of the phase functions associated with each of the described aerosol types were then calculated using the appropriate set of flight-average values. The results of these calculations are shown in Figure 4.7. The mean and standard deviation were calculated using the logarithm of the flight-average values since the absolute values typically span several orders of magnitude. Additionally, the theoretical results of Mishchenko et al. (1997) were used to predict the phase functions associated with nonspherical dust particles. There is clearly more variation in the phase functions resulting from measurements made within the clean marine boundary layer than from the polluted cases, although this may, in part, be a result of a more limited sample for the polluted aerosols. The relatively shallow phase function calculated for the non-dusty free troposphere is a result of both the high concentration of small particles and the enhanced absorption by these particles due to the higher elemental carbon content assumed (based on measurements). As previously discussed, these particles have little impact on the columnar radiative properties of the aerosol. For the other, optically more important, aerosol types, variability within the categories is seen to be comparable to the variability between the categories, indicating that errors resulting from assuming a constant phase function for a given type of aerosol may be similar in magnitude to assuming an incorrect aerosol type all together.

## 4.4 Case Studies

While assessment of radiative closure is possible using any type of flight pattern, vertical spirals in a cloudless area are particularly useful in that they allow for a continuous profile of sunphotometer-derived extinction coefficients from near sea-level to well into the free troposphere. During ACE-2, vertical spirals were flown on 8 of the 21 Pelican missions, although clouds were present during one of these spirals, compromising the sunphotometer data. Of the seven remaining flights, four were conducted early in the campaign when clean conditions prevailed. Since the focus of

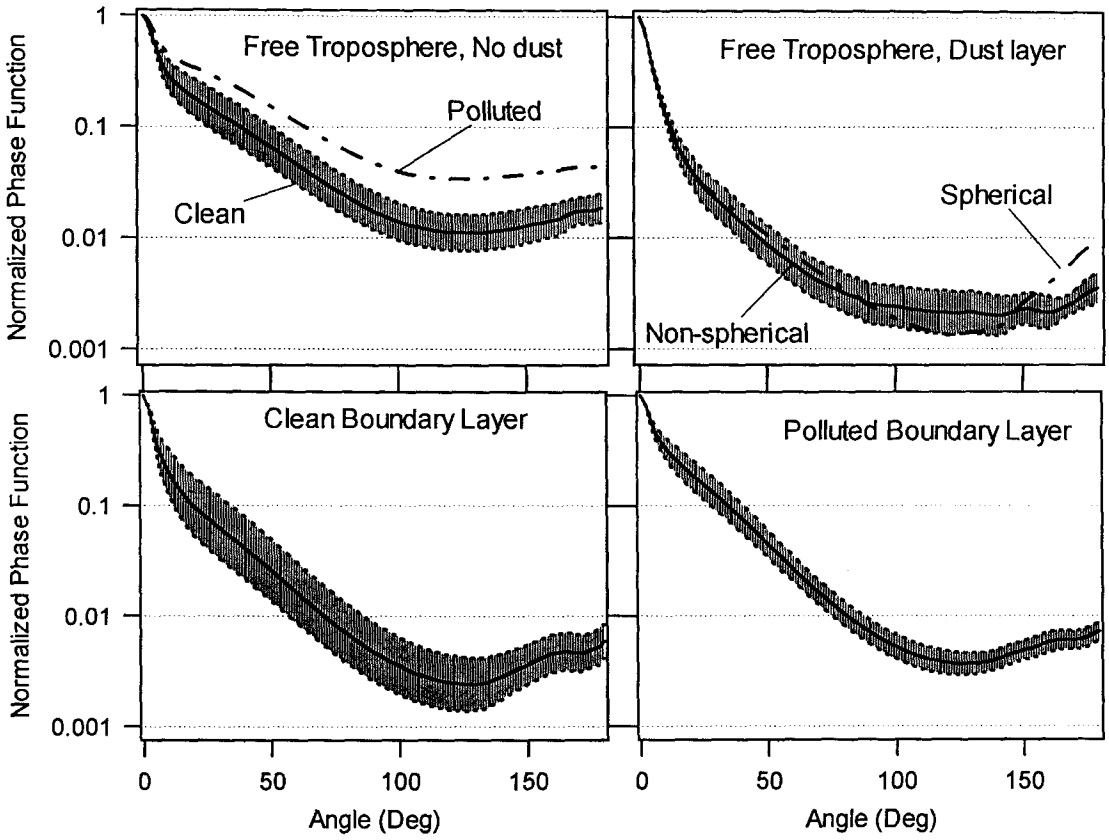


Figure 4.7: Averaged phase functions corresponding to each of the aerosol types characteristic of the ACE-2 region. The solid line represents the mean value of the phase functions measured during flights associated with the particular aerosol type, while the shaded area corresponds to +/- one standard deviation. Phase functions calculated for the dust aerosols were adjusted to account for the fact that the particles are likely not spheres through the use of modeling results by Mishchenko et al. (1997). All size distributions were adjusted to ambient relative humidity.

this campaign was to characterize Saharan dust and European pollution aerosols, only one of these background flights was chosen, along with each of the non-background cases, for detailed analysis. The primary focus here is a discussion of the comparisons between the derived and measured optical parameters. More detailed analyses of the radiative impact of the aerosols studied is available elsewhere (Schmid et al., 2000; Öström and Noone, 2000; Gassó et al., 2000).

**Uncertainty Analysis** In an attempt to quantify the effect uncertainties in the measurements made and assumptions used have on radiative closure, a number of sources of error were considered for each of the four case studies. This procedure was performed for each of the wavelengths measured by the sunphotometer, and for each of the nephelometers utilized. The individual sources of error considered were uncertainty concerning the degree to which the aerosol was heated in the PCASP; errors in the measurement of the ambient relative humidity as well as that within each of the nephelometers; error in the concentrations used for the size distribution extrapolation when no FSSP data were available; incorrect sizing by the DMA and OPCs; incorrect assumptions about the fraction of the aerosol assumed to be non-hygroscopic (i.e., EC, OC, and dust); incorrect assumptions concerning the mixing state of the aerosol; error related to the assumption that salt aerosols were hydrated when the RH was above the appropriate crystallization point; error resulting from the assumption that organic carbon aerosol is non-hygroscopic; and uncertainty regarding the penetration efficiency of the cyclone. Additionally, random errors associated with each of the instruments were considered.

The resulting combined uncertainties are presented for each comparison as a function of altitude in the difference plots that are described below in the discussion of the individual case studies. A subset of these data are summarized in Tables 4.2 and 4.3. Many of the uncertainties are highly variable among flights and as a function of altitude, so the averaged values presented in the tables provide only a degree of insight into the relative importance of each of the potential sources of error. Several of the responses to the specified perturbations seem counter-intuitive at first. These

peculiarities result from the abrupt change in particle size associated with either the crystallization or deliquescence point for the salts considered. For instance, an increase in the ambient relative humidity in the free troposphere is seen to result in a decrease in the calculated extinction coefficient. In this case, the drying associated with the PCASP was originally sufficient to reduce the relative humidity below the crystallization point of at least one of the salts assumed to be present. The calculated size of the particles at ambient RH is therefore much larger than for the case in which a higher ambient humidity prevents crystallization of the particles within the PCASP. A description of the relative importance of each of the sources of error for each of the instruments under the range of conditions encountered would be prohibitively long. However, it is clear from these results that sizing accuracy, mixing state, degree of heating within the PCASP, and assumptions concerning the hygroscopicity of organics are among the most important sources of error in many of the cases analyzed. Relative to these uncertainties, ultimate determination of scattering or extinction from the size distribution measurements is not particularly sensitive to the extrapolation used in the absence of FSSP data. Random errors associated with each of the measurements often exceeded the uncertainty attributable to the other perturbations, although an average value of these estimates is of little use given the variability in the aerosol loading observed even for a given class of conditions.

**June 21, 1997** KNMI back trajectories terminating at Tenerife on June 21, show that both the boundary layer and free tropospheric air masses had remained over the North Atlantic for several days. This mission was, therefore, aimed at analyzing the relatively unperturbed aerosol characteristic of this region, which can then serve as a baseline to which the more anthropogenically or desert influenced aerosols can be compared. To avoid potential island influence, the flight was conducted to the northwest of Tenerife, as is shown on Figure 4.8. As discussed previously, chemical composition measurements made on Tenerife both in the boundary layer and the free troposphere were used to construct size-resolved aerosol compositions. The assumed compositions shown in Figure 4.8 are representative of these relatively clean condi-

Table 4.2: Uncertainties related to radiative closure with the sunphotometer. Each quantity represents the average response to the specified perturbation for the four case studies discussed. To estimate the potential error resulting from the assumption that the organics particles were non-hygroscopic, they were assumed to have growth characteristics identical to ammonium bisulfate. Scatter in the optical depths measured by the sunphotometer was used to estimate the random error associated with the derived extinction coefficients for each flight. The uncertainty related to the FSSP extrapolation is only relevant for those flights in which the FSSP was inoperable.

| Perturbation | | Boundary Layer | |
|---|---|---|---|
| Type | Magnitude | Clean | Polluted |
| PCASP heating | +/- 2 °C | +17.1 / -6.2% | +19.8 / - 9.0% |
| RH measurement | +/- 3% | +2.8 / -4.1% | +6.5 / -7.2% |
| FSSP extrapolation | +/- 50% | +4.6 / -3.1% | +3.1 / -2.0% |
| Sizing accuracy | +/- 5% | +18.4 / -14.5% | +20.8 / -16.0% |
| Carbon, dust fraction | +/- 50% | -4.3 / +3.6% | -1.8 / +2.9 % |
| Mixing state | external / internal | +0.8 / -3.8% | -4.8 / -0.5% |
| Deliquescence | If $RH_{amb} > RH_{del}$ | -1.6% | -2.9% |
| Organic hygroscopicity | $\sim NH_4HSO_4$ | +14.6% | +2.8% |
| Size distribution random error | +/- $\sqrt{N}$ | +/- 14.8% | +/- 11.5% |
| Sunphotometer random error | est. from scatter | +/- 6.7% | +/- 6.2% |

| Perturbation | | Free Troposphere | |
|---|---|---|---|
| Type | Magnitude | No Dust | Dust |
| PCASP heating | +/- 2 °C | +0.6 / -0.3% | +0.3 / -0.3% |
| RH measurement | +/- 3% | -0.4 / -3.5% | +0.0 / -0.4% |
| FSSP extrapolation | +/- 50% | +2.1 / -1.4% | +12.7 / -8.5% |
| Sizing accuracy | +/- 5% | +18.8 / -15.0% | +11.3 / -9.9% |
| Carbon, dust fraction | +/- 50% | +3.7 / -5.8% | +0.2 / -1.2% |
| Mixing state | external / internal | +10.2 / 3.9% | -5.6 / -1.9% |
| Deliquescence | If $RH_{amb} > RH_{del}$ | +4.3% | -3.0% |
| Organic hygroscopicity | $\sim NH_4HSO_4$ | +14.3% | +13.0% |
| Size distribution random error | +/- $\sqrt{N}$ | +/- 23.8% | +/- 22.9% |
| Sunphotometer random error | est. from scatter | +/- 27.7% | +/- 3.6% |

Table 4.3: Uncertainties related to radiative closure with the non-humidified nephelometerr. Each quantity represents the average response to the specified perturbation for the four case studies discussed. To estimate the potential error resulting from the assumption that the organics particles were non-hygroscopic, they were assumed to have growth characteristics identical to ammonium bisulfate. Estimation of the random error in the humidigraph and TSI nephelometer measurements was accomplished by adjusting the values specified by Gassó et al. (this issue) and Anderson et al. (1996) to the ~90 s sampling interval employed here. The uncertainty related to the FSSP extrapolation is only relevant for those flights in which the FSSP was inoperable.

| Perturbation | | Boundary Layer | |
|---|---|---|---|
| Type | Magnitude | Clean | Polluted |
| PCASP heating | +/- 2°C | +12.3 / -6.8% | +12.2 / -8.0% |
| RH measurement | +/- 3% | +3.7 / -0.1% | -0.3 / -3.3% |
| FSSP extrapolation | +/- 50% | +0.2 / -0.1% | +0.1 / -0.1% |
| Sizing accuracy | +/- 5% | +17.7 / -14.4% | +18.8 / -15.4% |
| Carbon, dust fraction | +/- 50% | -6.6 / +8.1% | -4.5 / +2.8% |
| Mixing state | external / internal | +24.2 / -17.1% | +4.7 / -2.0% |
| Deliquescence | If $RH_{amb} > RH_{del}$ | +6.3% | +0.4% |
| Organic hygroscopicity | $\sim NH_4HSO_4$ | +17.7% | +5.1% |
| Cyclone cutoff | +/- 15% | +2.3 / -5.1% | +0.3 / -5.4% |
| Size distribution random error | +/- $\sqrt{N}$ | +/- 8.9% | +/- 5.3% |
| Nephelometer random error | $6.5 \cdot 10^{-7}$ $m^{-1}$ | +/- 8.2% | +/- 1.4% |

| Perturbation | | Free Troposphere | |
|---|---|---|---|
| Type | Magnitude | No Dust | Dust |
| PCASP heating | +/- 2 °C | +0.6 / -0.5% | +0.6 / -0.5% |
| RH measurement | +/- 3% | +5.8 / -4.3% | -0.5 / -1.2% |
| FSSP extrapolation | +/- 50% | +0.0 / -0.0% | +0.2 / 0.2% |
| Sizing accuracy | +/- 5% | +20.0 / -16.1% | +8.8 / -7.6% |
| Carbon, dust fraction | +/- 50% | -2.8 / +0.5% | -2.6 / +2.5% |
| Mixing state | external / internal | +16.6 / -16.7% | +10.3 / -17.4% |
| Deliquescence | If $RH_{amb} > RH_{del}$ | +13.5% | +5.4% |
| Organic hygroscopicity | $\sim NH_4HSO_4$ | +16.5% | -0.2% |
| Cyclone cutoff | +/- 15% | +1.6 / -2.2% | +8.5 / -9.9% |
| Size distribution random error | +/- $\sqrt{N}$ | +/- 18.4% | +/- 14.7% |
| Nephelometer random error | $6.5 \cdot 10^{-7}$ $m^{-1}$ | +/- 61.3% | +/- 6.9% |

tions. In particular, the submicron aerosol is composed of a significant fraction of organic carbon, both in the boundary layer and the free troposphere, while elemental carbon constitutes an appreciable fraction only in the free tropospheric aerosol.

Also shown in Figure 4.8 are the relative humidity, pressure altitude, number size distribution, integrated number concentration, and calculated aerosol mass, all as functions of time. Similar to the majority of the measurements made during ACE-2, the size distribution and associated number concentration vary little with time, in both the boundary layer and free troposphere. As was the case for the overall results discussed above, each of the quantities presented, except aerosol mass, is calculated using the adjusted size distributions at ambient relative humidity. As described previously, the free tropospheric aerosol sampled on this date had a significantly higher number concentration and median diameter than that measured during any of the other flights. This increased concentration does not, however, translate into a significant increase in mass. The sparse, but large, sea salt particles within the boundary layer account for an order of magnitude more mass and extinction than the concentrated, but small, particles within the free troposphere.

Indicated on the plot showing altitude and relative humidity are periods over which the size distributions are averaged. The number, volume, and extinction distributions corresponding to the averaged periods within the free troposphere (FT) and the boundary layer (BL) are shown Figure 4.9. The characteristic bimodal boundary layer number distribution and monomodal free tropospheric number distribution are clearly shown. Also indicated on the altitude and humidity plot is the altitude profile (P) used for radiative closure comparisons. For the closure comparisons, the size distributions were averaged over 90 s to improve upon the resulting counting statistics. This resulted in a vertical resolution of approximately 175 m for 30 min profiles (June 21), 117 m for 45 min profiles (July 8 and July 17), and 88 m for 60 min profiles (July 10).

As shown on Figure 4.9, the column-integrated extinction coefficients calculated using the size distributions were comparable to those derived using the sunphotometer data. However, relatively large discrepancies exist in the boundary layer where

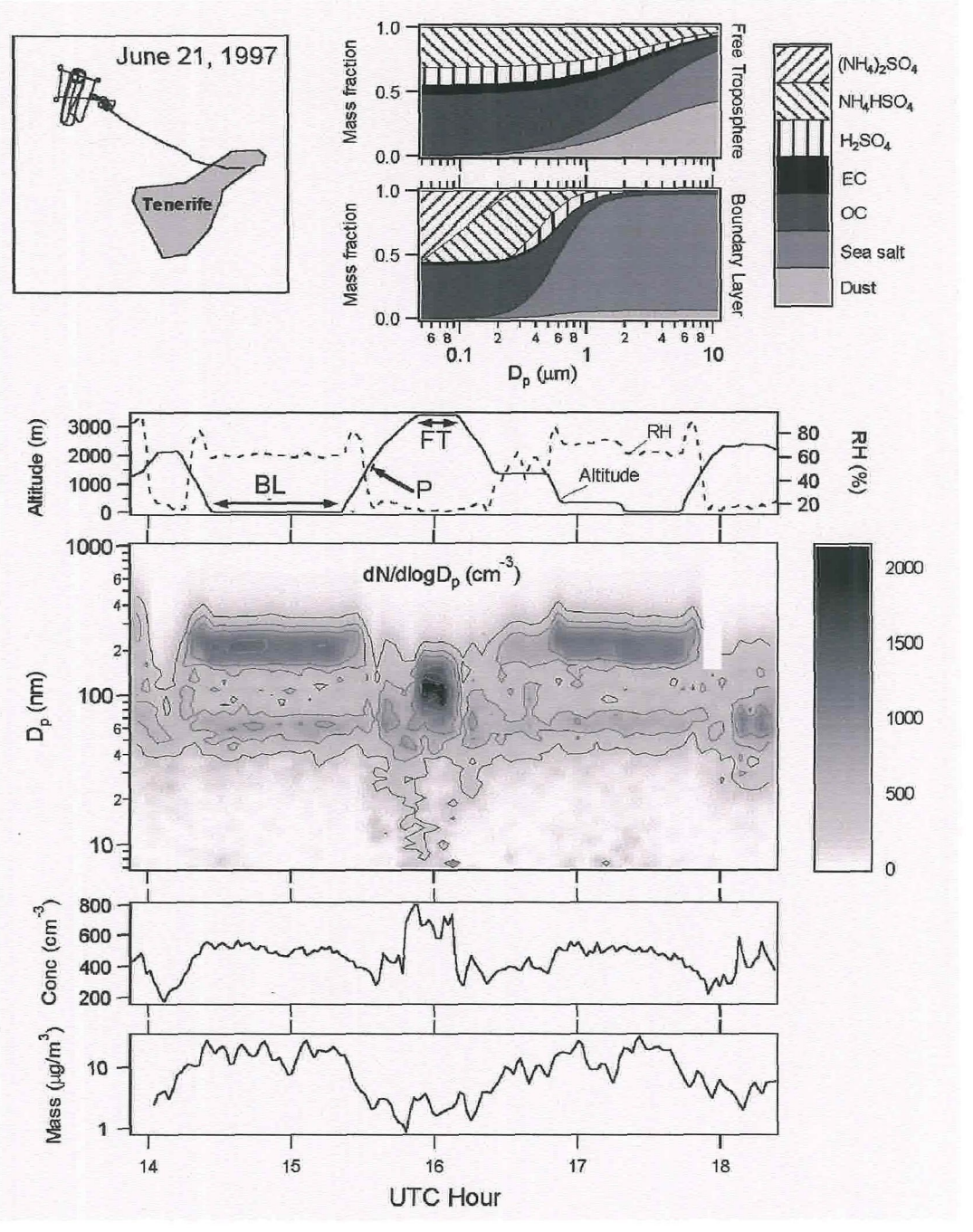


Figure 4.8: Size distributions and derived properties from the June 21 flight. Shown are the assumed chemical compositions, the flight track, the relative humidity and pressure during the flight with averaging periods indicated (BL = boundary layer, FT = free troposphere, and P = altitude profile), an image plot showing the relative change in size distribution as a function of time, and the integrated number concentration and dry aerosol mass as functions of time.

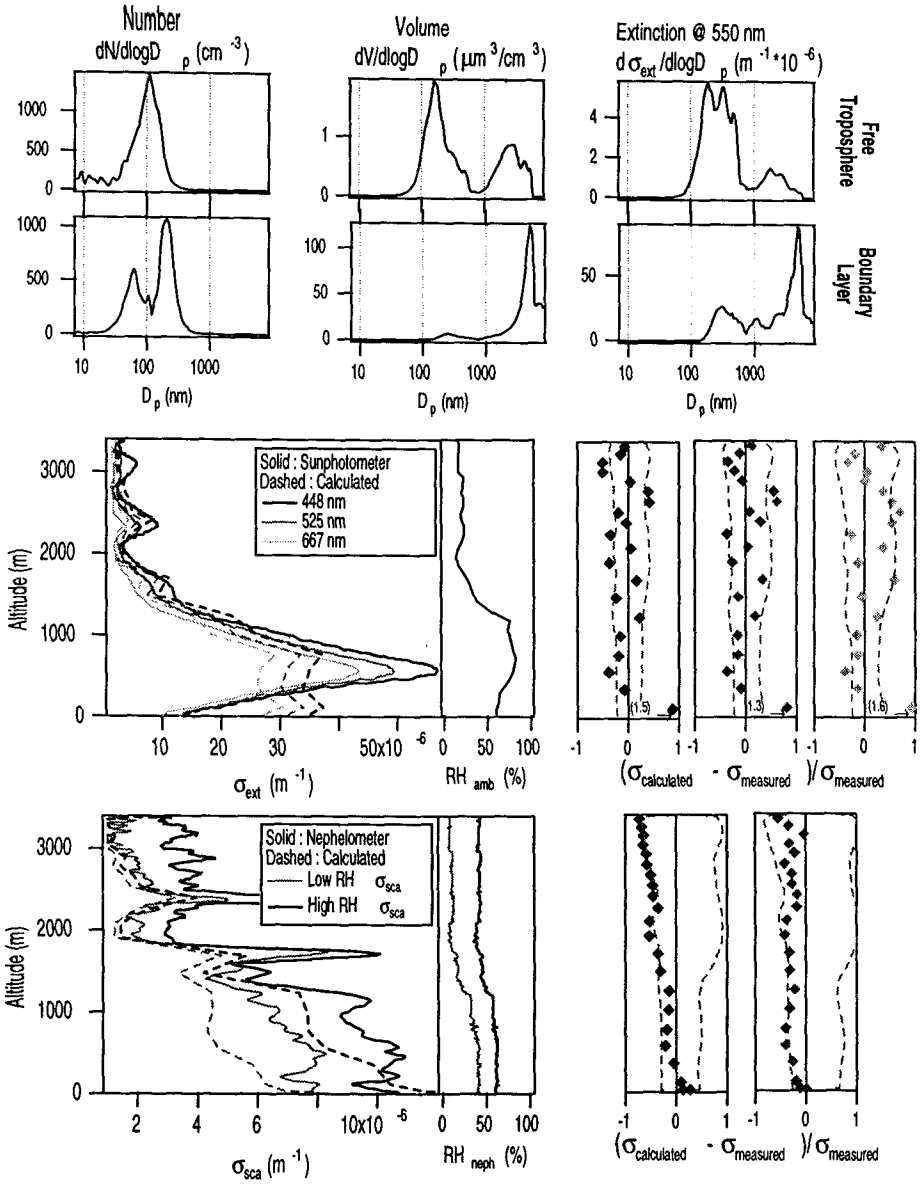


Figure 4.9: Size distributions and optical comparisons from the June 21 flight. Shown are the number, volume, and extinction distributions for the averaging periods shown on Figure 4.8, the comparison between the calculated and measured extinction coefficients corresponding to three of the sunphotometer wavelengths, and the comparison between the calculated and measured scattering coefficients for the nephelometers. Associated with each of the comparisons is a difference plot that presents the fractional discrepancy between the calculated and measured property (diamonds) along with the uncertainty bounds (dashed lines) calculated from the perturbations listed in Tables 4.2 and 4.3. To provide greater detail for the majority of the data points, fractional discrepancies greater than 1 are presented as arrows, with the actual discrepancy shown in parentheses.

the calculations do not capture a distinct maximum present in the sunphotometer data at approximately 500 m. From the adjacent difference plots, it is clear that this disagreement exceeds that expected for the uncertainties and random errors involved in the measurements for about half of the points of comparison within the boundary layer. Although it is not possible to definitively state which measurement is erroneous, a maximum such as that present in the sunphotometer data could be the result of inaccuracies involved in differentiating the raw signal. This postulation is supported by the absence of a similar maximum in the nephelometer data, although the limited particle size range that successfully penetrates the cyclone could hide such a maximum were it a result of large sea salt particles. Additionally, the apparent agreement between the scattering coefficient of the nephelometer operated at near ambient RH and the extinction coefficient derived by the sunphotometer data near sea level suggests that at least one of the measurements is incorrect, since the nephelometer only measures a subset of the total extinction. The size distribution based calculations do appear to capture the measured inverse relationship between extinction and wavelength, a relationship often parameterized as an Ångström coefficient.

Although the maximum discrepancies between the calculated and measured scattering coefficients corresponding to the "wet" and "dry" nephelometers are less than those associated with the sunphotometer comparison, there appears to be a systematic underestimation of the measured values. This is clearly shown in the difference plots associated with the nephelometer comparisons, although most of these points still lie within the range of estimated uncertainties. The calculated increase in the scattering coefficient with increasing relative humidity agrees well with measurements made in the boundary layer, but underestimates those made in the free troposphere. This is most likely the result of inaccurate assumptions concerning the chemical composition of the aerosols or to error incurred by assuming that the organic carbon is non-hygroscopic.

**July 8, 1997** In contrast to the relatively unperturbed boundary layer and free troposphere observed during the June 21 case study, on July 8 the boundary layer air

parcel had passed over much of the Iberian Peninsula while the free tropospheric air parcel originated over Africa. Consistent with expectations, the resulting boundary layer and free tropospheric aerosols contained substantial quantities of anthropogenic aerosols and Saharan dust, respectively. As shown in Figure 4.10, the flight was conducted southeast of Tenerife in a cloudless region that was not directly affected by either Tenerife or the adjacent island, Gran Canaria. Measurements made at PDH show an enhanced fractional contribution of the sulfates in continentally influenced aerosols, which is reflected in the size-resolved, assumed composition for the boundary layer. The fine mode aerosol within the free troposphere was predominantly organic carbon, with dust constituting the majority of the coarse mode.

Boundary layer aerosol number concentrations were observed to reach values more than five times higher than those measured during the cleaner, June 21 flight, while free tropospheric aerosol mass loadings were more than two orders of magnitude greater than those previously measured. The averaged number, volume, and extinction distributions in Figure 4.11 show the monomodal submicron aerosol within the boundary layer dominates the overall extinction coefficient, while the coarse dust particles are responsible for essentially all of the extinction in the free troposphere. The calculated aerosol mass, and to a lesser extent, the calculated extinction coefficient, is sensitive to the extrapolation used since the FSSP on the *Pelican* was inoperable.

Agreement between calculated and measured optical properties of the aerosol for this flight is significantly better than for the June 21 case. Discrepancies associated with the sunphotometer comparisons are within experimental uncertainties both in the boundary layer and the dust layer aloft. Only between these two distinct layers is the disagreement excessive, largely due to the differentiation of sunphotometer data, which resulted in negative extinction coefficients between approximately 1600 and 1900 m. Agreement between the derived and measured scattering coefficients is within specified uncertainties both in the boundary layer, and in the transition between the boundary layer and dust aloft, although a significant amount of scatter is present when the values approach $10^{-6}$ $m^{-1}$. More significant discrepancies exist between the nephelometer measurements and size distribution calculations in the dust

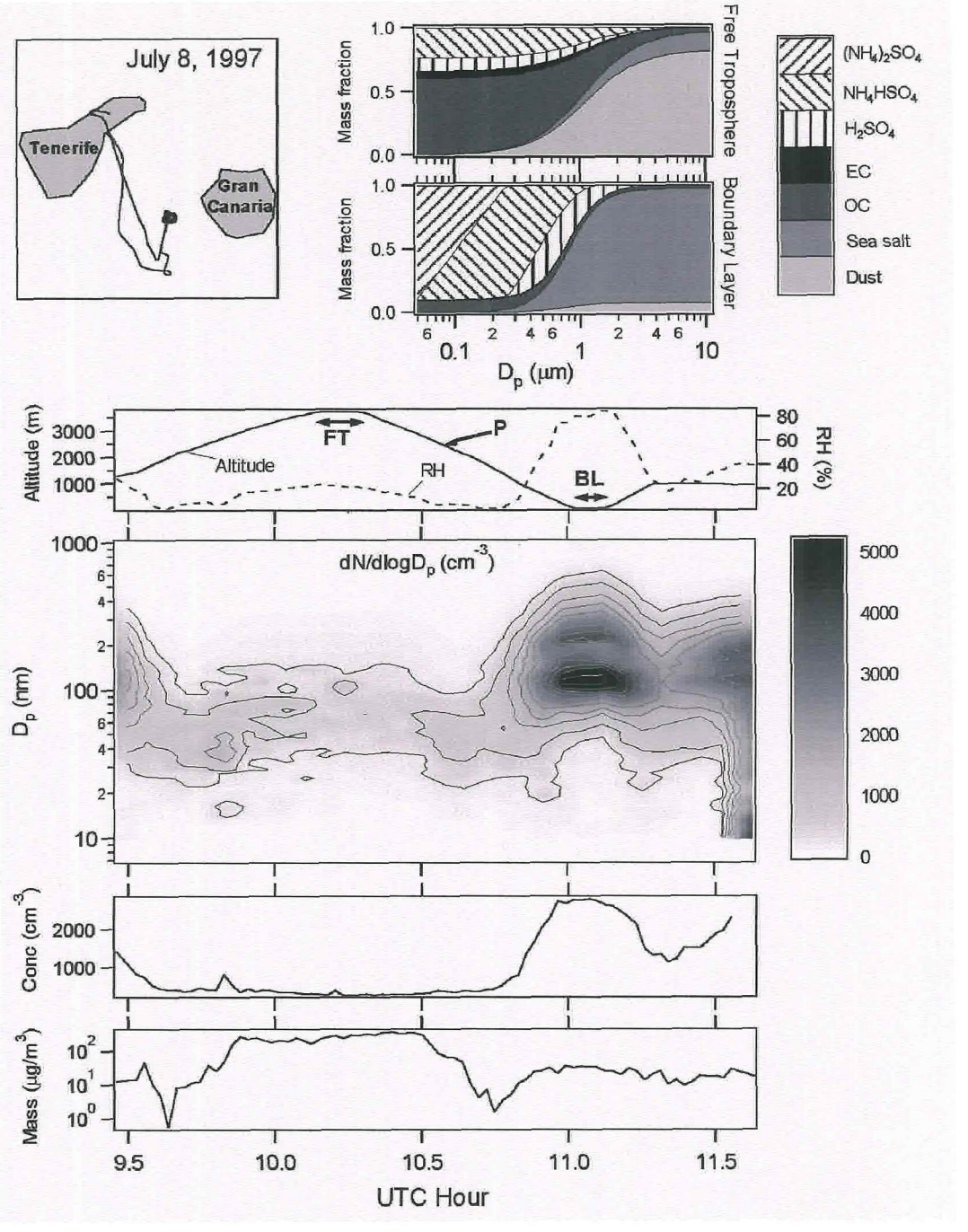


Figure 4.10: Size distributions and derived properties from the July 8 flight. Shown are the assumed chemical compositions, the flight track, the relative humidity and pressure during the flight with averaging periods indicated (BL = boundary layer, FT = free troposphere, and P = altitude profile), an image plot showing the relative change in size distribution as a function of time, and the integrated number concentration and dry aerosol mass as functions of time.

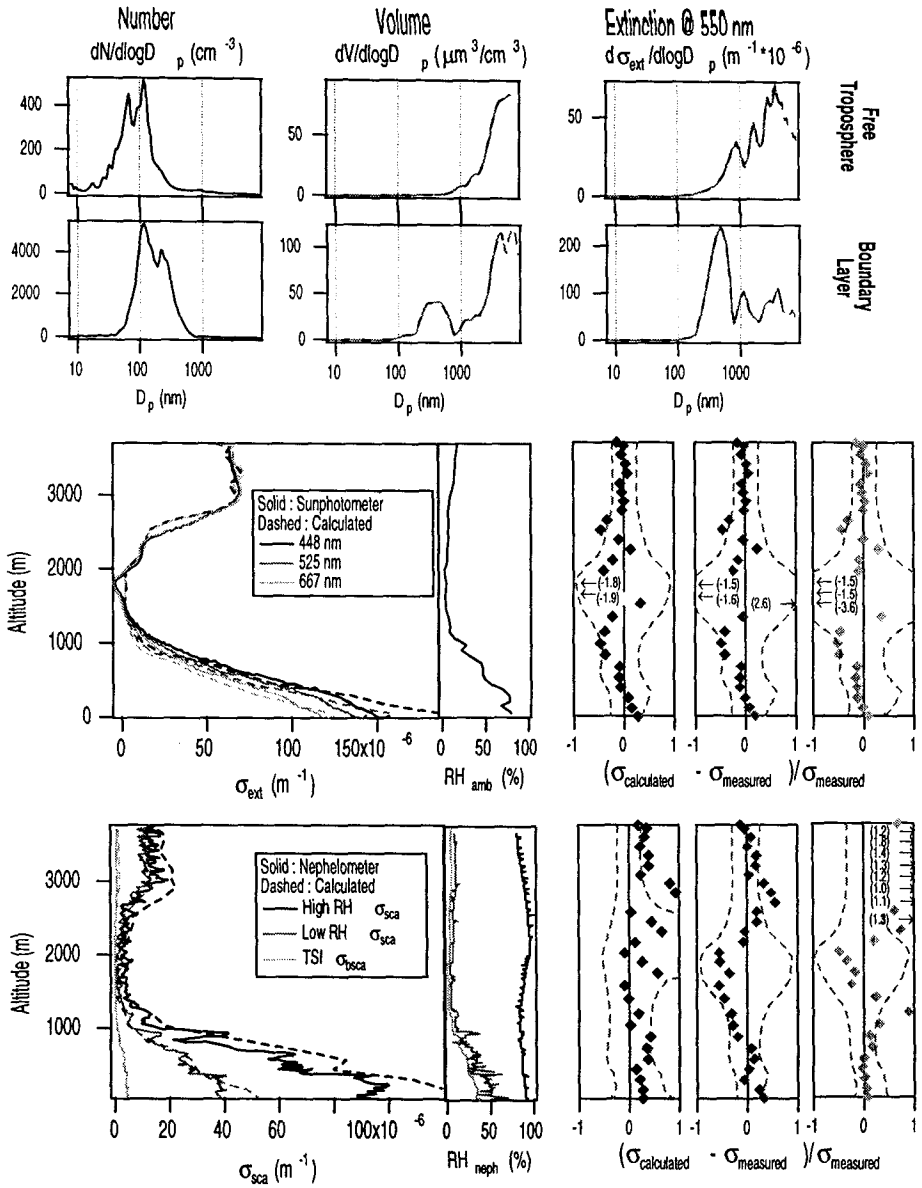


Figure 4.11: Size distributions and optical comparisons from the July 8 flight. Shown are the number, volume, and extinction distributions for the averaging periods shown on Figure 4.10, the comparison between the calculated and measured extinction coefficients corresponding to three of the sunphotometer wavelengths, and the comparison between the calculated and measured scattering coefficients for the nephelometers. Associated with each of the comparisons is a difference plot that presents the fractional discrepancy between the calculated and measured property (diamonds) along with the uncertainty bounds (dashed lines) calculated from the perturbations listed in Tables 4.2 and 4.3. To provide greater detail for the majority of the data points, fractional discrepancies greater than 1 are presented as arrows, with the actual discrepancy shown in parentheses.

layer. Greater than expected losses within the cyclone, tubing, and nephelometers themselves could account for these discrepancies, although a 15% decrease in the cyclone cut size was found to be insufficient to result in agreement. Uncertainty concerning the phase functions of nonspherical particles and the impact this would have on the integrated scattering coefficient and, more importantly, the backscattering coefficient could also lead to the observed disagreement.

**July 10, 1997** The principal focus of the July 10 flight was a sunphotometer intercomparison with the R/V *Vodyanitsky.* As a result, the majority of the flight was a transect to and from the location of the ship, as is shown in the flight track on Figure 4.12. Similar to the July 8 case study, the boundary layer aerosol encountered on July 10 was also continentally influenced. Composition measurements made at PDH on this day indicate that the bulk aerosol had characteristics very similar to those observed for the previous case study, with sulfates dominating the submicron mass. However, the number concentration observed was significantly less than on July 8, while the size distribution was shifted to slightly larger diameters. These two effects were found to partially offset one another with respect to the optical properties of the aerosol, though. The free tropospheric aerosol was observed to contain little or no mineral dust and contributed negligibly to the total columnar mass or extinction.

As shown in Figure 4.13, within the boundary layer, extinction coefficients derived from the sunphotometer data were approximately 25% greater than those calculated based on the size distribution measurements. Agreement with the nephelometers was significantly better, suggesting that the disagreement with the sunphotometer may be a result of larger particles that would not reach the nephelometers, but would affect the sunphotometer measurement. As with approximately half of the flights, no FSSP data were available in this case, and therefore the previously discussed extrapolation could result in an underestimation of the concentration of large, sea salt particles. Scattering and extinction coefficients within the free troposphere were approximately two orders of magnitude less than within the boundary layer, resulting in an increase

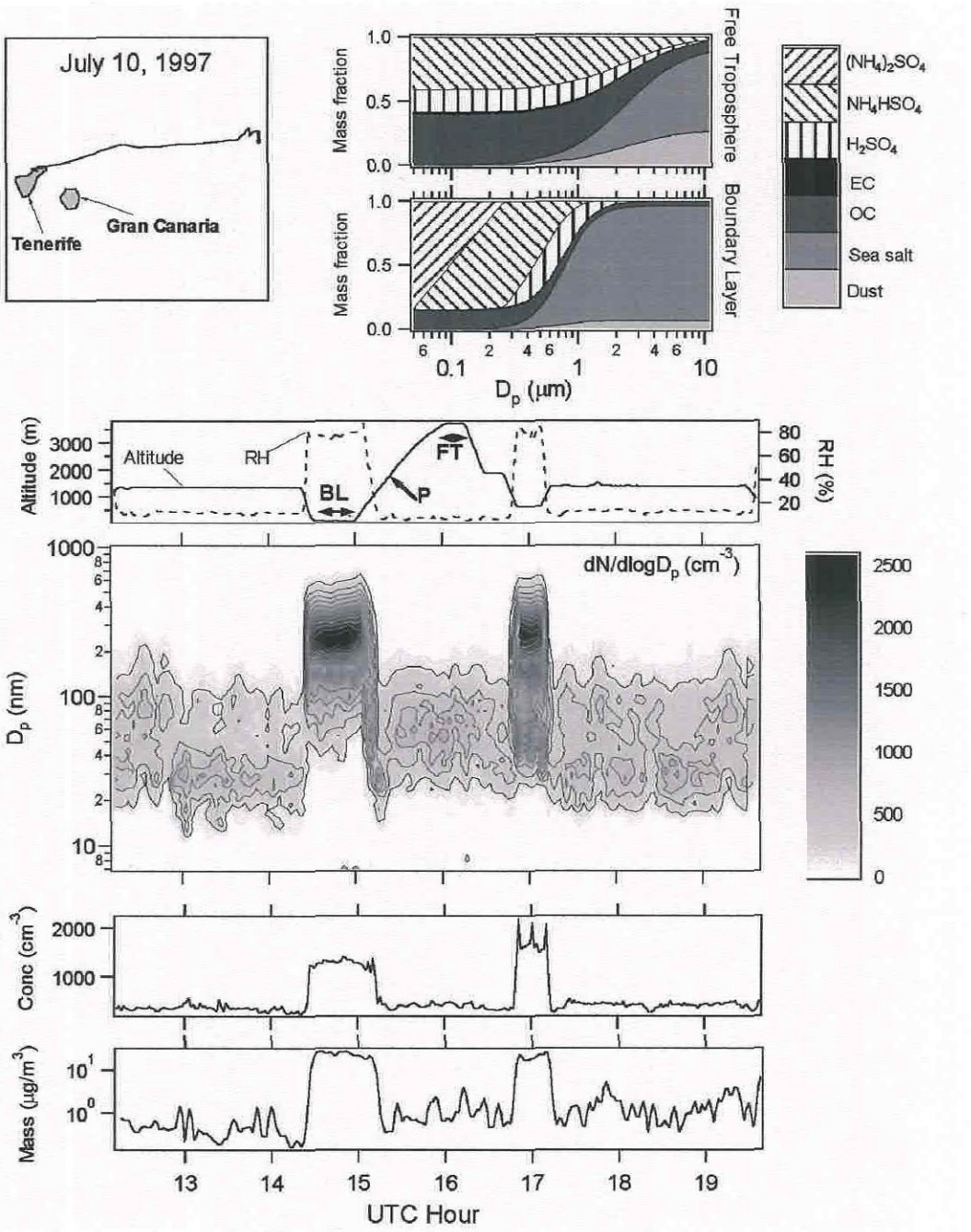


Figure 4.12: Size distributions and derived properties from the July 10 flight. Shown are the assumed chemical compositions, the flight track, the relative humidity and pressure during the flight with averaging periods indicated (BL = boundary layer, FT = free troposphere, and P = altitude profile), an image plot showing the relative change in size distribution as a function of time, and the integrated number concentration and dry aerosol mass as functions of time.

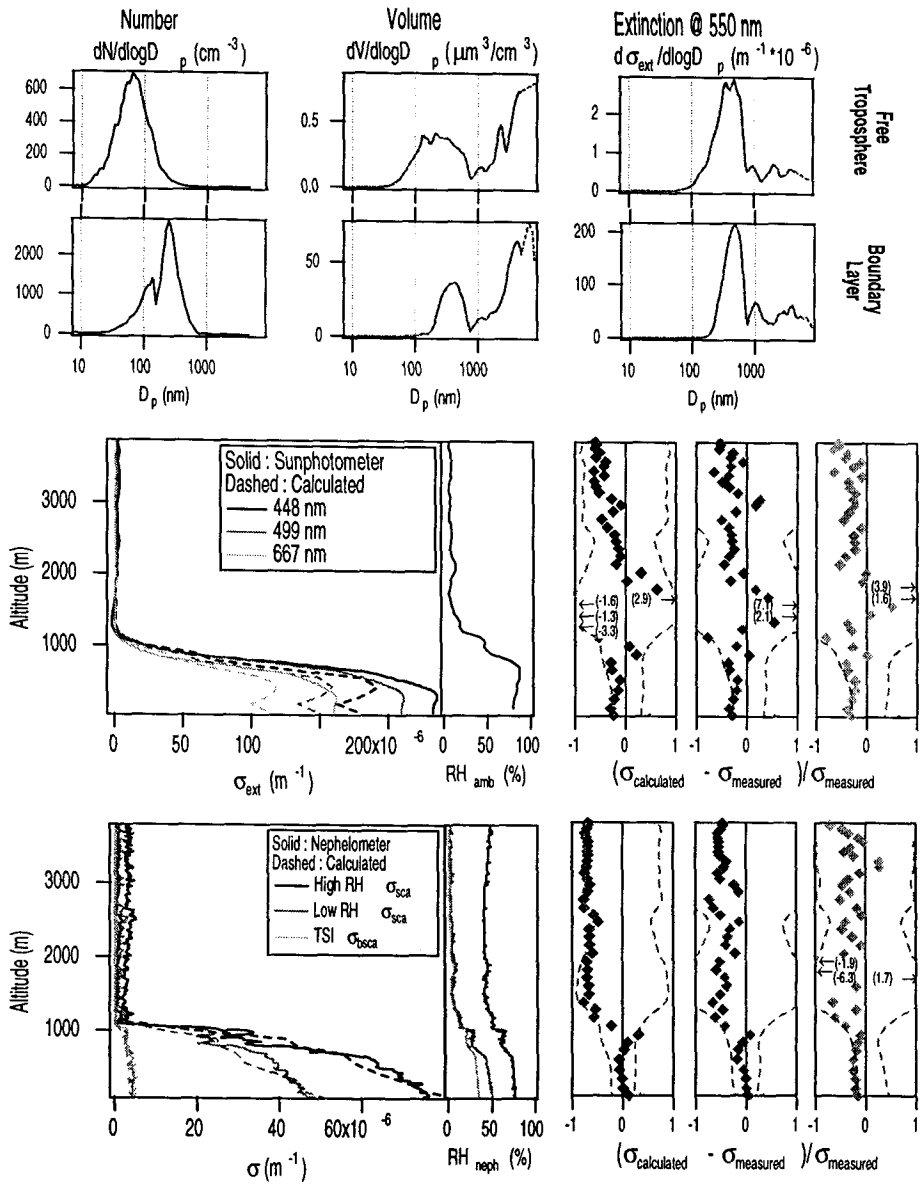


Figure 4.13: Size distributions and optical comparisons from the July 10 flight. Shown are the number, volume, and extinction distributions for the averaging periods shown on Figure 4.12, the comparison between the calculated and measured extinction coefficients corresponding to three of the sunphotometer wavelengths, and the comparison between the calculated and measured scattering coefficients for the nephelometers. Associated with each of the comparisons is a difference plot that presents the fractional discrepancy between the calculated and measured property (diamonds) along with the uncertainty bounds (dashed lines) calculated from the perturbations listed in Tables 4.2 and 4.3. To provide greater detail for the majority of the data points, fractional discrepancies greater than 1 are presented as arrows, with the actual discrepancy shown in parentheses.

in the importance of the estimated random errors, and an increase in the scatter observed in the difference plots.

**July 17, 1997** The last of the case studies focused on the properties of a dust layer significantly more effective at light extinction than that encountered during July 8. KNMI back trajectories suggested that the air parcel arriving in the boundary layer passed adjacent to Europe making no direct contact, while most of the back trajectories arriving in the free troposphere originated over Africa. Since the goal of this mission was to characterize the dust layer, the flight was conducted primarily south of Tenerife where boundary layer measurements were subject to contamination from the island. This flight track is shown in Figure 4.14. On two occasions, the aerosol number concentration reached approximately $10^4$ $cm^{-3}$, suggesting influence from sources on Tenerife. Size distributions and integrated number concentration corresponding to these events have not been included in the plots to allow for more detail for the uninfluenced data. Measurements of both organic and elemental carbon at IZO were thought to be unreasonably high for this date (J. Putaud, 1998, personal communication) and therefore, the assumed chemical composition was based on the average of the measurements made the previous and following days.

As shown in Figure 4.15, the coarse Saharan dust particles were observed to account for essentially the entirety of the aerosol mass and extinction coefficient within the free troposphere. The number size distribution within the boundary layer is almost identical to that measured during the June 21 flight. Relative to the June 21 flight, however, the submicron aerosol contributed significantly more to the extinction coefficient.

Results from comparisons between calculated and derived optical properties were similar to those from the July 8 flight, with discrepancies in excess of the estimated uncertainties only for those comparisons with the nephelometers in the dust layer. Some possible explanations for this disagreement are given in the discussion of the July 8 mission. It is not clear whether the variability in the size distribution based extinction coefficient as a function of altitude, or the lack thereof in the sunphotometer

data, is a true representation of the boundary layer structure. The ambient relative humidity profile seems to have a shape similar to the calculated values, though much less exaggerated. As has been true in the boundary layer for most of the optical comparisons, the derived extinction coefficients are less than those measured by the sunphotometer.

## 4.5 Summary

Aerosol size distributions were measured using a DMA and two OPCs during 21 flights conducted as part of the ACE-2 field campaign. Great care was taken to ensure the accuracy of the individual size measurements and of the ultimate integrated distribution to which they contributed. Aerosol characteristics observed in this region were varied, primarily resulting from the extent of contact the surrounding air mass made with Europe or Africa prior to its arrival. To permit description of average aerosol properties, boundary layer aerosols in this region can generally be categorized as background or continentally influenced, while free tropospheric aerosols can be differentiated on the basis of the presence or absence of a Saharan dust layer. Similar to previous studies conducted in this area, the number size distributions within the boundary layer were found to be bimodal during relatively clean conditions, but possessed only a single, accumulation, mode during more polluted conditions. Free tropospheric aerosols consistently had only a single mode that typically peaked below 100 nm diameter.

Detailed analyses were performed for four case studies that, collectively, spanned the range of aerosol types encountered. Of particular interest for these case studies were radiative closure comparisons performed between the vertically-resolved aerosol optical characteristics as determined through the use of the aerosol microphysical data, and those measured directly by a multi-wavelength sunphotometer and three nephelometers. While differences did exist between the derived and measured quantities in some cases, in general, the agreement obtained was within the uncertainty expected. Averaged over the four case studies, the derived extinction coefficient was

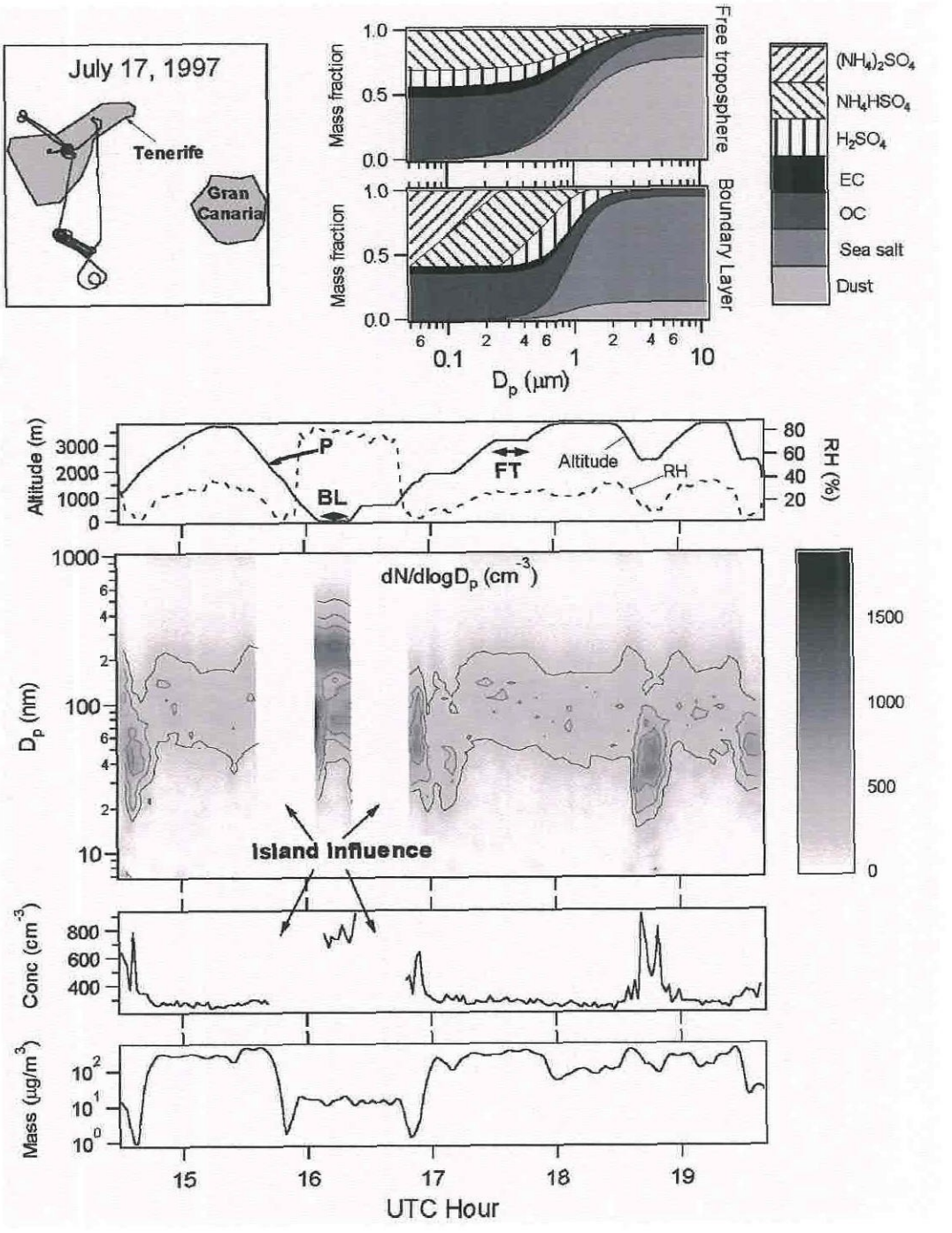


Figure 4.14: Size distributions and derived properties from the July 17 flight. Shown are the assumed chemical compositions, the flight track, the relative humidity and pressure during the flight with averaging periods indicated (BL = boundary layer, FT = free troposphere, and P = altitude profile), an image plot showing the relative change in size distribution as a function of time, and the integrated number concentration and dry aerosol mass as functions of time.

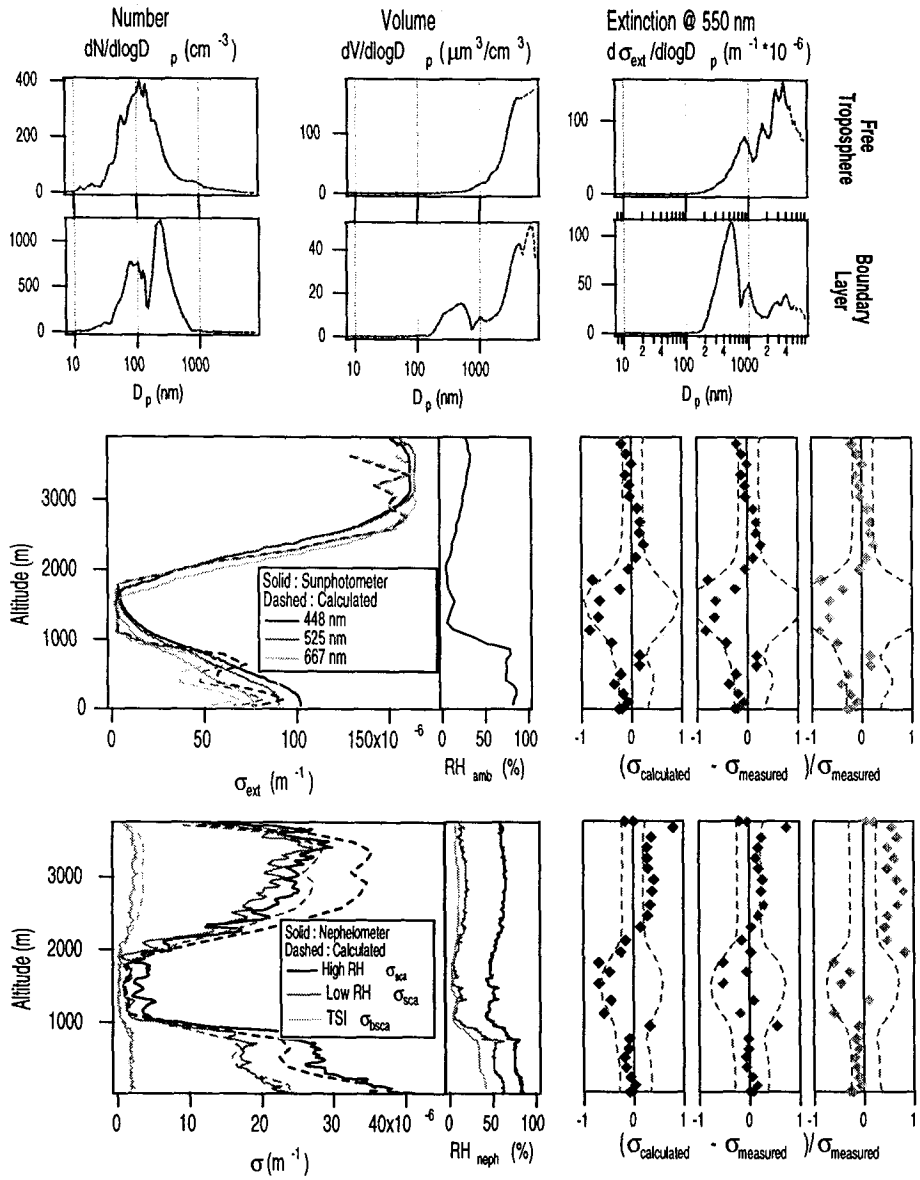


Figure 4.15: Size distributions and optical comparisons from the July 17 flight. Shown are the number, volume, and extinction distributions for the averaging periods shown on Figure 4.14, the comparison between the calculated and measured extinction coefficients corresponding to three of the sunphotometer wavelengths, and the comparison between the calculated and measured scattering coefficients for the nephelometers. Associated with each of the comparisons is a difference plot that presents the fractional discrepancy between the calculated and measured property (diamonds) along with the uncertainty bounds (dashed lines) calculated from the perturbations listed in Tables 4.2 and 4.3. To provide greater detail for the majority of the data points, fractional discrepancies greater than 1 are presented as arrows, with the actual discrepancy shown in parentheses.

2.5% greater than that measured by the sunphotometer for measurements made in the clean boundary layer, but was 13%, 3.3%, and 17% less than that measured within the polluted boundary layer, free troposphere with a dust layer, and free troposphere without a dust layer, respectively. For comparisons with the non-humidified nephelometer, the averaged derived scattering coefficient exceeded the measured value by 4.7% and 17% in the polluted boundary layer and dust-laden free troposphere, respectively, but was 9.6% and 41% less than that measured for background boundary layer and free tropospheric aerosols, respectively. The simultaneous agreement with the variety of instruments on board, each of which was sensitive to different aspects of the sampled aerosol population, limits the degree to which potential multiple errors in the size distribution and related analysis could simply offset one another, as might be the case if comparison with a single measurement at a single wavelength were made. It is clear from the case studies that direct comparison between the partial scattering coefficients measured by the nephelometers and the total extinction coefficient derived from the sunphotometer measurements, without careful consideration of the size distributions, would lead to substantial error. Future improvements in the sizing instruments themselves, as well as the simultaneous measurement of time and size-resolved aerosol chemical composition, will improve the ability to perform in situ radiative closure on the atmospheric aerosol.

# Chapter 5 Airborne Analysis of the Los Angeles Aerosol

*Atmospheric Environment*, in press

**Abstract**

As part of the Southern California Ozone Study (SCOS), a research aircraft was employed during August and September of 1997 to characterize the physical and chemical properties of the aerosol present over the Los Angeles Basin. Aerosol size distributions measured using a differential mobility analyzer and two optical particle counters were combined with filter-based composition measurements to derive a physicochemical description of the aerosol sampled. The accuracy of this description was evaluated through comparison of derived and directly measured aerosol properties including mass, absorption coefficient, hemispherical backscattering coefficient, and total scattering coefficient at two different relative humidities. The sampled aerosol exhibited a complex vertical structure possessing multiple elevated aerosol layers. The most pronounced of these layers were observed to form by injection of aerosol above the ground-level mixed layer along the southern edge of the San Gabriel Mountains, which form the northern boundary of much of the Los Angeles Basin. Over multiple inland areas, additional layers were observed at about 2500 m above sea level (asl), while off the coast of Santa Monica, thin but concentrated layers were detected about 500 m asl. In addition to the sharp vertical gradients in aerosol concentration observed, horizontal gradients at multiple locations were found to be sufficient to result in more than 50% variability within a 5 x 5 km computational grid cell commonly used in atmospheric models. Vertically-resolved aerosol measurements made over one location during several flights, as well as over several locations during a morning and afternoon flight on the same day, were used to investigate the temporally- and spatially-resolved impact the aerosol had on gas-phase photolysis rates. These calculations predict that for a 10° zenith angle the sampled aerosol enhanced photolysis rates by up to about 5%, although a slight decrease was often observed near ground level.

## 5.1 Introduction

Southern California has long struggled to comply with state and federal air quality standards. Faced with a steadily increasing population and tightening ozone and particulate matter standards, further emissions reductions will be necessary. Extensive atmospheric modeling efforts have provided a means for linking specific emission control scenarios with probable air quality outcomes (see, for example, Meng et al., 1997). However, the complex terrain and meteorology associated with Southern California, coupled with inherent uncertainties in model input fields, complicates these efforts. Aircraft-based measurements (Blumenthal et al., 1978; Wakimoto and McElroy, 1986) have demonstrated that vertical transport in the Los Angeles area is not consistent with the simple representation of a mixed layer trapped below a temperature inversion. Recently, three-dimensional meteorological models have provided further insight into mechanisms responsible for formation of distinct pollution layers that exist above the Los Angeles Basin for extended periods of time (Lu and Turco, 1994, 1995). Successful prediction of ground-level concentrations can only be accomplished if the behavior and nature of material aloft are adequately described. In addition to the poorly characterized variation of species concentrations with altitude, strong horizontal gradients pose a unique problem for models; observed variations within a computational grid cell (typically 5 x 5 km) call into question the assumption that concentrations are uniform inside a grid volume. Use of a single measurement within a grid cell to represent the entire cell can lead to uncertainties as high as 25-45%, depending on the species of interest (McNair et al., 1996).

During the summer and fall of 1987, the Southern California Air Quality Study (SCAQS) was undertaken to provide a sufficiently detailed data set to test the capabilities of available meteorological and air quality models. Data from SCAQS, particularly a small number of multi-day episodes, have served as the foundation for most of the modeling work in the years since (Pandis et al., 1992; Harley et al., 1993; Pandis et al., 1993; Jacobson, 1997; Lurmann et al., 1997; Lu et al., 1997; Meng et al., 1998). Ten years after SCAQS, during the summer and fall of 1997, the Southern

California Ozone Study (SCOS) was conducted in order to supplement the data set acquired during SCAQS by employing a network of emissions, meteorological, and air quality measurements. The stated goals of SCOS were:

1. Update and improve the existing aerometric and emission databases and model applications for representing urban-scale ozone episodes in Southern California.

2. Quantify the contributions of ozone generated from emissions in one Southern California air basin to federal and state ozone standard exceedances in neighboring air basins.

3. Apply modeling and data analysis methods to design regional ozone attainment strategies.

To satisfy goal 2, the study covered an extensive region that was roughly bounded by the Channel Islands to the West, the San Joaquin Valley to the North, and the California state border to the East and South. In all, the study encompassed approximately 53,000 square miles, although a large fraction of the measurements were made within the Los Angeles Basin. SCOS was conducted between mid-June and mid-October when the highest pollutant concentrations are usually observed in the region. However, during this campaign unusually high sea surface temperatures caused by a significant El Niño event resulted in deeper marine layers and enhanced mixing relative to typical conditions in Southern California. Hence, air pollutant concentrations tended to be somewhat lower during this study than is common for the region.

As its name implies, the Southern California Ozone Study was conducted primarily to improve our understanding of ozone and its gas-phase precursors. A smaller, but still extensive, component of the study focused on understanding the formation and evolution of the atmospheric aerosol. The expanded monitoring network in place for the ozone study facilitated interpretation of aerosol measurements. As part of the aerosol component of SCOS, a research aircraft was utilized during August and September of 1997 to provide a three-dimensional characterization of the Los Angeles aerosol. This paper presents a description of the measurements obtained by that

aircraft during the study period, and an analysis of the impact the aerosol column may have on key gas-phase photolysis rates involved in ozone production.

## 5.2 Instrumentation and Analysis

Between August 27 and September 12, 1997 the Center for Interdisciplinary Remotely-Piloted Aircraft Studies (CIRPAS) Pelican aircraft flew 12 missions over the Los Angeles Basin. The Pelican is a Cessna Skymaster that has been modified by replacing the front engine with an extended nose cowling that serves as the primary instrumentation bay. The resulting pusher configuration is ideal for aerosol measurements because it minimizes the disturbance of the atmosphere prior to sampling. Optical particle counters were mounted on each of the wings, while the remaining instruments were located inside the aircraft. These latter instruments sampled from two parallel inlets, each of which included a cyclone with a nominal cut size of 2.5 $\mu$m. Since the cyclones were positioned immediately downstream of the inlet opening, little drying of the particles was likely prior to removal of the coarse mode. Table 5.1 contains a complete list of instruments on board the Pelican during SCOS.

### 5.2.1 Filter Samples

The chemical composition of the aerosol was probed using a filter system employing three parallel sampling trains, each having a flow rate of 24 L min$^{-1}$. Separate trains were used for analysis of trace metals, elemental and organic carbon, and inorganic ions. Each sampling train consisted of three identical filter cassettes, allowing sequential exposure of multiple filters through the use of cockpit-activated solenoid valves that were in-line with each of the filter cassettes. During SCOS, three sets of filter samples were taken during each of the first six flights, with two sets taken on the seventh flight. Filters were unloaded immediately following each flight and remained refrigerated during storage and transport until analysis. Several filter blanks were taken from each sampling train and were used to correct for the samples analyzed.

Table 5.1: Measurements made on board the Pelican.

| Property measured | Instrument | Time |
|---|---|---|
| *Aerosol measurements* | | |
| Inorganic ions, trace metals, EC/OC | sub-2.5 $\mu$m filter samplers | $\sim$ 1 h |
| Particle size (0.01 - 0.5 $\mu$m) | TSI 3071 DMA / 3010 CPC | 1 min |
| Particle size (0.15 - 3.0 $\mu$m) | PMS PCASP | 1 s |
| Particle size (0.5 - 20 $\mu$m) | PMS FSSP | 1 s |
| 3-color light scattering coefficient (total and hemispherical backscattering) | TSI 3563 nephelometer | 1 s |
| Light scattering / RH relationship | UW humidigraph (Radiance Research nephelometers) | 6 s |
| Light absorption coefficient | Radiance Research PSAP | $\sim$ 1 min |
| *Radiation measurements* | | |
| Total solar | Eppley pyranometer | 1 s |
| UV | Eppley radiometer | 1 s |
| *Meteorological measurements* | | |
| Pressure (static and dynamic), temperature, and dew point | Various | 1 s |

The first sampling train used a Teflon filter to collect samples for trace metal analysis. Inductively-coupled plasma mass spectrometry (ICP-MS) was used to quantify $Na^+$, $Al^{3+}$, $K^+$, $Ni^{2+}$, $Zn^{2+}$, $Mg^{2+}$, $Si^{4+}$, $Fe^{3+}$, and $Cu^{2+}$ for each of the filters. With the exception of $Na^+$ and $Mg^{2+}$ that were assumed to be associated with sea salt particles, each of the metals was assumed to be present as oxides ($Al_2O_3$, $SiO_2$, $K_2O$, $Fe_2O_3$, NiO, CuO, and ZnO) for determination of aerosol mass. Uncertainty in total aerosol mass introduced as a result of this assumption is relatively low since the elements analyzed typically constituted only a small fraction of the aerosol.

Elemental and organic carbon collected on quartz filters in the second sampling train was analyzed through thermal optical reflectance (Chow et al., 1993) by researchers at the Desert Research Institute (DRI). To account for the positive artifact resulting from organic vapor adsorption on the filter, a quartz back-up filter was used, with the corrected organic aerosol mass assumed to be the difference between that measured on the front and back filters. Since oxygen and hydrogen are not detected in this type of analysis, organic carbon loadings were multiplied by 1.4 to estimate total organic aerosol mass (White, 1990).

Table 5.2: Detection limits for species analyzed.

| Species | Analytical Limit ($\mu$g/filter) | Ambient Conc. ($\mu$g/m$^3$) |
|---|---|---|
| $SO_4^{2-}$, $NO_3^-$, $NH_4^+$ | 0.8 | 0.4 |
| OC | 2 | 1 |
| EC | 0.5 | 0.3 |
| Fe, Si, K | 0.1 | 0.05 |
| Na | 0.01 | 0.005 |
| Mg, Ni, Cu, Zn, Al | 0.001 | 0.0005 |
| mass | 10 | 5 |

The final sampling train employed an MgO denuder to remove nitric acid in order to minimize the positive artifact that it might otherwise cause. Downstream of the denuder, a Teflon filter was used to collect aerosol for inorganic ion analysis. Researchers with DRI used ion chromatography to analyze and, and colorimetry to quantify. The mass measured on the nylon back-up filter was assumed to be volatilized ammonium nitrate, and was, therefore, used to correct the and mass measured on the Teflon filter.

To assess the degree to which the aerosol mass was accounted for through the speciation analyses, filters collected in trains A and C were analyzed by gravimetry. These analyses were conducted by researchers at DRI under controlled conditions in which the relative humidity was maintained at between 45 and 55%. The correction applied to the and concentrations to account for ammonium nitrate volatilization was also applied to the gravimetric mass.

Detection limits for each aerosol species analyzed are listed in Table 5.2. Aerosol mass for each of the 20 sets of filters analyzed is shown in Figure 5.1. With the exception of the September 4 and 5 flights, filter samples represent the integration of the aerosol present over a relatively wide area and over about 2 km variation in altitude. These spatially-unresolved filter measurements were used to gain a general understanding of the chemical nature of the aerosol and to aid in the analysis of time-resolved size distributions, but were not used to directly assess variations in composition within the study area.

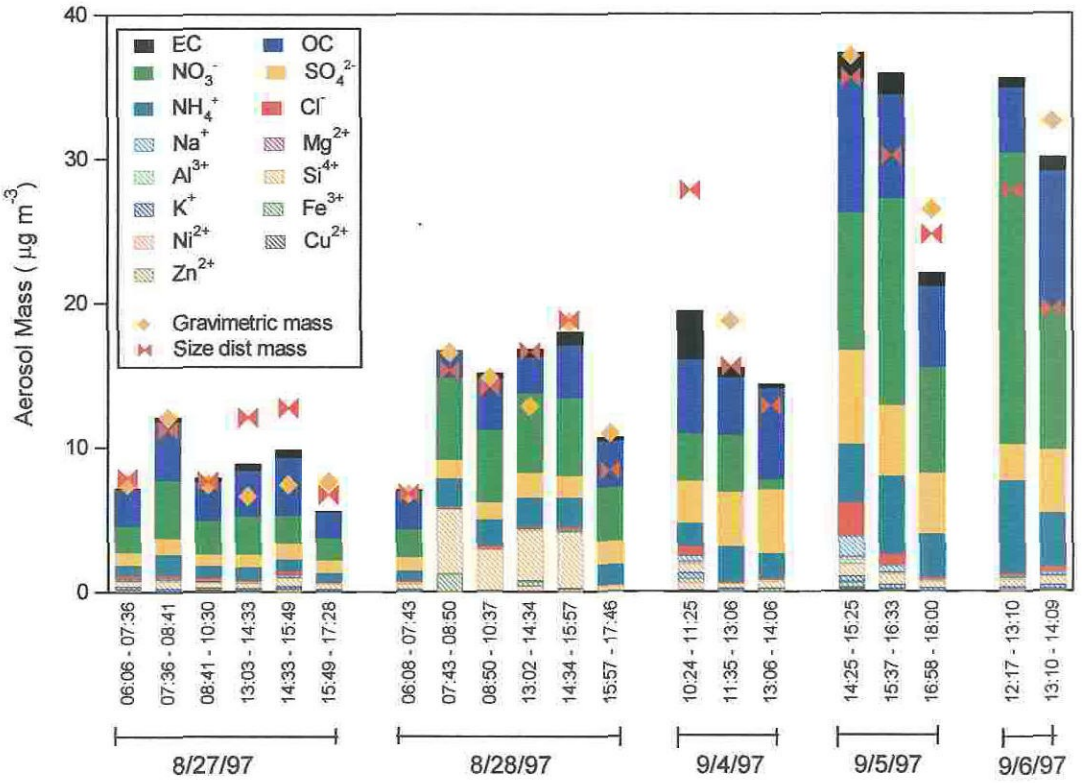


Figure 5.1: Fine aerosol chemical composition during the seven flights for which samples were collected. Also shown is aerosol mass determined gravimetrically, and through integration of the size distributions.

### 5.2.2 Optical Measurements

Three integrating nephelometers and an absorption photometer provided details of the optical and hygroscopic properties of the aerosol sampled during SCOS. The University of Washington Passive Humidigraph, which consists of two Radiance Research nephelometers operated in parallel at different relative humidities (RH), was used to investigate the relationship between humidity and aerosol light scattering. In general, humidities within the dry and wet nephelometers bracketed the ambient RH. A TSI 3563 nephelometer that measures total scattering and hemispherical backscattering at blue (450 nm), green (550 nm), and red (700 nm) wavelengths was operated at a humidity slightly below that of the drier of the two Radiance Research nephelometers. Each of the nephelometers was calibrated prior to, or during, the study using gases with known scattering properties.

A Radiance Research Particle Soot Absorption Photometer (PSAP) was used to make time-resolved measurements of the absorption properties of the dry aerosol. The PSAP continuously records transmittance of light (567 nm) through two regions on a filter, one of which has an aerosol-laden flow passing through it, while the other is used as a reference. The aerosol absorption coefficient, $\sigma_{ap}$, is determined from the rate of change of the transmittance ratio between the two regions. PSAP calibration results described by Bond et al. (1999) were used to analyze the data obtained. It has been observed that variations in transmittance ratio unrelated to increased particle loading occur as a result of pressure variations within the instrument. Only during constant altitude legs when the observed change in transmittance due to particle loading dominated over that caused by pressure variations were data analyzed.

### 5.2.3 Size Distribution Measurements

By integrating measurements from a differential mobility analyzer (DMA) and two optical particle counters (OPCs), aerosol size distributions spanning the range from 10 nm to >20 $\mu$m in diameter were determined with 1 min time resolution. A TSI 3071 cylindrical DMA was operated with a TSI 3010 condensation particle counter to size

particles with diameters between approximately 10 and 500 nm. Each of the DMA flow rates was actively controlled to minimize fluctuations induced by pressure changes within the instrument. The voltage applied to the DMA was scanned over 45 s, and was automatically adjusted to maximize particle size range, while remaining below the pressure and temperature dependent threshold for electrostatic breakdown. A wing-mounted Particle Measuring Systems (PMS) Passive Cavity Aerosol Spectrometer Probe (PCASP-100X) sized particles ranging from approximately 140 nm to over 3 $\mu$m. The PCASP was calibrated prior to SCOS with polystyrene latex (PSL) particles. Mie theory calculations that accounted for the angular configuration of the light receptor in the PCASP were used to adjust this PSL calibration to that expected for particles of any specified complex index of refraction. Mounted on the wing opposite to the PCASP was a PMS Forward Scattering Spectrometer Probe (FSSP-100). By utilizing an external laser / detector, the FSSP causes only minimal disturbance to large particles and cloud droplets. The 1 Hz measurements of both the PCASP and FSSP were averaged over the $\sim$1 min measurement time of the DMA.

The PCASP and DMA systems both change the relative humidity of the aerosol during the act of sampling, while the FSSP has little effect on this important parameter. To combine these measurements into a coherent description of the sampled aerosol, the ambient particle size distribution must be estimated from the perturbed data. An accurate description of the effect of humidity on particle size requires knowledge of, or assumptions about, the aerosol composition, mixing state, and deliquescence state. Filter samples taken during the majority of the Pelican flights were used to estimate the composition of the sampled aerosol during the respective filter integration interval. For those flights during which no filter samples were taken, the average composition analyzed during the flights with filter measurements was used. Since filter samples were not size-resolved, it was assumed that size-dependent composition and mixing relationships were similar to those described by Zhang et al. (1993) in their analysis of data taken during SCAQS. External mixtures of salt particles were assumed so that available single-salt solution thermodynamics data (Tang and Munkelwitz, 1994; Tang, 1996; Tang et al., 1997) could be used for particle growth

/ evaporation calculations. Tang (1996) showed that only minor differences exist in overall optical properties of internal and external mixtures of common nitrates and sulfates. Moreover, the similar densities of common nitrates and sulfates limit the uncertainty in the calculated aerosol mass that might be caused by this assumption. Hygroscopic growth was considered only for the salt species, and not for carbon or dust. The assumption that carbonaceous aerosol is non-hygroscopic is known to be incorrect for at least some organic species found in the aerosol phase (Saxena et al., 1995). However, in their interpretation of SCAQS impactor data, Zhang et al. (1993) suggest that externally mixed carbonaceous particles were non-hygroscopic, while carbon internally mixed with salt particles was less hygroscopic than the salt itself. The relatively low humidity encountered throughout the present study, and generally characteristic of the region, further limits uncertainties caused by this assumption.

The ambient relative humidity measured during SCOS often lay between the crystallization and deliquescence points of the salt species known to be present in the aerosol. Whether the aerosol would be wet or dry under these circumstances depends on the RH history it experienced. Humidity data taken during the flights, coupled with continuous ground-based measurements at five locations in the Los Angeles area, were used to estimate the maximum humidity encountered by the aerosol that was sampled during a given flight. As an estimate of the uncertainty that this assumption might introduce, it was determined that, averaged over all of the flights, PM2.5 (dry aerosol mass = 2.5 $\mu$m aerodynamic diameter) calculated using the assumption that the maximum humidity encountered was the ambient humidity at that time is only 5.1% greater than that calculated assuming all salts had previously deliquesced. After adjusting for relative humidity differences, excellent agreement in measured concentration was observed in the overlapping size range of the PCASP and FSSP. In general, the size distribution recovered from the DMA had a similar shape to that measured by the PCASP, but was shifted by about 10% to larger size. The cause of the discrepancy is not known, but it generally had little impact on derived aerosol mass and optical properties. Lacking definitive evidence of the relative accuracy of the different measurements, individual distributions were simply averaged in overlapping

size ranges.

### 5.2.4 Optical and Mass Closure

Although composition and optical measurements afford valuable information about the properties of the sampled aerosol, only an accurate physicochemical description can provide a full range of spatially and temporally resolved aerosol characteristics. In order to test the validity of the size distribution-based physicochemical description of the aerosol, a number of closure comparisons were performed with the optical and composition measurements. The utility of such comparisons is that they provide confidence in the over-determined set of measurements when closure is achieved, and indicate potential sources of error when it is not.

To estimate aerosol mass collected on the filters during sampling intervals, aerosol size distributions were first adjusted to the relative humidity within the cyclone, which was slightly warmer and drier than outside. The density of each aerosol type considered was then calculated and used to determine the appropriate cyclone penetration efficiency s-curve. For hygroscopic particles, density was calculated as a function of relative humidity, whereas constant densities of 2.6 g $cm^{-3}$ for dust (Tegen and Fung, 1994), and 2.0 g $cm^{-3}$ and 1.4 g $cm^{-3}$ for elemental and organic carbon, respectively (Larson et al., 1988), were used. The aerosol mass of those particles that passed through the cyclone was then calculated through integration of the size distribution. Aerosol mass derived in this way is included in Figure 5.1. Although there are some differences between the three measures (species sum, gravimetric, and size distribution integration) of aerosol mass during a given filter interval, there are no pronounced systematic discrepancies.

As with aerosol mass calculations, modification of the aerosol size distribution to account for removal in the cyclone is necessary for comparison with the various optical instruments on board. The remaining particles are then adjusted to the relative humidity within each instrument. For those cases in which the relative humidity of the sample flow is reduced below the crystallization point of a given salt, only if the RH in

the humidified nephelometer is above the deliquescence point of the salt is it assumed to be hydrated. For analysis of scattering and absorption coefficients, constant refractive indices of 1.95 - 0.66$i$ for elemental carbon (Bergstrom, 1972) and 1.55 - 0.0$i$ for organic carbon (Larson et al., 1988) were assumed. The wavelength-dependent complex index of refraction of Saharan dust particles described by Patterson et al. (1977) was assumed to be representative of dust present in Los Angeles. Optical properties of dust vary with location and even time, but few representative data are available. Fortunately, the contribution of dust to scattering and absorption was generally small, minimizing the uncertainty in derived optical properties resulting from this assumption. Refractive index of aqueous aerosols was determined by the partial molal refraction approach of Moelwyn-Hughes (1961). For internal mixtures of salt and carbon, the volume-weighted average of the refractive indices of the components was used. Fuller et al. (1999) found that volume-weighted calculations tend to overestimate absorption of a mixed salt / elemental carbon particle relative to more physically realistic scenarios such as a salt shell that contains an elemental carbon inclusion. However, because of uncertainty in the mixing state and size distribution of carbon in the aerosol, the magnitude of the error remains unknown.

Mie Theory was used to predict the response of the optical instruments to the sampled aerosol with specified size-resolved concentration and refractive index. For comparison with the nephelometers, the angular sensitivity of the TSI 3563 (Anderson et al., 1996) was incorporated into the Mie Theory calculations. Figure 5.2 shows closure comparisons with the total scattering coefficient measured by each of the Radiance Research nephelometers, the 550 nm hemispherical backscattering coefficient measured by the TSI nephelometer, and the absorption coefficient measured by the PSAP. Data from each of the seven flights during which filter samples were taken are included in the comparisons with the three nephelometers, while data from only those flights that included extended constant altitude legs were included in the PSAP comparison to minimize biases caused by pressure variations. Although each comparison is characterized by some discrepancy, that with the PSAP is clearly the most significant. Potential causes of this disagreement include errors in the analysis of

carbon or in the distinction between organic and elemental carbon, errors in assumed mixing state and sphericity of the particles, and errors in the absorption measurement itself, potentially due to the broadside enhancement effect described by Fuller et al. (1999). It is unlikely that this discrepancy results from use of volume-weighted refractive indices in the size distribution-based calculations, since this would tend to increase the derived absorption coefficient, thereby improving agreement.

## 5.3 Three-Dimensional Aerosol Structure

A variety of flight patterns were utilized during SCOS in order to explore the three-dimensional distribution of the aerosol in the Los Angeles Basin. The pattern used during the first four missions of SCOS consisted of a sequence of ascending and descending spirals. Both spatial and temporal variations in the aerosol were explored by conducting one of these 4-hour missions in the morning and another in the afternoon on both August 27 and August 28. Meteorological measurements showed the temperature inversion on August 27 had a height of approximately 350 m until breaking up in the early afternoon. A weak offshore flow was observed during the evening, followed by on-shore flow and an inversion having a height of approximately 500 m the following day. Peak 1-hour ozone concentrations observed in the Southern California Air Basin were 116 and 132 ppb on August 27 and 28, respectively.

To present the three-dimensional structure of the aerosol during this period, data from spirals along two cross sections have been considered. An east-west cross section was chosen that includes spirals over Santa Monica, El Monte, Azusa, Pomona, and Rialto, while a north-south cross section includes spirals over Altadena, El Monte, Fullerton, and Seal Beach. It is not possible to completely deconvolute the spatial variations between spiral locations from variations that result from evolution or advection of the aerosol during the course of a flight. Nor is it possible to predict with confidence the aerosol properties at a point along one of the cross sections through simple interpolation of measurements made. Nevertheless, Figures 5.3 and 5.4 present data along these cross sections as if they were snapshots in time exhibiting smooth

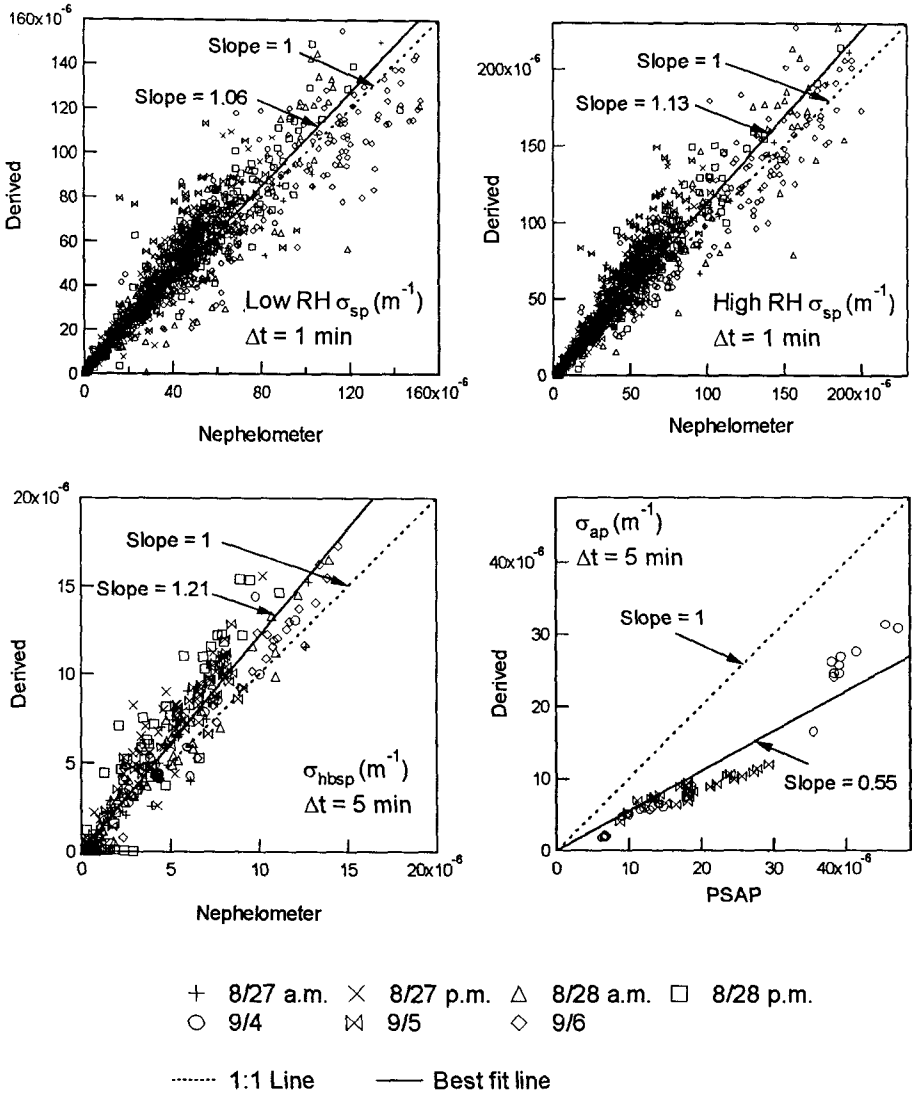


Figure 5.2: Closure comparisons between derived and directly measured optical properties. Data presented are from those flights during which filter samples were collected. Comparisons shown include total scattering coefficients measured by the Radiance Research nephelometers at varying relative humidity, hemispherical backscattering at 550 nm measured by the TSI nephelometer, and absorption measured by the PSAP.

variations between locations. PM2.5 has been considered here because of its regulatory relevance. Shown at the top of these figures are contour plots of aerosol mass derived from measurements made at the lowest point of each spiral. Also presented are the east-west (E-W) and north-south (N-S) cross sections considered. Beginning on the morning of August 27, the aerosol was most concentrated over the inland valleys between El Monte and Chino, where PM2.5 exceeded 40 mg $m^{-3}$. Strong gradients in PM2.5 are apparent along both cross sections between the coast and inland areas. Only a weak aerosol layer at approximately 1000 m above sea level (asl) is visible above the ground-level polluted layer. Along the east-west cross section, little change is observed in near-ground level aerosol mass from morning to afternoon, although the columnar aerosol burden over the inland areas increased, and a weak, but distinct, layer at ~400 m asl developed that stretched to Santa Monica. At approximately 1200 m asl along the north-south cross section, a much more intense aerosol layer is observed, in which PM2.5 exceeds 30 mg $m^{-3}$. These data suggest that aerosol was injected above the mixed layer at the southern edge of the San Gabriel Mountains and was then transported away from the mountains with the sea breeze return flow. Aircraft-based measurements have previously identified such elevated pollution layers both over Southern California (Blumenthal et al., 1978; Wakimoto and McElroy, 1986; Li et al., 1997) and over similar coastal regions (Wakamatsu et al., 1983; Lalas et al., 1983; Hoff et al., 1997). A second, less pronounced, layer is present approximately 200 m above the first. The two layers present along the east-west cross section the following morning are likely remnants of this (these) layer(s). As the ground-level mixed layer deepens in the afternoon of August 28, the morning layers cease to be distinct, suggesting that they mixed with the underlying layer. Along the north-south cross section, an elevated layer formed on August 28 in much the same way as was observed the previous day.

The climb and descent rates used during this study were typically 150 m $min^{-1}$, leading to a vertical resolution of ~150 m in the size distribution measurements. Aliasing due to this limited vertical resolution became excessive during several spirals, in which case the faster nephelometer measurements were examined. Figure 5.5 shows

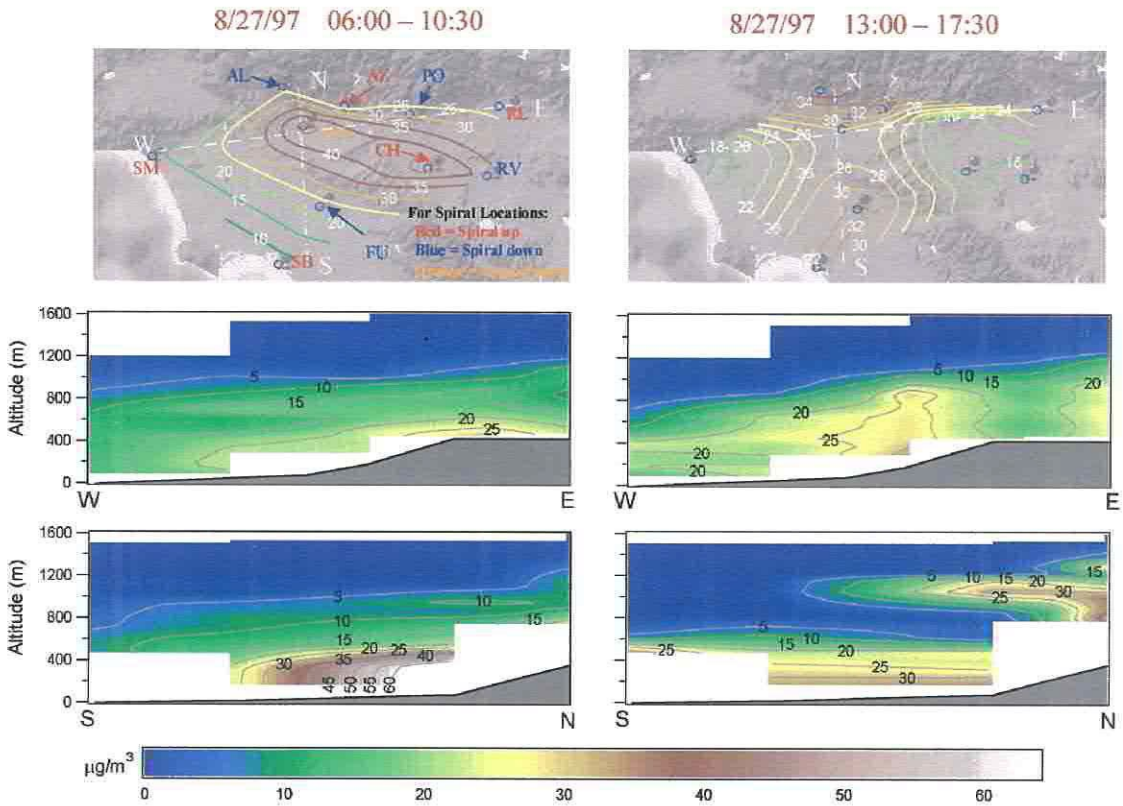


Figure 5.3: Distribution of PM2.5 throughout the Los Angeles basin as sampled during morning and afternoon flights on August 27. The top plots show contours of near-ground level aerosol mass as well as the east-west (E-W) and north-south (N-S) cross sections used in the image plots shown below. As indicated in the August 27 contour plot, spiral locations are Altadena (AL), Azusa (AZ), Chino (CH), El Monte (EM), Fullerton (FU), Pomona (PO), Rialto (RL), Riverside (RV), Santa Monica (SM), and Seal Beach (SB). Represented in the image plots is PM2.5 interpolated from adjacent spirals. The solid gray area at the bottom of each of the image plots represents the approximate ground level.

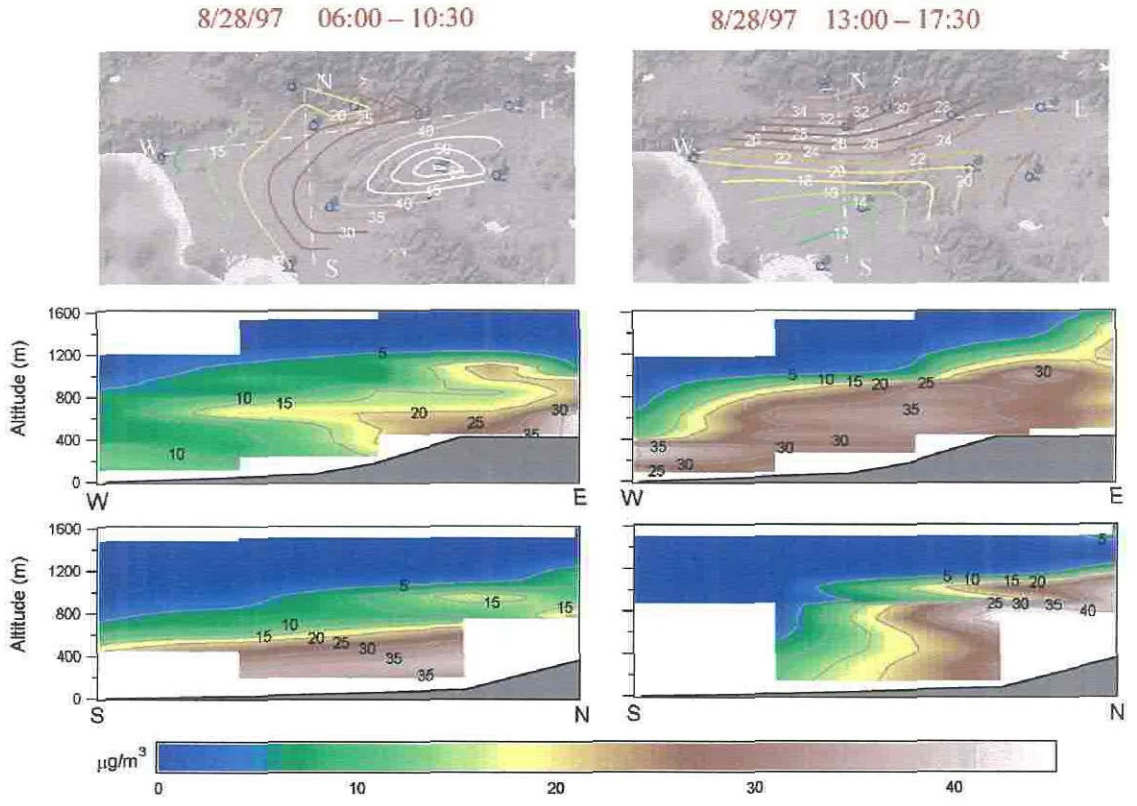


Figure 5.4: The same format as in Figure 5.3 for the aerosol sampled during morning and afternoon flights on August 28.

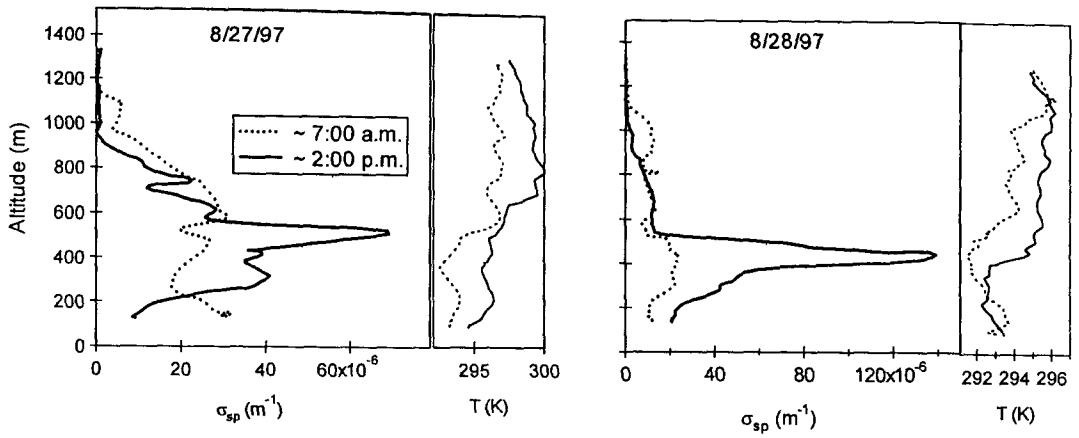


Figure 5.5: Vertical profiles of ambient temperature and aerosol scattering coefficient measured during spirals flown off the coast of Santa Monica on four missions conducted on August 27 and 28.

aerosol scattering coefficients recorded with the non-humidified Radiance Research nephelometer during each of the spirals flown off the coast of Santa Monica on the first four flights. The morning spirals show relatively little vertical variation on either day. With the strengthening of the sea breeze in the afternoon, pronounced, but thin (~100 m), aerosol layers developed. The scattering coefficient of 0.00014 $m^{-1}$ measured in the August 28 layer was among the highest observed at any location during the study. Like the layers over the inland areas, these coastal layers have been observed in previous studies and are attributed to vertical transport along the heated coastal ranges, followed by horizontal transport towards the coast as part of the sea breeze return flow (Lu and Turco, 1994).

During one flight on September 9 and two flights the following day three spirals over El Monte and two over Long Beach reached altitudes of over 3000 m. On both of these days upper level winds were from the south and west, and temperature inversions were present until mid-afternoon. Maximum 1-hour ozone concentrations were 105 and 113 ppb on September 9 and 10, respectively. Though the spirals were flown over a 32-hour period at two dissimilar locations, each encountered an aerosol layer at approximately 2500 m having a peak PM2.5 mass of about 2 mg $m^{-3}$, as

shown in Figure 5.6a. The early morning spiral flown over El Monte on September 9 indicates that a more concentrated layer may have been present above 3000 m, although no similar layers were observed during 3400 m spirals on the morning of September 10. The averaged mass distributions for the layers indicated by arrows in Figure 5.6a are presented in Figure 5.6b. There is a clear shift in the aerosol mass distribution within the 2500 m layer relative to the aerosol within either the ground level or 1500 m layers. This observation is consistent with an aerosol that has aged through condensation and coagulation.

Seven different flight patterns were employed for the twelve missions flown during SCOS, making analysis of day-to-day variations difficult. However, the majority of flight patterns included spirals over El Monte, Riverside, and Fullerton. These repeated spirals provide the data necessary for a statistical analysis of the aerosol over these locations. Day to day variations in the aerosol concentration and properties obscured any diurnal trends that might otherwise have been apparent. Therefore, in combining data from each set of spirals, no distinction was made between samples taken at different times. Figure 5.7 presents the mean and standard deviation of several intensive and extensive aerosol properties as a function of altitude for 10 spirals flown over both El Monte and Riverside, and 9 flown over Fullerton. The data have been smoothed to more clearly show vertical trends. As indicated in these plots, the aerosol variability at each location exceeds the mean variability between locations. Consistent with expectations, aerosol mass decreases with increasing altitude and with proximity to the coast. Aerosol number concentration was about 50% higher in El Monte than in Riverside, while aerosol mass was higher in Riverside, indicating that much of this increased mass results from growth of existing particles. Steadily improving air quality in Los Angeles, coupled with atypical meteorology associated with a strong El Niño event, led to significantly lower aerosol loadings during SCOS than during SCAQS ten years earlier. However, the relative contributions of fine (PM2.5) and coarse (PM10 - PM2.5) fractions remained much the same. Chow et al. (1994) found that, during SCAQS, PM2.5 constituted between 50 and 67% of PM10, while near-ground level measurements made on board the Pelican during

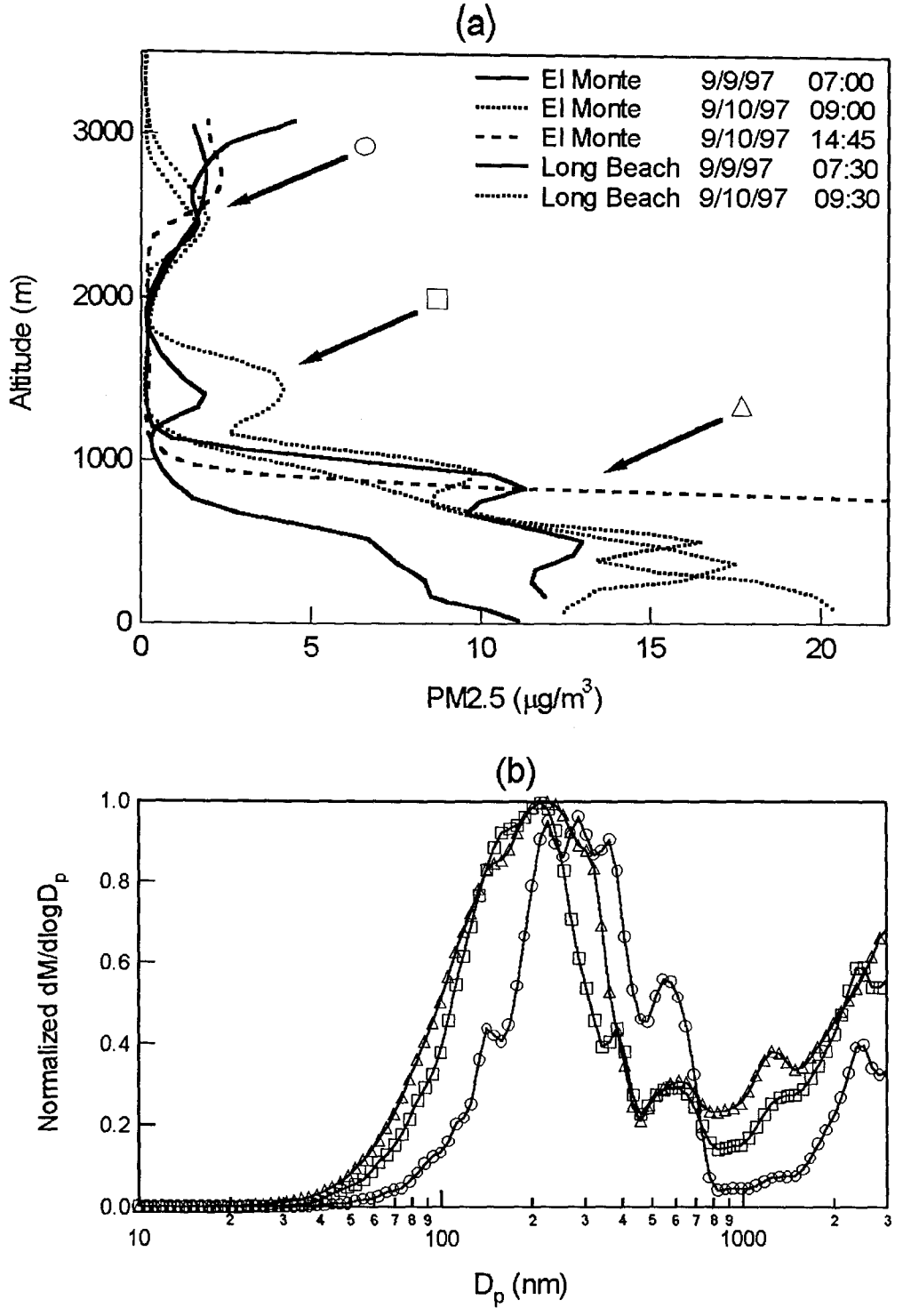


Figure 5.6: (a) Vertical profiles of PM2.5 measured during 3000+ m spirals flown over El Monte and Long Beach, and (b) normalized mass size distributions averaged over each of the layers indicated by arrows in (a)

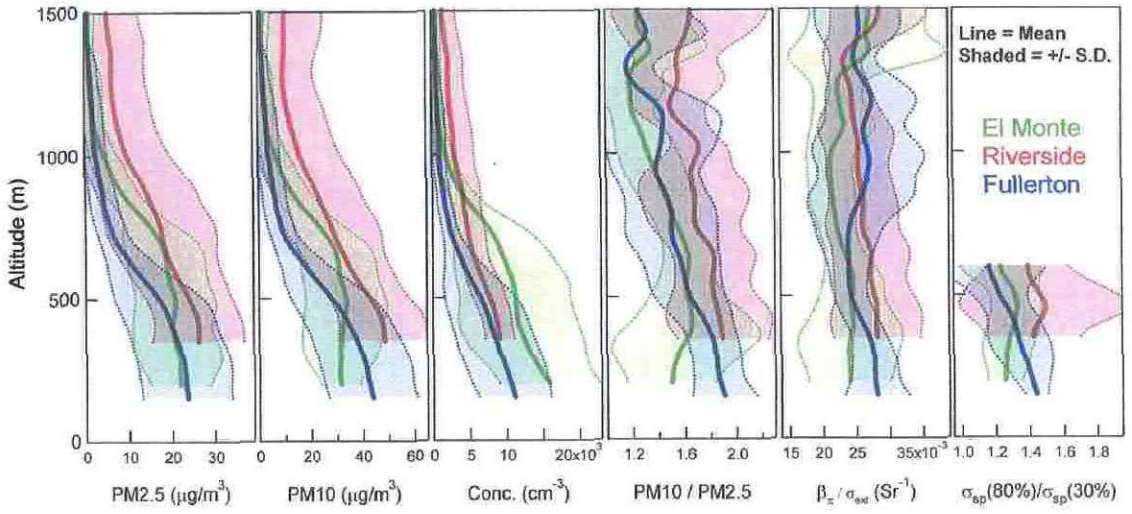


Figure 5.7: Vertical profiles representing the mean and standard deviation of a number of extensive and intensive aerosol properties. Data taken during the ten flights during which spirals were flown over El Monte and Riverside, and nine flights with spirals flown over Fullerton, were used in the analysis. For the derived ratio of scattering at 80% RH to scattering at 30% RH, only those data below the altitude at which random error began to dominate are shown.

SCOS indicate a corresponding range of 53 to 69%. At each of these locations, PM2.5 constituted an increasing percentage of PM10 with increasing altitude. The ratio of aerosol scattering at 80% RH to that at 30% RH is derived using the data from Radiance Research nephelometers along with an empirical relationship between scattering intensity and RH (Kasten, 1969). Only those data below the altitude at which random error began to dominate this ratio are shown. The enhanced ratio observed for Riverside suggests that aerosol hygroscopicity is greater in the inland areas, although variations in aerosol size distribution could also account for the change.

## 5.4 Sub-Grid Variability

The primary goal of SCOS was the acquisition of a sufficiently detailed database to lead to effective evaluation of photochemical and aerosol modeling capabilities. Computational limitations, sparse meteorological and air quality measurements, and

limited emissions inventories all serve to limit the minimum useful computational grid size of three-dimensional models. Typical grid cells are 5 km on a side with a vertical dimension that varies with height (Meng et al., 1997). McNair et al. (1996) discuss potential errors involved in assuming that point measurements of a given species represent the grid cell volume-average. In their analysis of data obtained during SCAQS, they found that for the one pair of monitoring sites that were separated by less than 5 km (4.8 km), variations in peak ozone concentration of up to 50% were observed. Similar discrepancies were noted when point measurements were compared with interpolations between surrounding measurements.

Identical patterns were flown on September 4 and 5 as part of an intensive measurement period during SCOS that was designed to investigate nitrate formation along a trajectory beginning east of downtown Los Angeles in Diamond Bar, passing over the ammonia-rich area near Mira Loma, and ending near the eastern edge of the Los Angeles Basin in Riverside. Meteorological measurements describe an initial offshore flow on September 4 that gave way to onshore winds and a 120-150 m deep marine layer on September 5. This transition was largely the result of increasing influence of tropical storm Kevin off the tip of the Baja Peninsula. Peak 1-hour ozone concentrations diminished with this transition from 157 ppb on September 4 to 113 ppb on September 5. To ensure a sufficient amount of aerosol was collected for filter analyses, the Pelican circled ~300 m above each sampling site for approximately one hour. Figure 5.8 shows flight patterns for these missions. Inspection of data from these flights during some of the constant altitude circular flight patterns showed persistent gradients in aerosol concentration. The diameter of the circles ranged from about 5.5 to 6.5 km. This is comparable to the computational grid size of conventional three-dimensional models. Unlike simultaneous ground-based samples at multiple locations, airborne analysis of relative changes in pollutant concentrations is largely insensitive to instrumental variability. On the other hand, with aircraft sampling it is possible that variations perceived as being attributable to horizontal gradients could, in fact, result from sampling along the boundary of a vertical layer that varies in height. Because of flight pattern restrictions, spirals were not flown over any of the

sampling locations, but were flown above adjacent areas. As shown in the insets in Figure 5.8, vertical profiles of PM2.5 and temperature over El Monte and Riverside do not indicate the presence of sharp vertical gradients near the sampling altitude (~500 m), suggesting that any variations are horizontal in nature.

For each sampling location shown in Figure 5.8, an arrow indicates the direction corresponding to the maximum gradient in aerosol concentration. Figures 5.9 and 5.10 show variations along the indicated direction of maximum gradient of several normalized extensive and intensive aerosol properties, as well as size distributions. The data along the gradients were averaged to limit scatter. Some variability was apparent at each location, but that observed at Diamond Bar and Mira Loma on September 4 and Riverside on September 5 is consistent with the presence of strong gradients in aerosol concentration, resulting in $PM2.5_{max}$:$PM2.5_{min}$ ratios of 1.61, 1.33, and 1.39, respectively. The lack of variability in either the intensive properties or the shape of the size distributions suggests that the aerosol concentration varies with location, but its characteristics do not. As is true for most of the Los Angeles Basin, there are major freeways as well as other emissions sources in the vicinity of each of these locations, potentially causing the observed variability. It is also possible that the variability is a result of changes in boundary layer depth over the area of the orbit. It is interesting to note that none of the locations exhibited the same variability, or lack thereof, on both days. Additional measurements are necessary to determine whether the presence of these strong gradients follows a diurnal pattern, which might explain the differences observed over the two-day period since the September 4 mission was conducted approximately four hours earlier than the flight conducted on September 5.

## 5.5 Effect of the Aerosol on Photolysis Rates

Formation of ozone and a number of other gas and aerosol phase species is driven by photochemistry (Seinfeld and Pandis, 1998). Accurate prediction of gas-phase concentrations requires a detailed understanding of the array of reactions responsi-

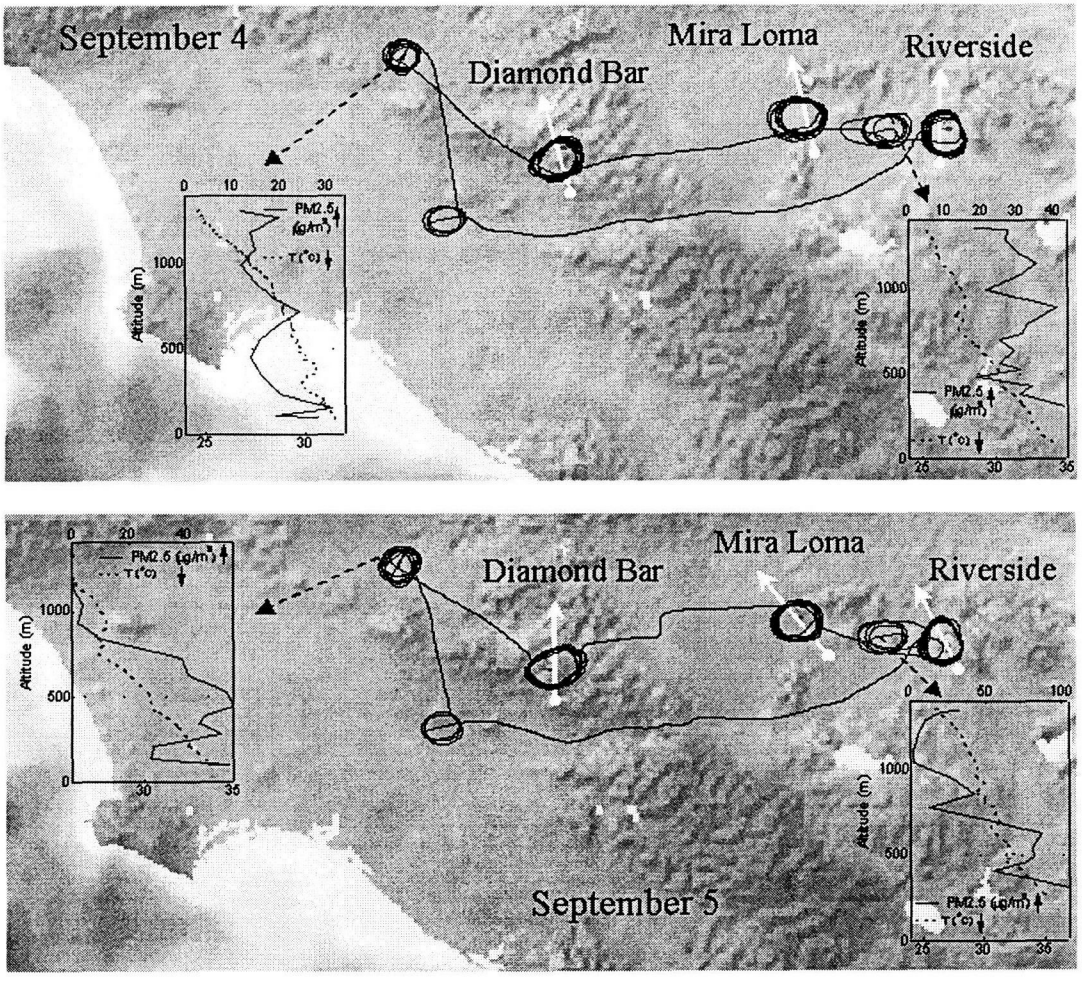


Figure 5.8: Flight patterns for missions conducted on September 4 and 5, along with calculated back trajectories for air parcels arriving at Mira Loma and Riverside during the corresponding sampling intervals. Insets show vertical profiles of PM2.5 and temperature at spiral locations. The heavy horizontal line in each of the profiles represents the approximate altitude of the circles flown above Diamond Bar, Mira Loma, and Riverside. The solid arrows through the flight track represent the direction of maximum aerosol gradient at each of the sampling locations that was used for the analysis presented in Figures 5.9 and 5.10.

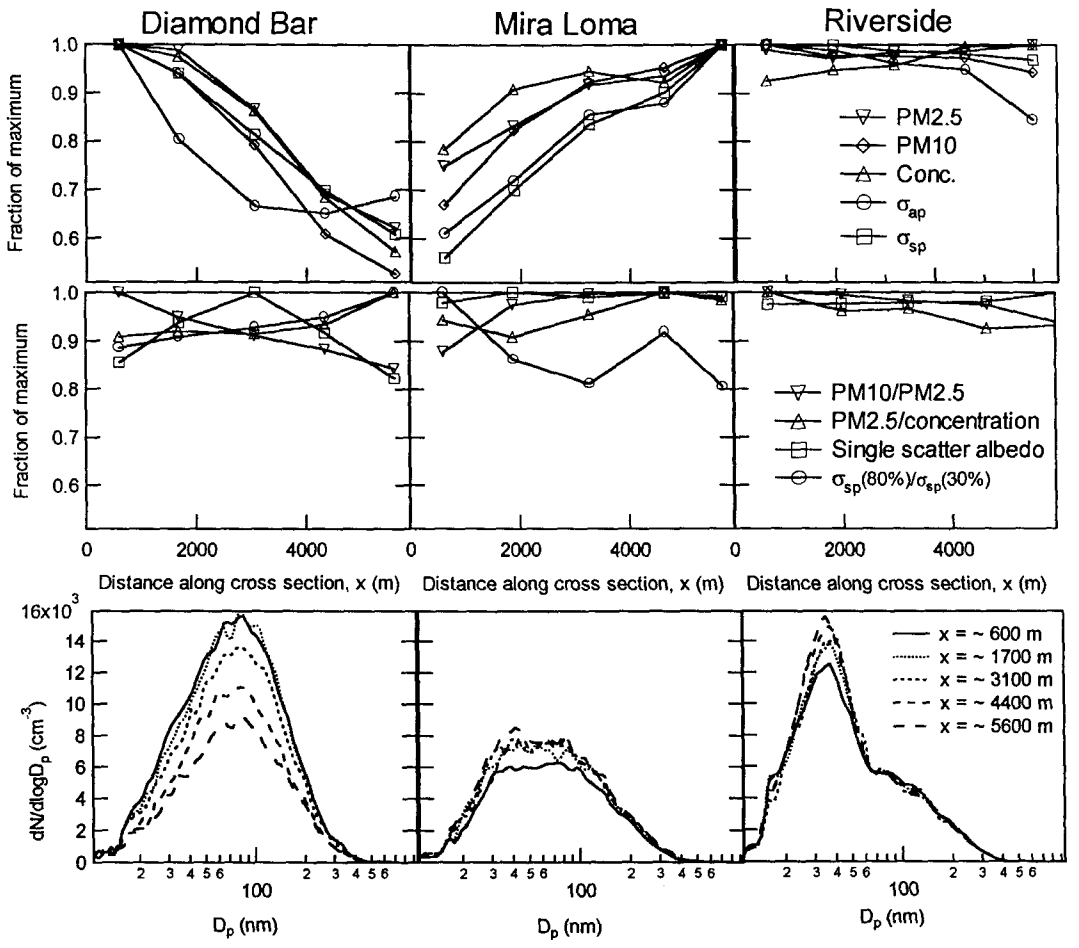


Figure 5.9: Variation of extensive aerosol properties, intensive aerosol properties, and number size distributions as a function of distance along the direction of maximum gradient indicated in Figure 5.8.

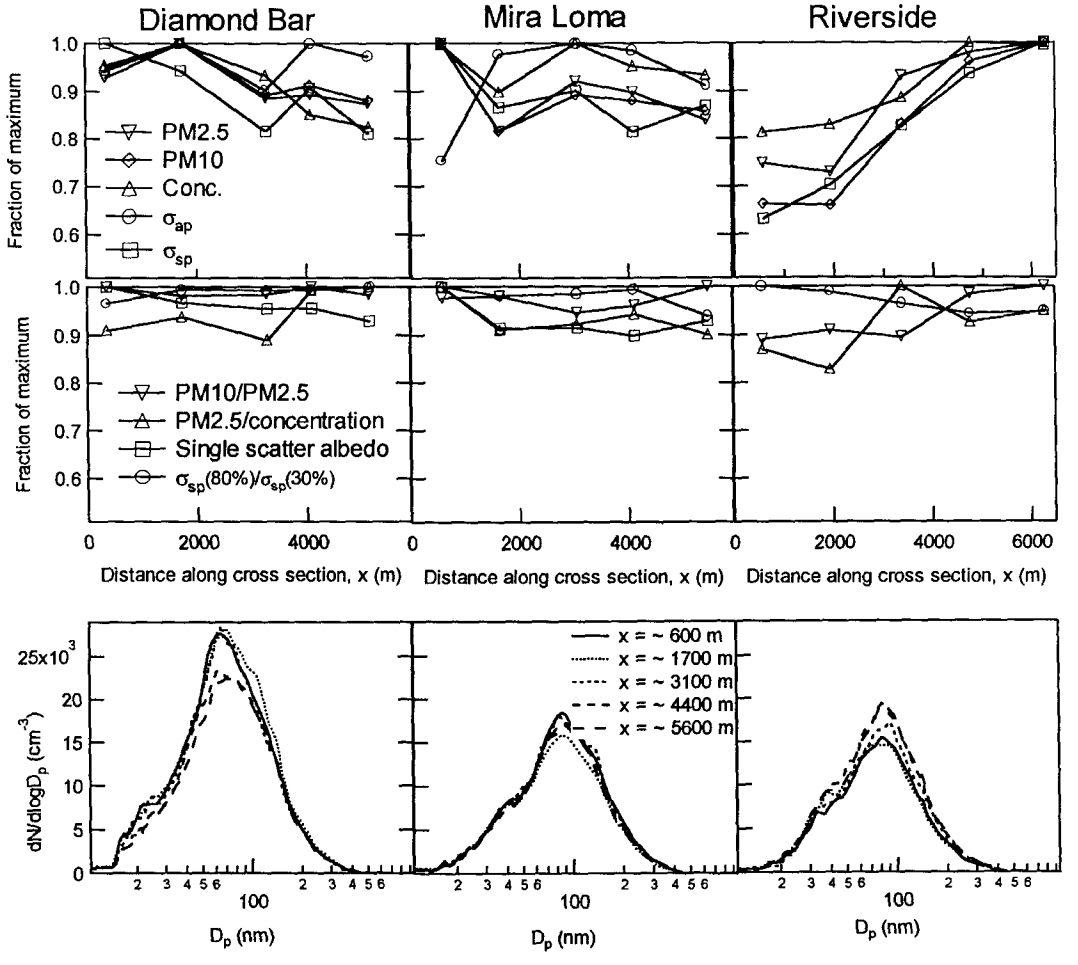


Figure 5.10: The same format as in Figure 5.9 for the aerosol sampled on September 5.

ble for their formation and destruction, as well as the spectrally-resolved actinic flux throughout the area of interest. Direct measurement of actinic flux or key photolysis rates themselves can provide the necessary information, although such data are typically available only at ground-level. Alternatively, vertical aerosol profiles derived from airborne measurements or vertically-resolved models can be used to determine the potential impact of scattering and absorption on photolysis rates. Several investigations of this type have been reported for different regions with varying cloud cover, surface albedo, and solar zenith angle (Demerjian et al., 1980; Ruggaber et al., 1994; Lantz et al., 1996; Castro et al., 1997; Dickerson et al., 1997; Jacobson, 1998, Liao et al., 1999). The extensive aerosol measurements made with the Pelican provide much of the data necessary for such an analysis, thereby reducing uncertainty in the role of the aerosol in atmospheric photochemistry.

The approach taken here to determine photolysis rates has been described in Liao et al. (1999), and will be described only briefly. Actinic flux was calculated using the one-dimensional discrete ordinate radiative transfer (DISTORT) model (Stamnes et al., 1988). The calculations employed eighty vertical layers from 0 to 70 km that ranged in thickness from 100 m in the lowest 3 km, to 5 km between 50 and 70 km in altitude. Aerosol concentration was assumed to be zero above the maximum measurement height. Clearly, this will result in some error in derived photolysis rates. An analysis of the impact of the layers observed at about 2500 m will be discussed below, but no consideration of even higher layers is made, although it is likely that the aerosol present above this height contributes negligibly to the columnar aerosol burden. Actinic flux was calculated for the 290 to 700 nm wavelength range with spectral intervals ranging from 1 nm for wavelengths between 290 and 330 nm, to 5 nm between 600 and 700 nm. Published data for temperature-dependent ozone absorption cross section (Malicet et al., 1995; WMO, 1985), solar irradiance (Neckel and Labs, 1984; Woods et al., 1996), temperature profile (Nagatani and Rosenfield, 1993), ozone profile (McPeters, 1993), and spectrally-resolved surface albedo (Demerjian et al., 1980) were utilized for these analyses. As is common in Southern California during the summer months, clouds were rare during this study and were, therefore, not

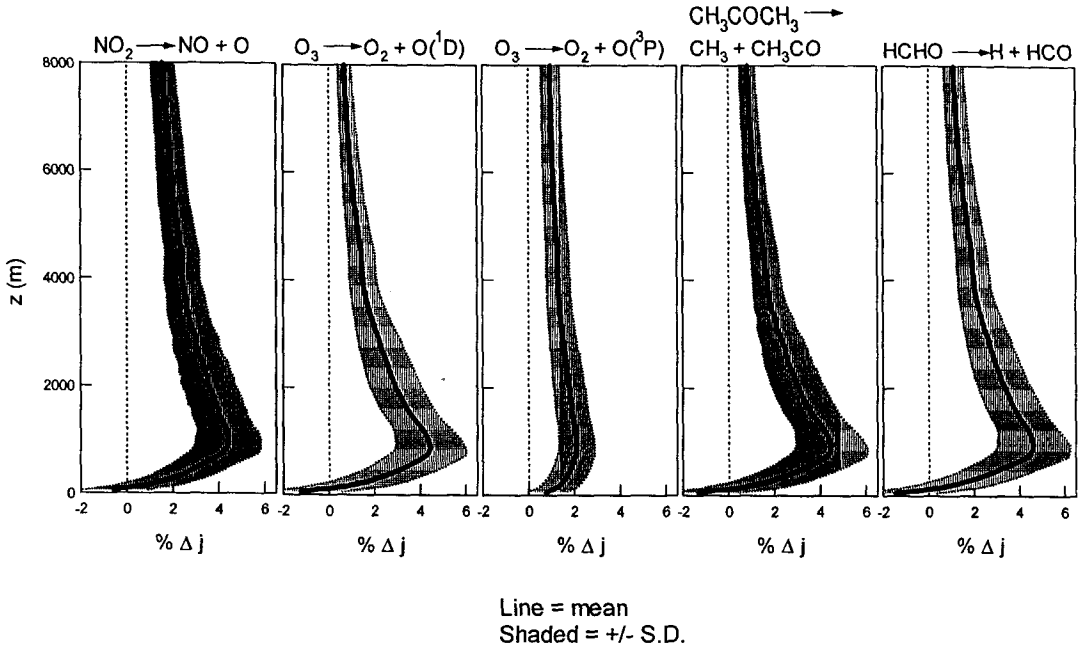


Figure 5.11: Fractional change in five gas-phase photolysis rates calculated to have resulted from the aerosol sampled over El Monte relative to an aerosol-free atmosphere. For each reaction considered, the mean and standard deviation were determined from photolysis rate calculations using measurements made during spirals flown over El Monte on ten flights. Unlike most of the other analyses presented here, altitude is relative to ground level and not sea level.

considered. To clearly demonstrate the variability associated with aerosol concentration and properties, and not time of day, a constant solar zenith angle of 10° was considered.

Consistent with the approach taken to characterize physical and chemical aerosol properties, photolysis rates were computed based on data taken along a cross section during one flight, and taken at one location during several flights. Poor spectral resolution and size-dependent non-idealities prevented direct use of nephelometer and absorption photometer measurements. Instead, aerosol optical properties at each height interval were determined through Mie Theory calculations using the size distributions. As discussed above, the size distribution measurements have vertical resolution of approximately 150 m, which is slightly greater than the minimum vertical layer thickness used in DISORT, so limited interpolation was necessary. The frac-

tional change in several key photolysis rates resulting from the aerosol sampled over El Monte during 10 flights is presented in Figure 5.11. As with the statistical analysis of vertically-resolved aerosol properties shown in Figure 5.7, the mean and standard deviation were calculated and presented as a solid line and shaded region, respectively. Little variation is observed in the impact the aerosol is expected to have on photolysis rates of $NO_2$, HCHO, $CH_3COCH_3$, and $O_3 \rightarrow O(^1D)$, while the impact on photolysis of $O_3$ to form $O(^3P)$ is smaller in magnitude and exhibits less vertical variability than is observed for the other reactions considered. For each reaction analyzed, the El Monte aerosol causes a slight decrease in photolysis rates in the lowest 100 m, with a more pronounced enhancement observed above this height. The presence of a cross-over point at which the fractional change of a given photolysis rate is zero results from an offset between increased diffuse actinic flux due to aerosol-enhanced scattering and decreased direct actinic flux caused by upward scattering and absorption by the overlying aerosol. These cross-overs have been observed in similar analyses with relatively non-absorbing aerosol like that encountered during SCOS (e.g., Liao et al., 1999). The maximum increase in photolysis rates above that expected if no aerosol were present is approximately 2% for $O_3 \rightarrow O(^3P)$, and 5% for each of the other reactions considered. Inclusion of the 2500 m aerosol layers measured during spirals over El Monte on September 9 and 10 results in a further enhancement of approximately 1% (0.3% for $O_3 \rightarrow O(^3P)$). Similar results were obtained when the fractional change in the photolysis rate of $NO_2$ was considered along the east-west cross section described in Figure 5.4 using data from morning and afternoon flights on August 28. As shown in Figure 5.12, only slight variations in photolysis rate alteration are observed along the cross section, both in the morning and afternoon. The sharp gradient in fractional photolysis rate change with height in the lowest 500 m demonstrates the potential error caused by extrapolations of ground-based radiative flux measurements. The impact of aerosols on photolysis rates presented here is similar to estimates of Jacobson (1998) using data obtained over Long Beach on August 27, 1987, during SCAQS, but differs significantly from calculations performed using data obtained over Claremont on the same day. Specifically, Jacobson (1998) predicted that the aerosol present

over Claremont resulted in a decrease of up to about 12% in the $NO_2$ photolysis rate, resulting from a more concentrated and highly absorbing aerosol than was sampled during SCOS. The atypical meteorological conditions during this campaign prevented a comparable severe pollution episode, while improved air quality in Southern California since 1987 would probably limit the likelihood of aerosol loadings similar to those observed in Claremont during SCAQS. Therefore, the results from SCOS and SCAQS probably bound the likely impact that a significant, present-day, pollution episode would have on photolysis rates.

## 5.6 Summary

As part of the Southern California Ozone Study (SCOS), 12 missions were conducted with an aircraft instrumented to characterize the chemical and physical properties of the Los Angeles aerosol. Instrumentation on board included three parallel filter sampling systems, three nephelometers, an absorption photometer, a DMA, and two OPCs. Data from the variety of measurements made were combined to provide a time-resolved physicochemical description of the aerosol. Several closure comparisons were performed between derived and directly measured properties. Best-fit lines through scatter plots containing these data for comparisons of fine aerosol mass, "dry" aerosol scattering coefficient, "wet" aerosol scattering coefficient, hemispherical backscattering coefficient, and absorption coefficient had slopes of 0.91, 1.06, 1.13, 1.21, and 0.55, respectively. The exact cause of the large disagreement in the absorption comparison is not known, although a number of potential errors have been suggested.

The aerosol present over the Los Angeles Basin exhibits a complex three-dimensional structure. Vertically-resolved data suggest that pronounced elevated layers present over the inland areas were formed by injection of aerosol above the ground-level polluted layer along the Southern edge of the San Gabriel Mountains, followed by advection towards the coast through incorporation into the sea breeze return flow. Additional layers were observed about 500 m asl off the coast of Santa Monica, and approximately 2500 m asl over El Monte and Long Beach. Data from spirals flown

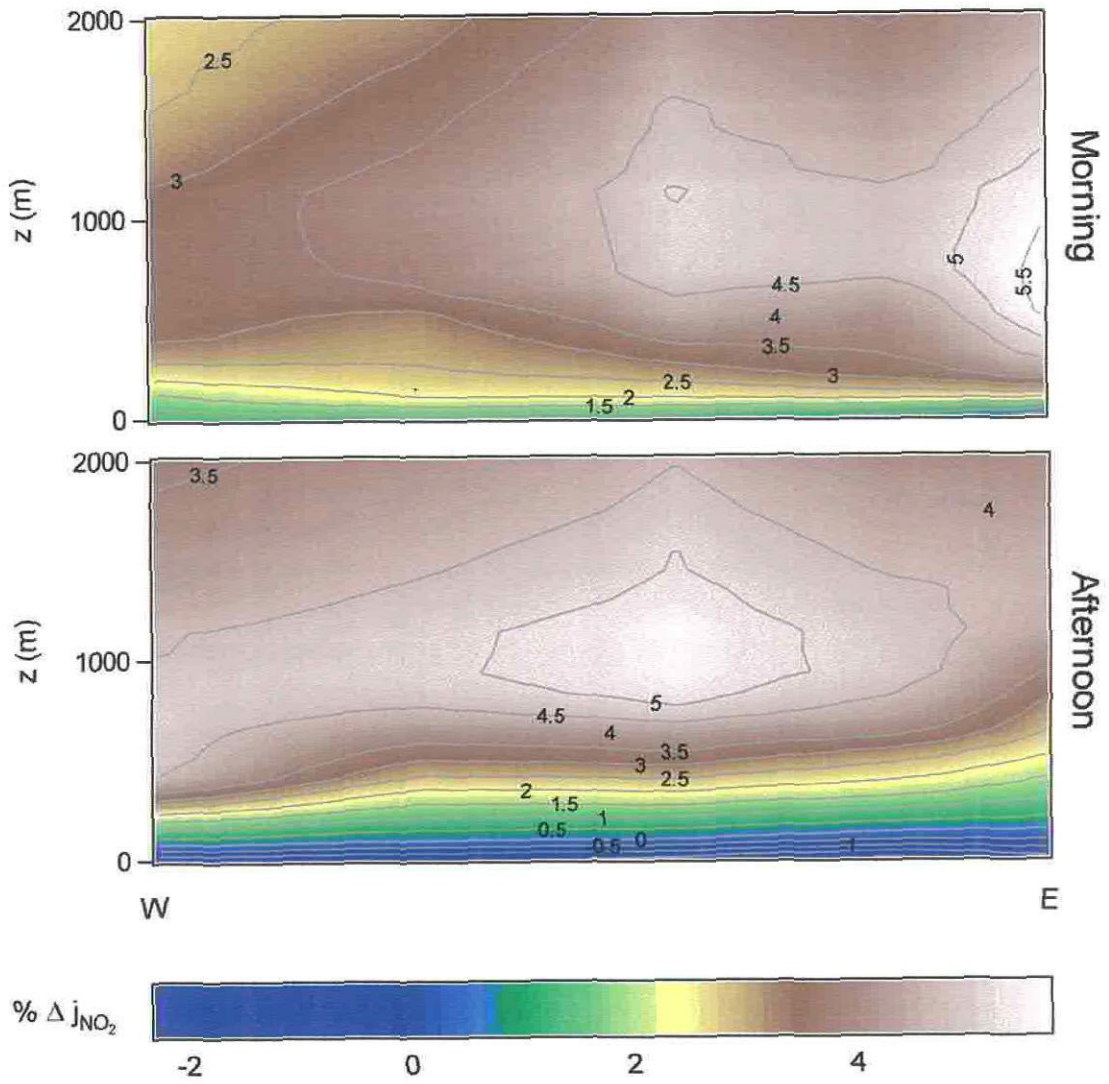


Figure 5.12: Vertically-resolved fractional change in the $NO_2$ photolysis rate calculated using data obtained during spirals flown on the morning and afternoon flights of August 28. The east-west cross section indicated in Figure 5.4 was used for presentation of these data.

over El Monte, Fullerton, and Riverside on several flights over the three-week sampling period were used to provide a limited statistical description of the vertically-resolved aerosol at each location. In general, it was found that variability over time exceeded variability among locations. Constant altitude circles flown over Diamond Bar, Mira Loma, and Riverside yielded evidence of gradients in aerosol concentration sufficient to cause over 50% variability within a 5 x 5 km computational grid cell commonly used in atmospheric models.

Data from spirals flown over El Monte during several flights, as well as from spirals flown over several locations on August 28, were used to analyze the impact of the aerosol on important photolysis rates in the photochemical generation of ozone. On average, the aerosol was predicted to cause a slight decrease in photolysis rates in the first 100 m above ground-level, but led to a more pronounced (up to ~5%) increase above that height. For most of the reactions considered, the 2500 m elevated aerosol layers above El Monte caused an enhancement in photolysis rates of about 1% above that resulting from the aerosol present below these layers. Collectively, the data obtained in this sampling program provide further insight into microphysical processes that govern the size, composition, and spatial and temporal behavior of the Los Angeles aerosol.

# Chapter 6 Conclusions

Analysis of atmospheric aerosols is complicated by their physical, chemical, spatial, and temporal variability. Faced with this complexity, it is necessary to determine the most suitable method of sufficiently characterizing an aerosol in order to investigate the property or effect of interest. Aircraft-based measurements often provide the best approach for studying variable or otherwise complex aerosols, particularly when their columnar properties are of interest. Though many of the limitations related to aircraft measurements are common with those encountered when sampling from other platforms, they are often times more extreme. Beyond the obvious constraints on weight, space, and power, aircraft-based measurements must typically be more time-resolved than their ground-based counterparts, since even a one-minute measurement will be integrated over several kilometers. Size distributions represent an aerosol descriptor that provides temporally (and therefore spatially) resolved information about both intensive and extensive aerosol properties. Although they do not completely define an aerosol population, when combined with additional measurements or assumptions concerning the physical and chemical state of the particles of interest, size distributions do offer enough detail to permit evaluation of a wide range of associated properties.

As with any measurement, it is beneficial to improve the speed with which aircraft-based size distributions can be made, as well as the range they cover. Improvements that have been made in the analysis of DMA data provide a means of accelerating DMA measurements, while, at the same time, improving accuracy. Introduction of scanning flow substantially enhanced the performance of DMAs by expanding their size range, and improving resolution and counting statistics. While these improvements have improved the accuracy of airborne and ground-based measurements, there still exists an enormous potential for improvement.

In many respects, the radiative closure analysis performed using data from ACE-2 was a great success; never before had the measured physicochemical properties of an aerosol been validated through comparison with such a wide range of optical measurements. Discrepancies between derived and measured optical properties were largely within calculated uncertainties. However, it is the uncertainties themselves

that may be regarded as excessive. Possible inaccuracies in assumptions that are used in place of unavailable data provide an all-to-simple explanation for observed discrepancies. Minimization of these possible sources of error will reveal the true accuracy of physicochemical descriptions of sampled aerosols. The discussion of the methodology used for the ACE-2 analysis is comparable in length to the remainder of the chapter. The numerous assumptions and simplifications have been discussed in detail, and future researchers would benefit from examining them in order to find ways to make changes prior to an experiment in order to eliminate the need for them during analysis.

The challenge in processing the SCOS data centered on determining how best to collapse gigabytes of data from a variety of instruments, during several flights that covered hundreds of square kilometers, into a coherent, and hopefully representative, picture of the Los Angeles aerosol. In doing this, necessary evils such as interpolation were required, though undoubtedly inaccurate to some extent given the complex meteorology and topography in Southern California. Likewise, deconvolution of temporal from spatial variations is not possible for the rapidly-evolving Los Angeles aerosol, but again, to provide a concise picture of the aerosol, these difficulties had to be overlooked to some degree. Certain measurements, such as continuous lidar at multiple locations, could have permitted a more accurate description, while additional flights may have aided in the interpretation of some of the complex features observed in the aerosol. Even with these limitations, the data set obtained from the 12 missions conducted during SCOS constitute what is likely the most comprehensive three-dimensional description of the Los Angeles aerosol made to date. In situ analysis of aerosols throughout the basin will provide much of the framework necessary for modeling endeavors in the future.

# Bibliography

[wmo, 1985] (1985). *Atmospheric Ozone.* Technical Report 16, World Meteorological Organization (WMO).

[Ackerman & Toon, 1981] Ackerman, T. P. and Toon, O. B. (1981). Absorption of visible radiation in atmosphere containing mixtures of absorbing and nonabsorbing particles. *Appl. Opt.*, 20, 3661–3667.

[Agarwal & Sem, 1980] Agarwal, J. K. and Sem, G. J. (1980). Continuous flow, single-particle counting condensation nucleus counter. *J. Aerosol Sci.*, 11, 343–357.

[Alofs & Balacumar, 1982] Alofs, D. J. and Balacumar, P. (1982). Inversion to obtain aerosol size distributions from measurements with a differential mobility analyzer. *J. Aerosol Sci.*, 13, 513–527.

[Anderson et al., 1996] Anderson, T. L., Covert, D. S., Marshall, S. F., Laucks, M. L., Charlson, R. J., Waggoner, A. P., Ogren, J. A., Caldow, R., Holm, R. L., Quant, F. R., Sem, G. J., Wiedensohler, A., Ahlquist, N. A., and Bates, T. S. (1996). Performance-characteristics of a high-sensitivity, 3-wavelength, total scatter/backscatter nephelometer. *J. Atmos. Ocean Technol.*, 13, 967–986.

[Bird et al., 1960] Bird, R. B., Stewart, W. E., and Lightfoot, E. N. (1960). *Transport Phenomena.* New York: John Wiley and Sons.

[Biswas et al., 1987] Biswas, P., Jones, C. L., and Flagan, R. C. (1987). Distortion of size distributions by condensation and evaporation in aerosol instruments. *Aerosol Sci. Technol.*, 7, 231–246.

[Blumenthal et al., 1978] Blumenthal, D. L., White, W. H., and Smith, T. B. (1978). Anatomy of a Los Angeles smog episode: Pollutant transport in the daytime sea breeze regime. *Atmospheric Environment*, 12, 893–907.

[Brenguier et al., 2000] Brenguier, J. L., Chuang, P. Y., Fouquart, Y., Johnson, D. W., Parol, F., Pawlowska, H., Pelon, J., Schüller, L., Schröder, F., and Snider, J. (2000). An overview of the ACE-2 CLOUDYCOLUMN closure experiment. *Tellus*, in press.

[Brink et al., 1983] Brink, H. M. T., Plomp, A., Spoelstra, H., and van de Vate, J. F. (1983). A high resolution electrical mobility aerosol spectrometer (MAS). *J. Aerosol Sci.*, 14, 589–597.

[Cachier et al., 1986] Cachier, H., Buat-Ménard, P., Fontugne, M., and Chesselet, R. (1986). Long-range transport of continentally-derived particulate carbon in the marine atmosphere: Evidence from stable carbon isotope studies. *Tellus*, 38B, 161–177.

[Castro et al., 1997] Castro, T., RuizSuarez, L. G., RuizSuarez, J. C., Molina, M. J., and Montero, M. (1997). Sensitivity analysis of a UV radiation transfer model and experimental photolysis rates of NO2 in the atmosphere of Mexico City. *Atmospheric Environment*, 31, 609–620.

[Chow et al., 1994] Chow, J. C., Watson, J. G., Fujita, E. M., Lu, Z. Q., Lawson, D. R., and Ashbaugh, L. L. (1994). Temporal and spatial variations of PM2.5 and PM10 aerosol in the Southern California Air Quality Study. *Atmospheric Environment*, 28, 2061–2080.

[Chow et al., 1993] Chow, J. C., Watson, J. G., Pritchett, L. C., Pierson, W. R., Frazier, C. A., and Purcell, R. G. (1993). The dri thermal optical reflectance carbon analysis system - description, evaluation and applications in United States air-quality studies. *Atmospheric Environment*, 27, 1185–1201.

[Clarke et al., 1996] Clarke, A. D., Porter, J. N., Valero, F. P. J., and Pilewskie, P. (1996). Vertical profiles, aerosol microphysics, and optical closure during the Atlantic Stratocumulus Transition Experiment - measured and modeled column optical-properties. *J. Geophys. Res.*, 101, 4443–4453.

[Cooper & Spielman, 1976] Cooper, D. W. and Spielman, L. A. (1976). Data inversion using nonlinear programming with physical constraints: Aerosol size distribution measurement by impactors. *Atmos. Env.*, 10, 723–729.

[Crump & Seinfeld, 1982] Crump, J. G. and Seinfeld, J. H. (1982). A new algorithm for inversion of aerosol size distribution data. *Aerosol Sci. Technol.*, 1, 15–34.

[de Juan & de la Mora, 1998] de Juan, L. and de la Mora, J. F. (1998). High resolution size analysis of nanoparticles and ions: Running a vienna dma of near optimal length at reynolds numbers up to 5000. *J. Aerosol Sci.*, 29, 617–626.

[Demerjian et al., 1980] Demerjian, K. L., Schere, K. L., and Peterson, J. T. (1980). Theoretical estimates of actinic (spherically integrated) flux and photolytic rate constants of atmospheric species in the lower troposphere. *Adv. Environ. Sci. Technol.*, 10, 369–459.

[Dickerson et al., 1997] Dickerson, R. R., Kondragunta, S., Stenchikov, G., Civerolo, K. L., Doddridge, B. G., and Holben, B. N. (1997). The impact of aerosols on solar ultraviolet radiation and photochemical smog. *Science*, 278, 827–830.

[Fissan et al., 1983] Fissan, H. J., Helsper, C., and Thielen, H. J. (1983). Determination of particle size distributions by means of an electrostatic classifier. *J. Aerosol Sci.*, 14, S354–357.

[Fissan et al., 1996] Fissan, H. J., Hummes, D., Stratmann, F., Buscher, P., Neumann, S., Pui, D. Y. H., and Chen, D. (1996). Experimental comparison of four differential mobility analyzers for nanometer aerosol measurements. *Aerosol Sci. Technol.*, 24, 1–13.

[Flagan, 1999] Flagan, R. C. (1999). On differential mobility analyzer resolution. *Aerosol Sci. Technol.*, 30, 556–570.

[Flagan et al., 1991] Flagan, R. C., Wang, S. C., Yin, F. D., Seinfeld, J. H., Reischl, G., Winklmayr, W., and Karch, R. (1991). Electrical mobility measurements of fine-particle formation during chamber studies of atmospheric photochemical-reactions. *Environ. Sci. Technol.*, 25, 883–890.

[Friedlander, 1977] Friedlander, S. K. (1977). *Smoke, Dust and Haze.* New York: Wiley-Interscience.

[Fuchs, 1963] Fuchs, N. A. (1963). On the stationary charge distribution on aerosol particles in a bipolar ionic atmosphere. *Geofis. Pura Appl.*, 56, 185–193.

[Fuller et al., 1999] Fuller, K. A., Malm, W. C., and Kreidenweis, S. M. (1999). Effects of mixing on extinction by carbonaceous particles. *J. Geophys. Res.*, 104, 15941–15954.

[Gassó et al., 2000] Gassó, S., Hegg, D. A., Covert, D. S., Collins, D. R., Noone, K. J., Oström, E., Schmid, B., Russell, P. B., Livingston, J. M., Durkee, P. A., and Jonsson, H. (2000). Influence of humidity on the aerosol scattering coefficient and its effect on the upwelling radiance during ACE-2. *Tellus*, in press.

[Gosman & Pun, 1974] Gosman, A. D. and Pun, W. M. (1974). *Lecture Notes for 'Calculation of recirculating flows'.* London: Imperial Colleg.

[Hagen & Alofs, 1983] Hagen, D. E. and Alofs, D. J. (1983). Linear inversion method to obtain aerosol size distributions from measurements with a differential mobility analyzer. *Aerosol Sci. Technol.*, 2, 465–475.

[Hansson, 1997] Hansson, H. C. (1997). *Personal Communication.*

[Harley et al., 1993] Harley, R. A., Russell, A. G., McRae, G. J., Cass, G. R., and Seinfeld, J. H. (1993). Photochemical modeling of the Southern California Air Quality Study. *Environ. Sci. Technol.*, 27, 378–388.

[Hegg et al., 1997] Hegg, D. A., Livingston, J., Hobbs, P. V., Novakov, T., and Russell, P. (1997). Chemical apportionment of aerosol column optical depth off the mid-Atlantic coast of the United-States. *J. Geophys. Res.*, 102, 25293–25303.

[Hoff et al., 1996] Hoff, R. M., Guisebagley, L., Staebler, R. M., Wiebe, H. A., Brook, J., Georgi, B., and Dusterdiek, T. (1996). Lidar, nephelometer, and in-situ aerosol experiments in Southern Ontario. *J. Geophys. Res.*, 101, 19199–19209.

[Hoff et al., 1997] Hoff, R. M., Harwood, M., Sheppard, A., Froude, F., Martin, J. B., and Strapp, W. (1997). Use of airborne lidar to determine aerosol sources and movement in the Lower Fraser Valley (LFV), BC. *Atmospheric Environment*, 31, 2123–2134.

[Hoppel et al., 1986] Hoppel, W. A., Frick, G. M., and Larson, R. E. (1986). Effect of non-precipitating clouds on the aerosol size distribution in the marine boundary-layer. *Geophys. Res. Lett.*, 13, 125–128.

[Howell & Huebert, 1998] Howell, S. G. and Huebert, B. J. (1998). Determining marine aerosol scattering characteristics at ambient humidity from size-resolved chemical-composition. *J. Geophys. Res.*, 103, 1391–1404.

[Jacobson, 1997] Jacobson, M. Z. (1997). Development and application of a new air pollution modeling system .3. Aerosol-phase simulations. *Atmospheric Environment*, 31, 587–608.

[Jacobson, 1998] Jacobson, M. Z. (1998). Studying the effects of aerosols on vertical photolysis rate coefficient and temperature profiles over an urban airshed. *J. Geophys. Res.*, 103, 10593–10604.

[Jensen et al., 1996] Jensen, T. L., Kreidenweis, S. M., Kim, Y., Sievering, H., and Pszenny, A. (1996). Aerosol distributions in the North-Atlantic marine boundary-layer during Atlantic Stratocumulus Transition Experiment Marine Aerosol and Gas-Exchange. *J. Geophys. Res.*, 101, 4455–4467.

[Johnson et al., 2000] Johnson, D. W., Osborne, S., Wood, R., Suhre, K., Johnson, R., Businger, S., Quinn, P. K., Wiedensohler, A., Durkee, P. A., Russell, L. M., Andreae, M. O., O'Dowd, C., Noone, K. J., Bandy, B., Rudolph, J., and Rapsomanikis, S. (2000). An overview of the Lagrangian experiments undertaken during the North Atlantic regional Aerosol Characterization Experiment (ACE-2). *Tellus*, in press.

[Kasten, 1969] Kasten, F. (1969). Visibility in the phase of pre-condensation. *Tellus*, 21, 631–635.

[Knutson & Whitby, 1975] Knutson, E. O. and Whitby, K. T. (1975). Aerosol classification by electric mobility: Apparatus, theory, and applications. *J. Aerosol Sci.*, 6, 443–451.

[Kousaka et al., 1985] Kousaka, Y., Okuyama, K., and Adachi, M. (1985). Determination of particle-size distribution of ultra-fine aerosols using a differential mobility analyzer. *Aerosol Sci. Technol.*, 4, 209–225.

[Kousaka et al., 1986] Kousaka, Y., Okuyama, K., Adachi, M., and Mimura, T. (1986). Effect of brownian diffusion on electrical classification of ultrafine aerosol-particles in differential mobility analyzer. *J. Chem. Eng. Japan*, 19, 401–407.

[Lalas et al., 1983] Lalas, D. P., Asimakopoulos, D. N., Deligiorgi, D. G., and Helmis, C. G. (1983). Sea-breeze circulation and photochemical pollution in Athens, Greece. *Atmospheric Environment*, 17, 1621–1632.

[Lantz et al., 1996] Lantz, K. O., Shetter, R. E., Cantrell, C. A., Flocke, S. J., Calvert, J. G., and Madronich, S. (1996). Theoretical, actinometric, and radiometric determinations of the photolysis rate coefficient of NO2 during the Mauna Loa observatory photochemistry experiment 2. *J. Geophys. Res.*, 101, 14613–14629.

[Larson et al., 1988] Larson, S. M., Cass, G. R., Hussey, K. J., and Luce, F. (1988). Verification of image-processing based visibility models. *Environ. Sci. Technol.*, 22, 629–637.

[Lawson & Hanson, 1974] Lawson, C. L. and Hanson, R. J. (1974). *Solving Least Squares Problems.* Englewood Cliffs, NJ: Prentice-Hall.

[Li et al., 1997] Li, S. M., Macdonald, A. M., Strapp, J. W., Lee, Y. N., and Zhou, X. L. (1997). Chemical and physical characterizations of atmospheric aerosols over Southern California. *J. Geophys. Res.*, 102, 21341–21353.

[Liao et al., 1999] Liao, H., Yung, Y. L., and Seinfeld, J. H. (1999). Effects of aerosols on tropospheric photolysis rates in clear and cloudy atmospheres. *J. Geophys. Res.*, 104, 23697–23707.

[Lloyd et al., 1997] Lloyd, J. J., Taylor, C. J., Lawson, R. S., and Shields, R. A. (1997). The use of the L-curve method in the inversion of diffusion battery data. *J. Aerosol Sci.*, 28, 1251–1264.

[Lu & Turco, 1994] Lu, R. and Turco, R. P. (1994). Air pollutant transport in a coastal environment .1. 2-dimensional simulations of sea-breeze and mountain effects. *J. atmos. Sci.*, 51, 2285–2308.

[Lu & Turco, 1995] Lu, R. and Turco, R. P. (1995). Air pollutant transport in a coastal environment .2. 3-dimensional simulations over Los Angeles basin. *Atmospheric Environment*, 29(13), 1499–1518.

[Lu et al., 1997] Lu, R., Turco, R. P., and Jacobson, M. Z. (1997). An integrated air pollution modeling system for urban and regional scales .1. Structure and performance. *J. Geophys. Res.*, 102, 6063–6079.

[Lurmann et al., 1997] Lurmann, F. W., Wexler, A. S., Pandis, S. N., Musarra, S., Kumar, N., and Seinfeld, J. H. (1997). Modelling urban and regional aerosols .2. Application to California's South Coast Air Basin. *Atmospheric Environment*, 31, 2695–2715.

[Maher & Laird, 1985] Maher, E. F. and Laird, N. M. (1985). Em algorithm reconstruction of particle-size distributions from diffusion battery data. *J. Aerosol Sci.*, 16, 557–570.

[Malicet et al., 1995] Malicet, J., Daumont, D., Charbonnier, J., Parisse, C., Chakir, A., and Brion, J. (1995). Ozone uv spectroscopy .2. Absorption cross-sections and temperature-dependence. *J. Atmos. Chem.*, 21, 263–273.

[Markowski, 1987] Markowski, G. R. (1987). Improving twomey algorithm for inversion of aerosol measurement data. *Aerosol Sci. Technol.*, 7, 127–141.

[McNair et al., 1996] McNair, L. A., Harley, R. A., and Russell, A. G. (1996). Spatial inhomogeneity in pollutant concentrations, and their implications for air quality model evaluation. *Atmospheric Environment*, 30, 4291–4301.

[McPeters, 1993] McPeters, R. (1993). Ozone profile comparisons. In E. E. Remsberg & M. J. Prather (Eds.), *The Atmospheric Effects of Stratospheric Aircraft: Report of the 1992 Models and Measurements Workshop* (pp. A1–A47). NASA Ref. Publ. 1292.

[Meek & Craggs, 1978] Meek, J. M. and Craggs, J. D., Eds. (1978). *Electrical Breakdown of Gases.* New York: John Wiley and Sons.

[Meng et al., 1997] Meng, Z., Dabdub, D., and Seinfeld, J. H. (1997). Chemical coupling between atmospheric ozone and particulate matter. *Science*, 277, 116–119.

[Meng et al., 1998] Meng, Z. Y., Dabdub, D., and Seinfeld, J. H. (1998). Size-resolved and chemically resolved model of atmospheric aerosol dynamics. *J. Geophys. Res.*, 103, 3419–3435.

[Mertes et al., 1995] Mertes, S., Schroder, F., and Wiedensohler, A. (1995). The particle-detection efficiency curve of the TSI-3010 CPC as a function of the temperature difference between saturator and condenser. *Aerosol Sci. Technol.*, 23, 257–261.

[Mishchenko et al., 1997] Mishchenko, M. I., Travis, L. D., Kahn, R. A., and West, R. A. (1997). Modeling phase functions for dustlike tropospheric aerosols using a

shape mixture of randomly oriented polydisperse spheroids. *J. Geophys. Res.*, 102, 16831–16847.

[Moelwyn-Hughes, 1961] Moelwyn-Hughes, E. A. (1961). *Physical Chemistry.* Tarrytown, New York: Pergamon.

[Nagatani & Rosenfield, 1993] Nagatani, R. M. and Rosenfield, J. E. (1993). Temperature, heating, and circulation. In E. E. Remsberg & M. J. Prather (Eds.), *The Atmospheric Effects of Stratospheric Aircraft: Report of the 1992 Models and Measurements Workshop* (pp. A1–A47). NASA Ref. Publ. 1292.

[Neckel & Labs, 1984] Neckel, H. and Labs, D. (1984). The solar-radiation between 3300A and 12500A. *Sol. Phys.*, 90, 205–258.

[Öström & Noone, 2000] Öström, E. and Noone, K. J. (2000). Vertical profiles of aerosol scattering and absorption measured in situ during the North Atlantic Aerosol Characterization Experiment. *Tellus*, in press.

[Pandis et al., 1992] Pandis, S. N., Harley, R. A., Cass, G. R., and Seinfeld, J. H. (1992). Secondary organic aerosol formation and transport. *Atmospheric Environment*, 26, 2269–2282.

[Patankar, 1980] Patankar, S. V. (1980). *Numerical Heat Transfer and Fluid Flow.* New York: McGraw-Hill.

[Patterson et al., 1977] Patterson, E. M., Gillette, D. A., and Stockton, B. H. (1977). Complex index of refraction between 300 and 700 nm for Saharan aerosols. *J. Geophys. Res.*, 82, 3153–3160.

[Pruppacher & Klett, 1997] Pruppacher, H. R. and Klett, J. D. (1997). *Microphysics of Clouds and Precipitation.* Reidel.

[Putaud et al., 2000] Putaud, J. P., VanDingenen, R., Mangoni, M., Virkkula, A., Raes, F., Maring, H., Prospero, J. M., Swietlicki, E., Berg, O. H., Hillamo, R., and Makela, T. (2000). Chemical mass closure and origin assessment of the submicron

aerosol in the marine boundary layer and the free troposphere at tenerife during ACE-2. *Tellus*, in press.

[Quant et al., 1992] Quant, F. R., Caldow, R., Sem, G. J., and Addison, T. J. (1992). Performance of condensation particle counters with three continuous-flow designs. *J. Aerosol Sci.*, 23, S1251–S1264.

[Raes et al., 2000] Raes, F., Bates, T., McGovern, F. M., and Liedekerke, M. V. (2000). The second Aerosol Characterization Experiment (ACE-2): General overview and main results. *Tellus*, in press.

[Raes et al., 1997] Raes, F., Vandingenen, R., Cuevas, E., Vanvelthoven, P. F. J., and Prospero, J. M. (1997). Observations of aerosols in the free troposphere and marine boundary-layer of the subtropical Northeast Atlantic - discussion of processes determining their size distribution. *J. Geophys. Res.*, 102, 21315–21328.

[Redemann et al., 1998] Redemann, J., Turco, R. P., Pueschel, R. F., Fenn, M. A., Browell, E. V., and Grant, W. B. (1998). A multi-instrument approach for characterizing the vertical structure of aerosol properties - case-studies in the Pacific basin troposphere. *J. Geophys. Res.*, 103, 23287–23298.

[Reineking & Porstendorfer, 1986] Reineking, A. and Porstendorfer, J. (1986). Measurements of particle loss functions in a differential mobility analyzer. *Aerosol Sci. Technol.*, 5, 483–486.

[Reischl et al., 1996] Reischl, G. P., Makela, J. M., Karch, R., and Necid, J. (1996). Bipolar charging of ultrafine particles in the size range below 10 nm. *J. Aerosol Sci.*, 27, 931–949.

[Rossell-Llompart et al., 1996] Rossell-Llompart, J., Loscertales, I. G., Bingham, D., and de la Mora, J. F. (1996). Sizing nanoparticles and ions with a short differential mobility analyzer. *J. Aerosol Sci.*, 27, 695–719.

[Ruggaber et al., 1994] Ruggaber, A., Dlugi, R., and Nakajima, T. (1994). Modeling radiation quantities and photolysis frequencies in the troposphere. *J. Atmos. Chem.*, 18, 171–210.

[Russell et al., 1995] Russell, L. M., Flagan, R. C., and Seinfeld, J. H. (1995). Asymmetric instrument response resulting from mixing effects in accelerated DMA-CPC measurements. *Aerosol Sci. Technol.*, 23, 491–509.

[Russell et al., 996a] Russell, L. M., Huebert, B. J., Flagan, R. C., and Seinfeld, J. H. (1996a). Characterization of submicron aerosol-size distributions from time-resolved measurements in the Atlantic Stratocumulus Transition Experiment Marine Aerosol and Gas-Exchange. *J. Geophys. Res.*, 101, 4469–4478.

[Russell et al., 996b] Russell, L. M., Zhang, S. H., Flagan, R. C., Seinfeld, J. H., Stolzenburg, M. R., and Caldow, R. (1996b). Radially classified aerosol detector for aircraft-based submicron aerosol measurements. *J. Atmos. Ocean Technol.*, 13, 598–609.

[Russell & Heintzenberg, 2000] Russell, P. B. and Heintzenberg, J. (2000). An overview of the ACE-2 clear sky column closure experiment (CLEARCOLUMN). *Tellus*, in press.

[Saxena et al., 1995] Saxena, P., Hildemann, L. M., Mcmurry, P. H., and Seinfeld, J. H. (1995). Organics alter hygroscopic behavior of atmospheric particles. *J. Geophys. Res.*, 100, 18755–18770.

[Schmeling et al., 2000] Schmeling, M., Russell, L. M., Erlick, C., Collins, D. R., Jonsson, H. H., Wang, Q., Kregsamer, P., and Streli, C. (2000). Chemical composition and characterization of aerosol particles from Pelican flights in clean, polluted and dust containing air masses during ACE2. *Tellus*, in press.

[Schmid et al., 2000] Schmid, B., Livingston, J. M., Russell, P. B., Durkee, P. A., Jonsson, H. H., Collins, D. R., Flagan, R. C., Seinfeld, J. H., Gassó, S., Hegg, D. A., Oström, E., Noone, K. J., Welton, E. J., Voss, K., Gordon, H. R., Formenti,

P., and Andreae, M. O. (2000). Clear sky closure studies of lower tropospheric aerosol and water vapor during ACE-2 using airborne sunphotometer, airborne in-situ, space-borne, and ground-based measurements. *Tellus*, in press.

[Seinfeld & Pandis, 1998] Seinfeld, J. H. and Pandis, S. N. (1998). *Atmospheric Chemistry and Physics.* New York: Wiley-Interscience.

[Stamnes et al., 1988] Stamnes, K., Tsay, S. C., Wiscombe, W., and Jayaweera, K. (1988). Numerically stable algorithm for discrete-ordinate- method radiative-transfer in multiple-scattering and emitting layered media. *Appl. Opt.*, 27, 2502–2509.

[Stolzenburg, 1988] Stolzenburg, M. R. (1988). *An Ultrafine Aerosol Size Distribution Measuring System.* PhD thesis, University of Minnesota.

[Swietlicki et al., 2000] Swietlicki, E., Zhou, J., Covert, D. S., Hameri, K., Busch, B., Vakeva, M., Dusek, U., Berg, O. H., Wiedensohler, A., Aalto, P., Makela, J., Marinsson, B. G., Papaspiropoulos, G., Mentes, B., Frank, G., and Stratmann, F. (2000). Hygroscopic properties of aerosol particles in the north-eastern Atlantic during ACE-2. *Tellus*, in press.

[Tang, 1996] Tang, I. N. (1996). Chemical and size effects of hygroscopic aerosols on light-scattering coefficients. *J. Geophys. Res.*, 101, 19245–19250.

[Tang & Munkelwitz, 1994] Tang, I. N. and Munkelwitz, H. R. (1994). Water activities, densities, and refractive-indexes of aqueous sulfates and sodium-nitrate droplets of atmospheric importance. *J. Geophys. Res.*, 99, 18801–18808.

[Tang et al., 1997] Tang, I. N., Tridico, A. C., and Fung, K. H. (1997). Thermodynamic and optical-properties of sea-salt aerosols. *J. Geophys. Res.*, 102, 23269–23275.

[Tegen & Fung, 1994] Tegen, I. and Fung, I. (1994). Modeling of mineral dust in the atmosphere - sources, transport, and optical-thickness. *J. Geophys. Res.*, 99, 22897–22914.

[Twomey, 1975] Twomey, S. (1975). Comparison of constrained linear inversion and an iterative nonlinear algorithm applied to the indirect estimation of particle size distributions. *J. Comput. Phys.*, 18, 188–200.

[Wakamatsu et al., 1983] Wakamatsu, S., Ogawa, Y., Murano, K., Goi, K., and Aburamoto, Y. (1983). Aircraft survey of the secondary photochemical pollutants covering the Tokyo metropolitan area. *Atmospheric Environment*, 17, 827–835.

[Wakimoto & McElroy, 1986] Wakimoto, R. M. and McElroy, J. L. (1986). Lidar observation of elevated pollution layers over Los Angeles. *J. Clim. appl. Met.*, 25, 1583–1599.

[Wang & Flagan, 1989] Wang, S. C. and Flagan, R. C. (1989). Scanning electrical mobility spectrometer. *J. Aerosol Sci.*, 20, 1485–1488.

[Wang et al., 1992] Wang, S. C., Paulson, S. E., Grosjean, D., Flagan, R. C., and Seinfeld, J. H. (1992). Aerosol formation and growth in atmospheric organic nox systems .1. outdoor smog chamber studies of c-7-hydrocarbons and c-8-hydrocarbons. *Atmos. Env.*, 26, 403–420.

[White, 1990] White, W. H. (1990). Contribution to light extinction, in *Acid Deposition, State of Science and Technology, NAPAP Rep. 24*. Natl. Acid Precip. Assess. Program, Washington, D.C., 85–102.

[Wiedensohler, 1988] Wiedensohler, A. (1988). An approximation of the bipolar charge-distribution for particles in the sub-micron size range. *J. Aerosol Sci.*, 19, 387–389.

[Wolfenbarger & Seinfeld, 1990] Wolfenbarger, J. K. and Seinfeld, J. H. (1990). Inversion of aerosol size distribution data. *J. Aerosol Sci.*, 21, 227–247.

[Woods, 1996] Woods, T. N. (1996). Validation of the UARS solar unltraviolet irradiances: Comparison with the ATLAS 1 and 2 measurements. *J. Geophys. Res.*, 101, 9541–9569.

[Zhang et al., 1995] Zhang, S. H., Akutsu, Y., Russell, L. M., Flagan, R. C., and Seinfeld, J. H. (1995). Radial differential mobility analyzer. *Aerosol Sci. Technol.*, 23, 357–372.

[Zhang & Flagan, 1996] Zhang, S. H. and Flagan, R. C. (1996). Resolution of the radial differential mobility analyzer for ultrafine particles. *J. Aerosol Sci.*, 27, 1179–1200.

[Zhang et al., 1993] Zhang, X. Q., McMurry, P. H., Hering, S. V., and Casuccio, G. S. (1993). Mixing characteristics and water-content of submicron aerosols measured in Los Angeles and at the Grand Canyon. *Atmospheric Environment*, 27, 1593–1607.